Physics – Uspekhi **60** (5) 435 – 471 (2017)

REVIEWS OF TOPICAL PROBLEMS PACS numbers: **61.80. – x**, **61.82. – d**, **61.85. + p**

Nano- and microstructuring of solids by swift heavy ions

F F Komarov

DOI: https://doi.org/10.3367/UFNe.2016.10.038012

Contents

Abstract. We review the current stage of research of track formation processes and mechanisms in materials irradiated by swift ions. We show that the nature and morphology of tracks depend on the type and structure of the material and on the energy density transfer to its electron subsystem. Swift heavy ions serve as tools to synthesize nanoclusters and nanowires, to controllably change their morphology, and to tailor electronic, magnetic, and optical properties. The unique optical, photoelectric, and conducting properties of tracks can be used to create a new generation of electronic and optoelectronic nanosize devices. These low-dimensional objects exhibit quantum behavior and are stimulating a broad range of fundamental and applied research.

Keywords: swift heavy ions, ion irradiation, track, chemical etching, ion-track template, nanotechnology

1. Introduction

For fast ions with kinetic energies $E \geqslant 1$ MeV a.m.u.$^{-1}$, the rate with which energy is imparted to the electron subsystem, $(\mathrm{d}E/\mathrm{d}x)_\mathrm{e}$, is $10^3 - 10^4$ times higher than the rate of energy imparted to the nuclear subsystem of the solid. As was demonstrated in Ref. [1], the high rate of energy transfer to the electron subsystem enhances the role of electron excitations in generating structural defects, causes intense inelastic sputtering of materials, and initiates a number of specific effects, such as track formation, local melting, amorphization, creation of extraordinary phases (high-pressure phases, fullerenes, and nanotubes), generation of shock waves, and the destruction of materials. The most important and interesting result concerning the penetration of high-energy ions through solids is the formation of specific spatially distributed defects, or tracks, at least a few microns in depth and a few nanometers wide. Such defects are commonly known as latent tracks if they can be identified by chemical etching of the irradiated material.

The discovery of ion tracks dates back to 1959 when Silk and Barnes published transmission electron micrographs of mica with long straight damage trails created by single fragments from the fission of ^{235}U [2]. Soon after that, it was realized that ion tracks are narrow (< 5 nm), stable, chemically reactive regions resulting from the interaction between projectile ions and target electrons [3]. Later, it was found that tracks are formed in insulators and some semiconductors if the electron stopping power S_e exceeded a material-dependent threshold value $S_{\mathrm{e,\,thr}}$. The damage region created around the swift heavy ion (SHI) trajectory in dielectric materials often exhibits a higher chemical reactivity than the unmodified surroundings. Therefore, nanochannels can be created in track regions by means of treatment in an appropriate etching agent. Track etching has been extensively used in particle detectors [3] and in the processing of membranes with a narrow distribution of pore size, specially using polymeric materials [4].

The production of micro- and nanostructures with interesting practical properties, which then become an integral part of devices for specific applications, requires appropriate techniques or methods. One of them, the

F F Komarov Sevchenko Research Institute of Applied Physics Problems, Belarussian State University,
ul. Kurchatova 7, 220045 Minsk, Belarus
Tel. + 375 (17) 212 48 33
E-mail: KomarovF@bsu.by

Received 26 September 2015, revised 19 May 2016
Uspekhi Fizicheskikh Nauk **187** (5) 465 – 504 (2017)
DOI: https://doi.org/10.3367/UFNr.2016.10.038012
Translated by F F Komarov; edited by A M Semikhatov

template-based method [5], which consists in filling a host porous medium with one or more desired materials (for example, by electrochemical processing), is now commonly used for the synthesis of metallic or polymeric micro- or nanostructures in wires or tubules [6]. Such track-etch templates allows synthesizing wires or tubules with a well-controlled size and shape and exhibiting a small roughness and a large aspect ratio; sizes from 10 nm to several μm with the length-to-diameter ratio in the range 10–1000 can be selected. All these wires or tubules can be removed from their host matrix layer using an appropriate solvent or etchant.

As an example, thin nanopore SiO_2 layers integrated into silicon wafers are of special interest for nanotechnology. For instance, in order to create optical devices with the optical confinement of photon crystals [7] or the 'moth-eye' anti-reflection effect [8], it is necessary to improve the insulator nanostructuring technique. A combination of lithography and reactive-ion etching has been used for the creation of nanostructures in SiO_2 [9]. However, trenches formed by reactive-ion etching sometimes have rough sidewalls because of the use of corrosive gases, which can degrade the device characteristics. A possible solution to this problem may be the SHI irradiation of SiO_2 aimed to latent track creation. To control the formation and etching of latent tracks and achieve a reproducible fabrication of SiO_2 layers with a high (up to $10^{10}-10^{12}$ cm^{-2}) density of nanochannels with a regular shape, it is very important to evaluate the crucial factors determining both mentioned processes.

SHI irradiation has also been of great interest in recent years due to its capacity to tune the material properties. It is possible to modify thin films, interfaces, and nanostructures embedded in a solid matrix by means of SHI irradiation. Examples of SHI irradiation-assisted modification in thin films are the appearance of room-temperature ferromagnetism in ZnO [10] or crystallization of amorphous SnO_2 layers and the formation of regular structures on an SnO_2 surface [11, 12]. The authors of Refs [13–15] have reported that the shape of Ag, Au, and Co nanoparticles changes from spherical to conical or elongated along the SHI beam direction. The possibility of SHI beam-induced dissolution and precipitation of Si nanoclusters in silicon nitride and silicon dioxide matrices was claimed recently [16, 17].

With some materials, most often with insulators, this technique is used to create various filters and microdiaphragms, as well as to fabricate nanochannel structures for electronics, photonics, and optics. A more extensive review of SHI applications is presented in Section 6.

Our first review [1] of track formation by SHI irradiation covered a broad range of topics on track formation in metals, semiconductors, and inorganic dielectrics. It was shown that the morphology of tracks depends on the type and structure of the material and on the spatial density of energy transferred to its electron subsystem. There are, however, a few contradictory models of track formation mechanisms, and most of them are still viable. The mechanisms that cause track formation and structural modifications resulting from the excited electronic states have been a topic of debate for many years. They range from the Coulomb explosion mechanism to the inelastic thermal spike model, as well as excitonic and soliton mechanisms.

Here, we review the current state of research of processes and mechanisms of track formation in solids irradiated by SHIs, including in polymers. Micro- and nanostructuring of solids by SHIs and the application of ion tracks are the main topics of this review.

2. Evolution of swift ion tracks

2.1 Spatial distribution of energy deposited by swift ions in solids

A swift heavy ion ($M_1 > 10M_{\text{proton}}$, $E \geqslant 1$ MeV a.m.u.$^{-1}$, where M_1 and E are the ion mass and energy) in solids loses its energy primarily to electron stopping, while the nuclear stopping is orders of magnitude lower. In general (for molecules, gases, liquids, or solids), the electronic energy loss is made of the ionization and excitation energy loss by the primary ion and by recoil atoms [18]. In the case of ionization energy loss, the deposited energy is taken to be equal to the binding energies of the ejected electrons. The excitation part of the inelastic energy loss of ions in solids consists of single-particle and plasmon excitations [18].

The ejected electrons are decelerated by inelastic and elastic collisions, forming a cascade of secondary (tertiary, etc.) electrons as they lose their energy and slow down to thermalization. The lateral and temporal dimensions of such cascades characterize the track structure. The large amount of energy deposited along the SHI trajectory results in extreme excitation of the electron subsystem of the solid in the nanometric vicinity of the SHI path. The spectrum of single-particle energy loss is determined by the type (metal, semiconductor, or insulator) and structure of the medium and does not depend on the type of the moving charged particle. When a plasmon state is excited, the energy absorbed by the solid is delocalized over an ensemble of atoms (molecules). The size of the delocalization region compared with the distance from the ion trajectory is $b_{\text{pl}} = v/\omega_{\text{pl}}$ (where v is the ion velocity and ω_{pl} is the plasmon frequency). Because of the Coulomb interaction, the electron density in the electron subsystem of the medium starts oscillating with the plasmon frequency [18]

$$\omega_{\text{pl}} = \left(\frac{4\pi n e^2}{m}\right)^{1/2}, \qquad (2.1.1)$$

where e and m are the charge and mass of the electron, and n is the valence-electron density of the medium.

In molecular media (e.g., polymers), the collective electron oscillations occur not in pure form but always in combination with intramolecular transitions [19]. That is why plasmon-type collective excitations take the form of longitudinal polarization waves in such media. The energy of excitation of such collective states is typically equal to 15–25 eV.

For ion energies in the range 1–100 MeV a.m.u.$^{-1}$, about 30–40% of the total stopping power is deposited in primary excitations and ionizations of the medium atoms [19–23]; the rest goes into the kinetic energy of ejected electrons, often called δ-electrons. Different media, according to the model discussed in Ref. [20], do not alter these values significantly. Thus, δ-electrons take part in transporting the energy lost by the incident heavy particle to other parts of the solid. Because the main mechanism of primary energy deposition operates via electron excitation, the deposited energy is strongly localized ($\leqslant 1$ nm) [18]. Knowledge about the localized region is very desirable for predicting the possibility of the subsequent latent track formation.

The central region of the track, where the processes of electron excitations prevail, is called the core or physical core. The lateral extension of the core is directly proportional to the velocity of the ion in a wide velocity range [21–23]. According to current views, a swift heavy ion gives rise to a cone-shaped continuous or discontinuous track consisting of the core and the surrounding sheath (or penumbra). Actually, there is no well-defined boundary between these two regions. In [24], the expression for the radius of the core was proposed in the form $r_c = \pi v/\omega_{01}$ (where v is the ion velocity and $\hbar\omega_{01}$ is the lowest energy of the electron transition in molecules or atoms), which is derived from the formula describing the probability of excitation of a molecule as a function of the impact parameter. In [25], the core radius was given by the formula $r_c = v/\omega_{pl}$. For nonrelativistic ions, r_c in insulators was given in [26] as $r_c = \hbar v/2E_{gap}$ (where E_{gap} is the energy gap between the valence and conduction bands). The first presented expression is a suitable version of r_c for molecules and water [19, 27] and two others for solids [28, 29].

The δ-electrons also cause electron excitation and ionization events, mostly outside r_c. The maximum range of δ-electrons can be calculated as [27]

$$r_{max}\ [\mathrm{g\ cm^{-2}}] = kW_{max}^2\,, \tag{2.1.2}$$

where $k = 6\times10^{-6}$ g cm^{-2} (keV)$^{-\alpha}$, $\alpha = 1.097$ for $W_{max} < 1$ keV, and $\alpha = 1.677$ for $W_{max} > 1$ keV. In many cases, it is convenient to express the depth in nm rather than in g cm^{-2}: r_{max} [g cm^{-2}] $= 10^5 r_{max}$ [nm] d [g cm^{-3}], where d is the density of the target material. Here, W_{max} is the maximum energy of δ-electrons, which is derived from the kinematics of head-on ion–electron collisions in the solid as

$$W_{max} = \frac{4Mm}{(M+m)^2}\,E_{ion} \approx 2mv^2\,. \tag{2.1.3}$$

A schematic illustration of such processes is presented in Fig. 1 [28], where the radial range of δ-electrons is indicated by r_p, which is called the penumbra (or sheath) radius. Moreover, the spectrum of secondary electrons initiated by the fast ejected electron extends to the energy $E_{max}^{\delta} = E_e/2 - I_c$, where E_e is the energy of the incident electron and I_c is the ionization energy of the medium. Because a higher knock-on electron energy yields a smaller angle of ejection, r_p is always smaller than r_{max}. The r_p value can be calculated by taking the velocity and the energy of δ-rays in the radial direction to be $V_\delta = v_{max}\cos\theta$ and $W \approx W_{max}\cos^2\theta$ and assuming that the maximum momentum is transferred to electrons in the radial direction at the scattering angle of $\pi/4$.

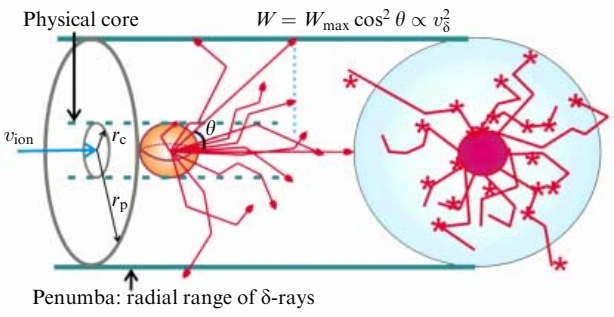

Figure 1. Artist's presentation of an ion track, which shows the physical core r_c, penumbra r_p, and δ-rays. W and r are the kinetic energy and the range of δ-rays [28].

Hence, for $\alpha = 1$, we obtain $r_p \approx r_{max}/(2\sqrt{2})$ using $r_\delta \approx kW$ and $W \approx W_{max}\cos^2(\pi/4)$.

Explicit analytic expressions for the energy densities in the core and penumbra as functions of dE/dx (the mean energy loss per unit path length or, in other words, linear energy transfer, LET) were given in [21]:

$$\varepsilon_c = \frac{(dE/dx)_e}{2\pi r_c^2}\left(1 + \frac{1}{1+2\ln(r_p/r_c)}\right), \quad r = r_c\,, \tag{2.1.4}$$

$$\varepsilon_p = \frac{(dE/dx)_e}{2\pi r^2\left(1+2\ln(r_p/r_c)\right)}\,, \quad r_c \leqslant r \leqslant r_p\,, \tag{2.1.5}$$

where r is the radial distance from the trajectory. Using expressions (2.1.4) and (2.1.5), we obtain the fraction of the total energy dissipation within a cylinder of radius r as

$$F = 0.5 + \frac{1+2\ln(r/r_c)}{2\left(1+2\ln(r_p/r_c)\right)}\,. \tag{2.1.6}$$

The energy density within the core r_c is mostly from glancing ion–electron collisions and a small fraction of low-energy knock-on (secondary) electrons that are trapped inside the core [the second term in (2.1.4)]. These equations can be used for a first estimate of electron energy densities inside and outside r_c. They also reflect the fact that the core always contains more than a half of the total energy dissipated by the SHI in the solid.

As the moving ion slows down, the dimensions of the core and the shell decrease. We note that the radial contraction of the track proceeds in such a way that the penumbra contracts faster than the core.

A software for calculating the radial energy distribution in the track, $\varepsilon(r)$, was developed in [19]. For practical applications, $\varepsilon(r)$ is represented by the approximate formula [19]

$$\varepsilon(r) = \frac{B}{r^2}\left(1 - \frac{r}{r'}\right), \tag{2.1.7}$$

where the coefficient B is obtained from the normalization condition

$$\int_a^{r'} 2\pi r\varepsilon(r)\,dr = \left(\frac{dE}{dx}\right)_e\,. \tag{2.1.8}$$

Here, $r' = r_\delta \approx 0.31 r_{\delta\,max}$ if the penumbra size is greater than the core size ($r_\delta > r_c$), and $r' = r_c$ if $r_\delta \approx r_c$. At $r' \gg a$ [where a is the size of the molecule (atom)], the normalization coefficient is

$$B \cong \frac{(dE/dx)_e}{2\pi\ln(r'/ae)}\,. \tag{2.1.9}$$

To predict the phenomenon of multiple upsets induced by a single ion in submicron electronic devices, a model based on the dielectric function theory was presented for calculating the track structure of SHIs in silicon [22]. A Monte Carlo code that simulates the transport of all (primary and secondary) particles in the framework of the event-by-event procedure, was used. The calculated histogram of the deposited doses as a function of the radial distance r from the ion trajectory was fitted by a function $\varepsilon(r)$ with energy-dependent parameters:

$$\begin{aligned}\varepsilon(r) &= C_1(E)f(r)r^{-2.308} \text{ for } 0.16\text{ nm} \leqslant r < 10\text{ nm}\,,\\ \varepsilon(r) &= C_2(E)f(r)r^{-2.055} \text{ for } 10\text{ nm} \leqslant r < 100\text{ nm}\,,\end{aligned} \tag{2.1.10}$$

where E is the ion energy expressed in MeV a.m.u.$^{-1}$, and ε and r are in Gy and nm. For energetic protons, $C_1(E) = 1.421 \times 10^5 E^{-0.913}$, $C_2(E) = 9.137 \times 10^4 E^{-0.9404}$, and $f(r) = 1.124 - 0.223r + 0.03656r^2 - 0.00156r^3$.

To obtain $\varepsilon(r)$ for heavier ions, Eqns (2.1.10) should be multiplied by $Z_{1,\mathrm{eff}}^2$, where $Z_{1,\mathrm{eff}}$ is the effective charge of the ion, related to the ion charge Z_1 by the formulas

$$Z_{1,\mathrm{eff}} = Z_1\left[1 - \exp\left(-125\beta Z_1^{-2/3}\right)\right], \qquad \beta = \frac{\left[E(E+1876.6)\right]^{1/2}}{E+938.3}, \tag{2.1.11}$$

where $\beta = v/c$, v is the ion velocity and c is the speed of light.

The results of calculations in accordance with Eqns (2.1.5), (2.1.7), and (2.1.10) confirm the conclusion that the energy density distribution $\varepsilon(r)$ drops faster than r^{-2} at all radial distances. Moreover, we note that the highest value of the deposited energy is observed in the central cylindrical region, around the ion trajectory confined within the radius $r_c \approx 4-5$ nm [19, 22, 23]. Beyond this radius, the energy density falls off very rapidly (by two orders of magnitude or more).

Based on such considerations, Kaplan and Miterev [24] believe that the characteristic $\varepsilon(r \leqslant 4\ \mathrm{nm})$ can be a measure of the intensity of radiation disturbances in the central region of the track, and therefore this characteristic is the argument of the function that describes the rate of etching of the dielectric along the track.

We now consider how the inelastic energy loss of SHIs, $(\mathrm{d}E/\mathrm{d}x)_e$, can be found. In 1930, Bethe developed a quantum theory for the energy loss of fast particles [30, 31]; he based his theory on the use of the Born approximation to calculate the differential cross section. For the interaction of a heavy particle ($M_1 \gg m$) with medium atoms, the general formula is

$$\left(\frac{\mathrm{d}E}{\mathrm{d}x}\right)_e = \frac{4\pi Z_{1,\mathrm{eff}}^2 e^4 N Z_2}{mv^2} \ln\left|\frac{2mv^2}{I}\right|, \tag{2.1.12}$$

where Z_2 is the atomic number of target atoms, N is the atomic density of the medium, and I is the geometric mean of the ionization potentials of the various shells of the atoms. The I value for an atom is defined as

$$\ln I = \sum_n f_n \ln E_n, \tag{2.1.13}$$

where the sum runs over all values of the excitation energies E_n of the atom and the oscillator strengths f_n obey the Thomas–Kuhn sum rule

$$\sum_n f_n = 1. \tag{2.1.14}$$

If the spectral distribution of the oscillator strengths is known, I can be calculated [18].

Using simple statistical estimates, Bloch showed in [32] that in the Thomas–Fermi theory,

$$\frac{I}{Z_2} \approx \varepsilon_{\mathrm{Ry}}, \tag{2.1.15}$$

where $\varepsilon_{\mathrm{Ry}}$ is the energy equal to one Rydberg (1 Ry = 13.6 eV).

A frequently used expression for $Z_{1,\mathrm{eff}}$ was given in [33]:

$$Z_{1,\mathrm{eff}}^{\mathrm{B}} = Z_1\left[1 - \exp\left(-125\beta Z_1^{-2/3}\right)\right], \tag{2.1.16}$$

where Z_1 is the ion atomic number and $\beta = v/c$. There are other expressions for $Z_{1,\mathrm{eff}}$, like the one proposed in [34], which depends on both Z_1 and the target atomic number Z_2. In silicon ($Z_2 = 14$), the ratio $R = (Z_{1,\mathrm{eff}}^{\mathrm{SG}}/Z_{1,\mathrm{eff}}^{\mathrm{B}})^2$ increases with increasing Z_1 and decreasing the ion energy E, reaching the maximum value $R \approx 2.5$ [35]. That is why errors can occur in the calculated inelastic energy losses presented in the tabulations such as SRIM [36], ICRU [37], CasP [38], Geant [39], and others.

To describe the primary process of δ-electron ejection in a solid and the energy spectra of these electrons, different approaches are used: the classical binary encounter approximation (BEA) [40–43], the quantum mechanical perturbative plane-wave Born approximation (PWBA) [44, 45], and the complex dielectric function (CDF) [46–48]. The first two assume that a solid target consists of dynamically independent atoms, and collective effects in the electron subsystems of a solid are not considered in such approximations. On the contrary, the CDF formalism takes into account collective modes of electron excitations resulting from spatial and temporal correlations in the electron ensemble.

A simplified version of the BEA for the energy spectrum of δ-electrons ejected in the collision of an ion with target-atom electrons was proposed in [40]:

$$\frac{\mathrm{d}\sigma}{\mathrm{d}E} = \frac{2\pi e^4 Z_2 Z_{1,\mathrm{eff}}^2}{m_0 c^2 \beta^2 E^2} \times\left[1 - \frac{\beta^2 E}{E_{\max}} + \frac{\pi\beta Z_{1,\mathrm{eff}}^2}{137}\left(\frac{E}{E_{\max}}\right)^{1/2}\left(1 - \frac{E}{E_{\max}}\right)\right], \tag{2.1.17}$$

where $\mathrm{d}\sigma$ is the differential cross section of the process whereby an ion with an energy E_i (in MeV a.m.u.$^{-1}$) transfers energy E to the ejected electron from the n-shell, β is the ion velocity v in units of light velocity, m_0 is the electron rest mass, and $E_{\max}$ is the maximal energy transferred to the electron in the ion–electron collision, i.e., $E_{\max} = E_{\delta\,\max} + E_{\mathrm{bn}}$, with E_{bn} being the binding energy of the electron in the n-shell. The maximal kinetic energy of the ejected electron is

$$E_{\delta\,\max} = 2m_0 c^2 \beta^2 (1-\beta^2)^{-1}, \tag{2.1.18}$$

or, for nonrelativistic electrons, as we saw in Eqn (2.1.3), $2m_0 v^2$.

A simplified version of Eqn (2.1.17) is used in Geant 4 computer code [39] for the δ-electron spectrum:

$$\frac{\mathrm{d}\sigma}{\mathrm{d}E} = \frac{2\pi r_0^2 m_0 c^2 Z_2 Z_{1,\mathrm{eff}}^2}{\beta^2 E^2}\left[1 - \frac{\beta^2 E}{E_{\max}} + \frac{E^2}{E_{\max}^2}\right], \tag{2.1.19}$$

where $E = E_\delta + E_{\mathrm{bn}}$ and r_0 is the classical electron radius ($r_0 = 2.818 \times 10^{-13}$ cm). The ejected electron is assumed to be initially at rest in both formulas.

The differential cross section $\mathrm{d}\sigma_v/\mathrm{d}W$ associated with an energy transfer W was calculated in [44, 45]:

$$\frac{\mathrm{d}\sigma_v}{\mathrm{d}W} = 8\pi\overline{Q}_{\mathrm{p}}^2\left(\frac{e^4}{v^2}\right)\frac{a_0^2}{Z_v}\int_{Q_{\min}}^{\infty}\mathrm{d}Q\ \frac{\left|F_v(W,Q)\right|^2}{Q^2}, \tag{2.1.20}$$

where a_0 is the Bohr radius, $W = T/(Z_v^2\,\mathrm{Ry})$, T is the energy transfer, $Z_v = Z_2 - \xi$ is the target-atom screening charge, ξ is the Slater screening parameter [49],

$$Q_{\min} = \frac{W^2 M_1 Z_v^2\,\mathrm{Ry}}{4mE} \approx \frac{W}{4\eta_v}, \qquad \eta_v = \frac{mE}{M_1 Z_v^2\,\mathrm{Ry}},$$

E and M_1 are the ion energy and mass, and $|F_v(W,Q)|$ is the form factor that depends on the electron shell configuration (1s, 2s, 2p1/2, 2p3/2, etc.). Its values have been determined in Ref. [50] for hydrogenic orbitals. Very often in calculations, a point-like constant charge $\overline{Q}_\mathrm{p}$ is assumed in the presentation of the ion structure [51].

We note that the PWBA approximation is valid for a week perturbation, when the criterion

$$K = \frac{Z_1}{Z_2}\,\frac{v_\mathrm{e}}{v} \ll 1 \tag{2.1.21}$$

is satisfied [18], where v_e is given by the virtual theorem, $(1/2)mv_\mathrm{e}^2 \approx B_v$, and B_v is the electron binding energy, which means the applicability of such an approach for high-velocity and nearly fully stripped ions. The PWBA treatment can be extended to medium-energy ions by renormalization to the experimental $(\mathrm{d}E/\mathrm{d}x)_\mathrm{e}$ [39, 51] through a phenomenological mean effective charge $\overline{Q}_\mathrm{p}$.

The statistical energy deposition (SED) model is also used for calculations of multiple ionization cross sections of atoms and molecules by fast ions [52], as well as for calculations of the radial distribution of the deposited energy density in ion tracks [53].

The CDF is a first-order Born approximation, which has been used in many studies to calculate the interaction cross section of charged particles with the electron subsystem of solids [22, 46–48, 54–58]. The cross section of scattering of a charged particle (ion, ejected electron) on the strongly correlated electron subsystem of a solid is given by the cross section of scattering on an individual electron times the dynamic structure factor of the electron subsystem [59]. This dynamic structure factor is expressed in terms of the inverse imaginary part of the complex dielectric function $\varepsilon(\omega,g)$ of the medium [46, 48, 54]. Then the double differential cross section per the transferred energy $\hbar\omega$ and the momentum $\hbar g$ is

$$\frac{\mathrm{d}^2\sigma}{\mathrm{d}(\hbar\omega)\,\mathrm{d}g} = \frac{2Z_{1,\mathrm{eff}}^2\,e^2}{n\pi\hbar^2v^2}\,\frac{1}{g}\,\mathrm{Im}\left[\frac{-1}{\varepsilon(\omega,g)}\right], \tag{2.1.22}$$

where $Z_{1,\mathrm{eff}}$ is replaced with $Z_\mathrm{e} = 1$ in the case of a moving electron, v is the velocity of the incident particle, $\hbar$ is the Planck constant, and $n = n_\mathrm{e}$, the density of electrons for inelastic scattering (impact ionization), or $n = N$, the density of atoms for elastic scattering (kinetic energy transfer without electron excitation in the target).

The CDF cross section for energy transfer is given by [56]

$$\frac{\mathrm{d}\sigma}{\mathrm{d}E} = \frac{2Z_{1,\mathrm{eff}}\,e^2}{\pi N\hbar^2v^2}\int_{g^-}^{g^+}\frac{1}{g}\,\mathrm{Im}\left[\frac{-1}{\varepsilon(\omega,g)}\right]\mathrm{d}g\,, \tag{2.1.23}$$

where N is the atomic density of the target, $g^- = \omega/v$, and $g^+ \approx E_\mathrm{max}^{1/2}$. The function $\mathrm{Im}[-1/\varepsilon(\omega,g)]$ is called the energy loss function. Moreover, the energy loss of a projectile (ion or electron) is given by the first moment of the mean free path λ [57]:

$$\left(\frac{\mathrm{d}E}{\mathrm{d}x}\right)_\mathrm{e} = \int_{E_\mathrm{min}}^{E_\mathrm{max}}\frac{\mathrm{d}\lambda^{-1}}{\mathrm{d}(\hbar\omega)}\,\hbar\omega\,\mathrm{d}(\hbar\omega)\,. \tag{2.1.24}$$

Here, $\lambda = n\sigma^{-1}$ is the mean free path of an individual particle for elastic and inelastic scattering cross sections, $E_\mathrm{min} = E_\mathrm{g}$ (where E_g is the band gap for inelastic scattering), $E_\mathrm{max} = \hbar\omega_\mathrm{max} = 4EmM_1/(M_1+m)^2$ for an incident ion, and $E_\mathrm{max} = E/2$ for an electron, taking the identity of electrons into account. In metals and semi-metals, assuming a free electron gas of valence electrons, $E_\mathrm{min} = \hbar\omega_\mathrm{min}$ can be estimated as [60]

$$\omega_\mathrm{min} = \frac{Z_{1,\mathrm{eff}}^2\,e^4}{4\pi\varepsilon_0^2b_\mathrm{max}^2\omega_\mathrm{max}^2 + Z_{1,\mathrm{eff}}^2\,e^4}\,\omega_\mathrm{max}\,, \tag{2.1.24$'$}$$

where ε_0 is the dielectric permittivity and b_max is limited in such materials by conduction electron screening and, in accordance with the Mozumder treatment [26], $b_\mathrm{max} = 1.12v_\mathrm{ion}/\omega_\mathrm{pl}$.

The integration limits for the moments in the double differential inverse mean free path,

$$\frac{\mathrm{d}\lambda^{-1}}{\mathrm{d}(\hbar\omega)} = \int_{g^-}^{g^+}\frac{\mathrm{d}^2\lambda^{-1}}{\mathrm{d}(\hbar\omega)\,\mathrm{d}(\hbar g)}\;\mathrm{d}(\hbar g)\,,$$

are given by [48]

$$\begin{aligned} g^\pm &= \sqrt{\frac{2m}{\hbar^2}}\,\left(\sqrt{E} \pm \sqrt{E-\hbar\omega}\right) \text{ for electrons}\,,\\ g^- &= \frac{\omega}{v}\,,\quad g^+ = \frac{\sqrt{2mE_\mathrm{max}}}{\hbar} \text{ for ions}\,. \end{aligned} \tag{2.1.25}$$

The calculated cross sections of the SHI and electron scattering are then incorporated into a Monte Carlo model describing the electron kinetics in SHI tracks in a solid [20, 35, 51, 55, 57, 58]. In the case of semiconductors and dielectrics, such an approach allows simulating ionization of a solid by an incident ion as well as secondary electron cascades produced by primary electrons and Auger decays of holes in deep atomic shells.

We also note that the results of such calculations based on BEA, PWBA, SED, and CDF theories show a significant difference in spectra of low-energy δ-electrons ($\leqslant 100$ eV) [61]. This difference is due to the changes in the outer shell electron density distribution of the target atoms in passing from free atoms to a solid material. It was shown in [58] that the SHI energy losses are also affected by the material structure (amorphous or crystalline) for SHI energies around the Bragg peak (about 10–15% difference). Such differences cannot be captured within free-atom approximations such as SRIM [36], CasP [38], or Geant [39]. The SRIM code [36], which is often used for data interpretation in track physics, combines the system by Brandt and Kitagawa [62] for $(\mathrm{d}E/\mathrm{d}x)_\mathrm{e}$ with the effective-charge model and an empirical screening radius. The SRIM results normally come close to experimental data whenever such data exist [63]. We also note that the credibility of SRIM predictions can decrease dramatically in regions of the (Z_1, Z_2, E) parameter space that are not covered by experimental data (see Fig. 13 in Ref. [63]). An extended discussion of this topic and a critical examination of the existing theories on swift-ion energy loss are presented in recent paper [63]. Most of the ion-track studies have been done at kinetic energies between 1 and 10 MeV a.m.u.$^{-1}$, where the electron stopping power S_e is maximal.

2.2 Spatio-temporal evolution of ion tracks

2.2.1 Charge neutralization time. Excitation times for inner-shell electron processes are 10^{-19} to 10^{-17} s and reach 10^{-16} s for plasmon production. After these initial ionization and excitation events, the electron system evolves further. Some of

the δ-electrons initially excited by heavy ions escape and the center of the track is highly ionized. A plasma model of the SHI interaction with solids, developed in Ref. [64], predicts that a track core is formed in the time $\tau_0 \sim 10^{-17}$ s. The timescale of electron–hole pair production by a fast ion in semiconductors and insulators depends on the electron impact ionization rate and amounts to ~ 10 fs [65]. Depending on the ionization density and on the charge-neutralization time, the mutual repulsion of positively charged target ions in the core of tracks can convert a significant amount of the stored potential energy into atomic motion (Coulomb explosion model [3]). A strong electric field attracts the emitted δ-electrons and returns them to the core region. Therefore, the existence of a strong electric field in the track core is controlled by the neutralization time Δt_n.

The perturbation theory predicts neutralization times of about 10^{-16} s ($\Delta t_n \sim \omega_{pl}^{-1}$) for a weak and homogeneous charge displacement in metals such as Al.

Two models are often used to describe characteristic neutralization times: a simple Maxwell charge neutralization model, which determines the space charge relaxation based on local conductivity, and a plasma model, which evaluates space charge neutralization by using a set of equations for carrier mobilities and annihilation, recombination of carriers by Auger processes, ambipolar diffusion, conductive drift in space [51, 66], and impact ionization by a high electric field. This time can be calculated by solving the static Maxwell equations for the electric field **E**, the current density **j**, and the conductivity σ [66]:

$$\begin{aligned} &\operatorname{div}\mathbf{E} = \frac{\rho}{\varepsilon\varepsilon_0} = \frac{e\Delta n}{\varepsilon\varepsilon_0}\,, \\ &\operatorname{div}\mathbf{j} = -\frac{\partial\rho}{\partial t}\,, \\ &\mathbf{j} = \sigma\mathbf{E}\,. \end{aligned} \tag{2.2.1}$$

In the one-dimensional case, the solution of Eqns (2.2.1) can be represented as

$$\begin{aligned} &N_g(t) = N(0)_n \exp\left(-\frac{t}{\Delta t_n}\right), \\ &\Delta t_n = \varepsilon\varepsilon_0\sigma\,, \end{aligned} \tag{2.2.2}$$

where $N_g(t) = \rho V$ is the total number of charges at a time t, ε and ε_0 are the respective electric permittivities of the target material and the vacuum, V is the volume of the plasma region, and ρ is the excessive charge density in this volume.

Table 1 illustrates the neutralization times calculated for different materials according to Eqns (2.2.1) and (2.2.2). These data can be used as a crude estimate of a range of reliable values.

Table 1. Neutralization times of various materials obtained from the Maxwell relaxation [66].

Materials	Conductivity, $(\Omega\ \mathrm{m})^{-1}$	Neutralization time, Δt_n, fs
Cu	5.88×10^7	0.01
Al	3.77×10^7	0.024
W	1.89×10^7	0.1
Ni	1.43×10^7	0.13
Si	100	10^3
LiF	10^{-4}	10^9

Coulomb explosion would be noticeably developed if the charge-neutralization time exceeds 10^{-14} s for targets containing light atoms and 10^{-13} s for materials consisting of heavy atoms [3, 67–69]. Therefore, for most metals, charge neutralization is a very fast process and Coulomb explosion is impossible. This conclusion is also supported by the data in Table 1.

The core-track potential resulting from the charge separation in the ion track gives rise to decelerated convoy electrons [70, 71] and manifests itself in the surface scattering of molecules [72] or a strong energy reduction of target Auger electrons (mylar and polypropylene [73]) in the sub-fs and fs time range. This effect is found mainly for large-band-gap insulators, where electrons can be trapped and holes have low mobility. It can be estimated that a strong ion-track potential existing for more than 10 fs would lead to atomic motion of atoms [70, 71, 73].

The measured broadening of Auger electron peaks caused by the track-core potential can be related to the 'electron temperature' concept suggested in [73–77]. The energetic position and width of Auger lines yields different snapshots of the short-time evolution, some 1 fs after the passage of SHIs. For many examined materials, such as metals (Al and a few metallic glasses) and semimetals (C and Be), such track potentials have not been revealed [77]. From the experimental standpoint, this means that the core-track potential for these materials is below the experimental resolution limit $\pm(0.2-0.5)$ eV [69, 76, 77]. This also indicates that the neutralization time of the ion track in such materials should be smaller than the Auger-decay time of 10^{-14} s. Typical Auger-decay times are 11 fs for carbon K^1VV and 15 fs for silicon $2p^1VV$ lines. For multiple inner vacancy lines, the decay times are significantly reduced. For amorphous Si targets, Auger-energy reductions that maximize for short decay times reaching 3 eV for SHIs were observed in [76]. This relatively small effect (compared to 42 eV for swift Ne ions in polypropylene) is due to a very slow component of the core-track potential with $\Delta t_{track} > 30$ fs. This small shift of only 3 eV indicates a rapid electron neutralization of the track in an Si target. Such a value can be expected, considering the high mobilities of carriers in this material. The observed shift of Auger lines can be related to a very slow component caused by long-lived traps for electrons and holes. With the so-called Onsager radius $r_c = e^2/(\varepsilon k_B T)$ [78] taken as a criterion of the electron–hole distance within which recombination occurs ($\varepsilon = 11.9$ is the silicon permittivity, k_B is the Boltzmann constant, and T is the temperature), the value $r_c = 4.7$ nm was established in [22]. For this value of r_c, it was estimated in [22] that more than 90% of the carrier pairs promptly recombine, thus significantly reducing the track-core potential.

Hence, in semiconductors, the charge-neutralization time is a material and phase (amorphous or crystalline) [76] parameter and its value is considerably lower than in insulators. In [76], a comparison of the Auger electron spectra for amorphous and crystalline Si revealed a phase effect in the short-time dynamics of ion tracks, including for the track-core potential but not for the electron temperature (10,000–20,000 K) determined from these data. According to the interpretation in [76], the charge neutralization can be suppressed by 50% in amorphous Si compared to crystalline Si targets.

The neutralization time in semiconductors can be estimated from the Debye screening length by considering the

mobility of carriers [79]

$$\Delta t_{\rm n} = \frac{\varepsilon_0 \varepsilon}{g \mu_{\rm n}^*(T_{\rm L}, T_{\rm n}) n} , \qquad (2.2.3)$$

where $\mu_{\rm n}^*$ is given by [80]

$$\frac{\mu_{\rm n}^*(T_{\rm L}, T_{\rm n})}{\mu_0^*(T_{\rm L})} = \left[1 + \frac{3}{2} \frac{\mu_0^*(T_{\rm L}) k_{\rm B}}{g \tau_{\rm n} v_{\rm sat}^2} (T_{\rm n} - T_{\rm L})\right]^{-1} , \qquad (2.2.4)$$

and $T_{\rm L}$ is the lattice temperature, $\mu_{\rm n}^*$ is the mobility of hot electrons, n is the electron–hole density, μ_0^* is the mobility of electrons in the initial lattice, $v_{\rm sat}$ is the saturation speed, and $\tau_{\rm n}$ is the energy relaxation time for electrons. We note that in silicon, the energy relaxation times for electrons and holes, $\tau_{\rm n}$ and $\tau_{\rm p}$, are equal and are between 0.15 and 0.4 ps [81, 82]. Assuming a cold lattice with $T_{\rm L} = 300$ K and a hot electron–hole plasma with $T_{\rm n} = 10{,}000$ K, the electron–hole density $n = 10^{21}$ cm^{-3}, $\varepsilon = 11.9$, and $\tau_{\rm n} = 0.20$ ps and taking the data for crystalline silicon from the literature, $\mu_0^*(300\ {\rm K}) = 1430$ cm^2 V^{-1} s^{-1} and $v_{\rm sat} = 10^7$ cm s^{-1} [83], we obtain $\mu_{\rm n}^* \approx 0.15$ cm^2 V^{-1} s^{-1} and $\Delta t_{\rm n} = 0.45$ fs.

We estimate the neutralization time in quartz irradiated with SHIs. According to a simple consideration presented in Ref. [65] for semiconductors and dielectrics, adding the average kinetic energies of electrons $\overline{E}_{\rm n}$ and holes $\overline{E}_{\rm p}$ in the track core gives

$$\overline{E}_{\rm n}(r, t_0) + \overline{E}_{\rm p}(r, t_0) \approx 2E_{\rm gap} , \qquad (2.2.5)$$

where $E_{\rm gap} = 12$ eV for quartz, r is the distance from the ion trajectory, and t_0 is the time at which the Boltzmann statistics is applicable to the electron–hole plasma ($t_0 \approx 10$ fs). An interesting feature of relation (2.2.5) is that the average kinetic energy per electron–hole pair is independent of the distance r from the center of the track core. Taking into consideration that for quartz $\overline{E}_{\rm p} \approx 0.5\overline{E}_{\rm n}$ [84], this results in the electron temperature $T_{\rm n} = 8E_{\rm gap}/(9k_{\rm B}) \approx 1.2 \times 10^5$ K and the hole temperature $T_{\rm p} \approx 4E_{\rm gap}/(9k_{\rm B}) \approx 0.6 \times 10^5$ K. Using $\mu_0^*(300\ {\rm K}) = 20$ cm^2 V^{-1} s^{-1} [85], $v_{\rm sat} \approx 2 \times 10^7$ cm s^{-1} [86], $\varepsilon = 2.4$, and $T_{\rm n} = 1.2 \times 10^5$ K, we obtain $\mu_{\rm n}^* \approx 0.19$ cm^2 V^{-1} s^{-1} and $\Delta t_{\rm n} = 2.2$ fs from Eqns (2.2.3) and (2.2.4). Therefore, only a small track potential is expected for a quartz target due to a very short neutralization time.

Strictly speaking, this approach can be applied to the electron–hole plasma under the assumption of the Boltzmann statistics (with $t_0 \approx 10$ fs). The above estimate is therefore very rough for $\Delta t_{\rm n} < t_0$. As we show in Sections 2.2.2, 4.2, and 4.3, the electron and hole neutralization times $\tau_{\rm ee}$ and $\tau_{\rm hh}$, as well as the electron–phonon thermalization time, must be estimated separately.

2.2.2 Electron–electron, electron–phonon, and lattice thermalizations. The relaxation of the intense electron excitations caused by bombardment of a solid with high-energy ions is the main factor determining the nature of the track region. In many pure coarse-grained metals (with the grain size much larger than the electron mean free path), the relaxation of electron excitations in the track region is determined by the electron heat conductivity. The energy transfer from hot to cold electrons increases the radius of the excitation region and decreases the electron temperature inside this region.

In general, if the concentration of excited electrons is sufficiently high, they first very efficiently exchange their energies. According to the plasma model discussed in Ref. [87], the time of relaxation of the electrons to the equilibrium distribution is

$$\tau_{\rm ee} = \frac{5}{8} \left[\frac{m(k_{\rm B}T_{\rm e})^3}{\pi}\right]^{1/2} (e^4 n_{\rm e} \ln \lambda_{\rm p})^{-1} , \qquad (2.2.2.1)$$

where $\ln \lambda_{\rm p} \approx \ln(r_{\rm D}/b_{\rm min})$ is the Coulomb logarithm, $r_{\rm D} = (k_{\rm B}T_{\rm e}/4\pi n_{\rm e} e^2)^{1/2}$ is the Debye radius, $n_{\rm e}$ is the electron density, and $b_{\rm min}$ is the minimum value of the impact parameter. With the mean energy of the electrons $\bar{\omega}_{\rm e} \approx 3/2 k_{\rm B}T_{\rm e} \approx 10$ eV and $n_{\rm e} \approx 3 \times 10^{22}$ cm^{-3}, the electron relaxation time estimated by Eqn (2.2.2.1) is $\tau_{\rm ee} \sim 10^{-15}$ s.

We note that the ratio of the thermalization times in the electron and ion subsystems of the track plasma is defined in [79] as $\tau_{\rm ii}/\tau_{\rm ee} = (M_{\rm i} T_{\rm i}^3/m T_{\rm e}^3)$, and hence the initial equilibrium distribution of ions with respect to their velocities is established sooner than that for electrons, because $T_{\rm i} \approx 10^{-2} T_{\rm e}$.

Because $\tau_{\rm ee} \sim 10^{-15}$ s, the thermalization time in the ion subsystem of a solid is about 0.1 fs, which coincides with the characteristic plasmon frequency. Typical times of the atomic dynamics (phonons and atom vibration periods) are in the range $\sim 50-100$ fs. Hence, the dynamic state of the ensemble of atoms in the crystal lattice remains the same in a time of 0.1 fs.

When the concentration of electrons is $n_{\rm e} > 10^{20}$ cm^{-3}, after ~ 10 fs they can be considered a classical electron gas with the temperature $T_{\rm e}$, whence $\bar{\omega}_{\rm e} \approx 3/2 k_{\rm B}T_{\rm e}$ (where $\bar{\omega}_{\rm e}$ is the mean energy of relatively slow electrons in the framework of the Boltzmann statistics). This argument applies for $k_{\rm B}T_{\rm e} > 4$ eV and electron concentrations below $n_{\rm e} \sim 10^{22}$ cm^{-3}. Above this level, the electron gas degenerates and obeys the Fermi–Dirac statistics. For slow electrons with $E_{\rm e} < \hbar\omega_{\rm min}$ (subexcitation electrons), the thermalization time depends on the nature and the phase state of the medium and can range from 0.1 ps to 1 ns [19, 51, 88]. In crystalline silicon, such electrons with a mean kinetic energy of the order of 4 eV (i.e., of the order of the electron affinity) are not thermalized, and therefore their velocity distribution differs significantly from the Boltzmann distribution [51].

Moreover, during the process of auto-ionization, electrons with considerably higher energies (1000–3000 eV) are created in the plasma as well. The fraction of such hot free electrons is about 10–15% of the total electron number [89]. Because the thermalization times for these electrons can be longer than a few femtoseconds, it is necessary to consider the plasma with two fractions of electrons. The equilibration time of these electrons is about 30 fs [89]. Thus, this fraction of electrons should be treated separately when solving the kinetic equations for ions.

In Ref. [89], a plasma relaxation model is used to describe the excitations in solids (Al and quartz targets) by SHIs with energies of 3–11 MeV a.m.u.$^{-1}$. According to the results, the Boltzmann distribution of free electrons is established in a time $\leqslant 1$ fs at a temperature of tens of eV. For the experimental conditions used, the electron density and temperature are found to be equal to 4×10^{23} cm^{-3} and 10–50 eV. Thus, the number of electrons in the Debye sphere $N_{\rm D} = 4\pi r_{\rm D}^3 n_{\rm e}/3$ is in the range 0.14–0.32, and hence the plasma is strongly coupled in this case. The plasma coupling parameter Γ is defined as $\Gamma = (4\pi n_{\rm e}/3)^{1/3} e^2/(k_{\rm B}T_{\rm e})$. An X-ray spectral method based on the plasma relaxation model is proposed in Ref. [89] to measure the plasma temperature in the swift ion tracks.

The energy exchange through elastic collisions in the case of semiconductors and dielectrics is the main channel available for the equalization of electrons and heavy particles of the medium (ions and neutral atoms). If the rate of energy loss by such elastic collisions is $\sim 10^{-12}$ eV s^{-1}, the temperatures of electrons and ions are equalized in $\tau_{ei} > 10^{-12}$ s, and the temperatures of electrons and neutral particles, in $\tau_{en} \geqslant 10^{-11}$ s [51, 79]. The characteristic relaxation times τ_{ei} for metals and semiconductors differ substantially (see Table 2 in Ref. [1]), which speaks to the distinction in the process of track evolution in them. According to our calculations [90], the equalization times also depend on the energy spectrum of the electron excitations and the heat conductance of the material. In bulk crystalline silicon, the electron–phonon thermalization time $t_{e-ph} \sim 1$ ps is observed by time-resolved photoelectron spectroscopy using femtosecond laser pulses [91]. In fact, at a very high carrier concentration n_e, the highly excited conduction electrons of silicon behave quite similarly to that of metals [91].

In dielectrics, the Monte Carlo calculations in Refs [92, 93] demonstrate the equalization between the electron and the kinetic lattice temperatures within times $\tau_{ei} \approx 100$ fs. Such equalization times have also been observed when studying the excitation of electrons in laser-irradiated SiO_2 [94].

At the next stage of the spatio-temporal track evolution, heat conduction and energy transport by acoustic waves are the more important processes of energy removal from the track. The efficiency of heat transfer in the ambient medium is characterized by the temperature conductivity coefficient

$$\chi = \frac{\kappa}{\rho C_p}\,, \qquad (2.2.2.2)$$

where κ is the heat conduction coefficient, ρ is the density of the solid, and C_p is the specific heat capacity at constant pressure [95]. The dependence of the temperature conductivity coefficient of metals on the electron temperature, $\chi(T)$, is represented by a curve with a dip at $T_e > \varepsilon_F$ (where ε_F is the Fermi electron energy), with the minimum thermal diffusivity χ_{min} being roughly 1 cm^2 s^{-1} [1]. Moreover, the heat conductivity of typical metals is almost completely caused by the conduction electrons. The heat conduction coefficient of pure metals is very high and amounts to 403 W m^{-1} K^{-1} for silver and 210 W m^{-1} K^{-1} for aluminum [96]. The temperature conductivity coefficient of metals lies in the range from 0.21 cm^2 s^{-1} (Fe) to 1.71 cm^2 s^{-1} (Ag) [97]. Hence, the characteristic time it takes the electrons in the excited region of bulk metals to cool due to the electron heat conductivity can be estimated as

$$\tau_1 = \frac{r_c^2}{\chi_{min}} \approx 10^{-13}\ \text{s}\,, \qquad (2.2.2.3)$$

where $r_c \approx 4-5$ nm is the track-core radius.

In dielectrics, the transfer of thermal energy across the lattice is accomplished by the phonon gas. In certain semiconductors and dielectrics with rigid bonds, such as silicon, germanium, or diamond, the lattice heat conductivity is comparable to or higher than the heat conductivity of metals (137 W m^{-1} K^{-1} for silicon, 54 W m^{-1} K^{-1} for germanium, and 550 W m^{-1} K^{-1} for diamond) [96]. The temperature conductivity coefficient of such materials is comparable to χ of metals (0.53 cm^2 s^{-1} for silicon). This means that for $r_c \approx 4-5$ nm in such crystals, the excited region cools to the temperature of the surrounding lattice within $\tau_1 \approx 10^{-13}-10^{-12}$ s.

We also note that all processes in SHI tracks formed in dielectrics can be significantly prolonged due to energy storage in holes via secondary electrons [98, 99]. The energy stored in a valence hole subsystem is released due to Auger decays on a longer timescale. The delay caused by this energy storage leads to an electron–lattice equilibration time of the order of 40–50 ps [98, 99]. The accumulated energy in such holes can be up to $\sim 80\%$ of the energy loss experienced by the incoming ion [98–100].

In addition, the potential energy that is still stored in electron–hole pairs is partially released by the formation of self-trapped excitons. This is demonstrated in time-resolved studies of carrier dynamics in wide-gap materials using pulsed lasers [101, 102]. According to the results in Ref. [102], the potential energy stored in self-trapped excitons in quartz is $E_{exc} \sim 7$ eV. For the average energy $\overline{E}_{e-h}$ required to generate an electron–hole pair, the theory predicts $\overline{E}_{e-h} \approx 3E_{gap}$ [103]. Thus, the fraction of the energy not yet converted to heat in the lattice system is $7\,\text{eV}/(3E_{gap}) \approx 0.2$. This stored energy of excitons is later converted into heat in the surrounding medium or into the formation of lattice defects (E'-centers, etc.).

Some wide-gap dielectrics (Al_2O_3, MgO) do not exhibit self-trapping of excitons [101, 102] and they have to be treated in the same way as in semiconductors (Si, Ge, etc.).

In polymers, heat conductivity is much lower, $\chi = 0.03-0.8$ W m^{-1} K^{-1} [19], meaning that the temperature conductivity values in this case are three orders of magnitude lower than for metals, and they equal $(0.4-1.8)\times 10^{-3}$ cm^2 s^{-1} [104]. The characteristic time of the existence of a heated region of the size $r_c \approx 4-5$ nm in polymers is longer than $\tau_1 \sim 10^{-10}$ s. For such materials, the energy transfer by the hydrodynamic mechanism is more efficient, in view of the characteristic time $\tau_g \sim r_c/v_s \approx 3\times 10^{-12}$ s for $r_c \approx 4$ nm, where v_s is the speed of sound (in polymers, $v_s \approx 1.5\times 10^3$ m s^{-1} [104]).

The discussed processes of electron–lattice thermalization and energy removal from the track can be considered appropriate only for metals, semiconductors, and insulators with a perfect crystal lattice. If the crystal structure has defects, the cross section of the energy track is determined by the characteristic sizes of structural elements such as the grains in polycrystalline targets or interphase boundaries (if their size is smaller than the core-track radius). Many experimental results concerning the effectiveness of inelastic sputtering of fine-grained targets of thin layers on bulk substrates [1, 105, 106] corroborate this idea. If the energy in the electron subsystem is concentrated within a certain area of the solid, the lattice can become strongly heated. The electron–lattice relaxation time is also highly dependent on other microdefects of the structure, such as impurities (in semiconductors), dislocations, microtwins, and amorphous inclusions [1, 23, 107, 108]. Moreover, it is well known that in crystalline materials the phonons are practically entirely stopped or reflected at the grain boundary.

The temperature conductivity coefficient χ in single crystalline dielectrics can be represented as $\chi = l_{ph}s/3$, where $l_{ph} \sim 1/T$ is the mean free path of phonons and s is the phonon mean velocity, which is approximately the longitudinal speed of sound v_s in such materials [23]. For example, we consider BN and AlN bulk crystals, which are respectively characterized at room temperature by $l_{ph} \approx 69$

and 36 nm [23]. If we deal with polycrystalline materials, and $l_{ph} > d/2$ (where $d/2$ is the radius of the crystalline grain), l_{ph} is replaced with the effective radius of the grain. In the case of amorphous dielectrics, l_{ph} is equal to the mean interatomic distance a, and a weak dependence of l_{ph} on T is observed [23, 109]. Therefore, the temperature conductivity coefficient for nanocrystalline materials is [109]

$$\chi = \frac{ds}{6} . \qquad (2.2.2.4)$$

Hence, the characteristic time it takes the thermoelastic spike in the excited region of a nanocrystalline dielectric material to cool due to heat conductivity can be estimated as

$$\tau_{1,\,\mathrm{nanocr}} \approx \frac{6r_c^2}{ds} . \qquad (2.2.2.5)$$

This indicates that the lifetime of thermoelastic spikes in such nanostructural materials decreases as the crystalline size increases. Spatio–temporal characteristics of the thermoelastic spikes in various nanocrystalline and amorphous targets have been calculated and discussed in Refs [23, 109] and the references therein.

3. Models of track formation in solids irradiated by SHIs

Several physical models have been developed to describe the evolution of the internal electron energy (quantified as the electronic temperature, as discussed in Section 2.2.1) via displacements of target atoms toward final structural and phase modifications. A manifestation of this latter stage of track formation has been observed by HRTEM, RBS-c, SAXRS, AFM, and other facilities.

Currently, three main mechanisms of energy conversion are discussed most: Coulomb explosion or Coulomb repulsion, energy transfer via the electron–phonon coupling, and an approach based on the rupture of atomic bonds in solids caused by intense electronic excitations [110, 111]. Even if charge neutrality is reestablished in the track core, the interatomic potentials between the atoms are still different from the equilibrium potentials, because the electrons are not in their lowest states. Hence, a fraction of the electron energy leads to modified interatomic forces and subsequent atomic motion. This mechanism is called 'athermal melting' or the lattice-relaxation mechanism [110, 111]. The crystalline order decays on a time-scale of 10^{-14} s, too rapidly to be mediated by phonons. Therefore, the relative importance of these mechanisms depends on the charge neutralization time, on the strength of the track potential, on the strength of the modified interatomic forces, and on the electron–phonon coupling efficiency.

As was shown in Section 2.2.1, for most metals and semiconductors, neutralization is a very fast process and Coulomb explosion is impossible. Generally speaking, Coulomb explosion assumes a radial coherent motion of all atoms in the track core [3, 68]. Such a situation corresponds to a practically instantaneous mechanical loading of the track core, releasing an elastic wave or shock wave [19, 23, 112]. Because the plasma in the track is quasi-neutralized in a very short time (see Section 2.2.1), this mechanism of shock wave formation is not likely to operate in tracks that are located deep inside the target. Quasinuetrality can only be violated at the boundaries of the exposed medium (at the points of entry or exit of an ion). This mechanism can be justified as regards explaining the sputtering of a target from surfaces exposed to ions [105].

But even if the process starts with coherent and collective motion, collisions between atoms tend to randomize their energy, and hence thermalized motion can occur on a picosecond time scale [113]. In the framework of such an approach, Coulomb explosion and a lattice thermal spike can represent early and late stages of the latent track formation [114, 115]. Indeed, the molecular dynamics (MD) simulations of the damage caused in calcium fluoride by a swift ion show that the formed ion explosion spike degenerates in < 65 fs into a thermal spike some 5.5 nm in diameter [115]. Annealing is a lengthy process, but by 20 ps, as the simulations show, the lattice thermal spike cools to give a stable, glassy structure some 4.6 nm across. According to more recent MD simulations [116, 117], the spatio-temporal evolution of ion tracks in other insulators, such as silica and quartz, proceeds similarly.

Even for insulators, a quantitative model based on the Coulomb explosion mechanism has yet to be developed. The predictive power of this mechanism for insulators is hampered by the lack of a quantitative description of the efficiency and lifetime of the electron trapping determining the lifetime of the Coulomb explosion. That is why no track radii have been determined from this mechanism.

The generation of a shock wave in the track of an SHI is also represented in another way: the formation of the shock wave as a result of a thermal spike [118]. The instantaneous heating of a local region of matter generates a pressure jump that initiates particle motion in that volume. If the velocity of this motion exceeds the speed of sound, a shock wave is created in the target. An important drawback of this model is the use of the classical theory of heat conductivity based on the Fourier law for heat flux. Nonequilibrium thermodynamics has to be applied with care when the characteristic length of the objects or space–time inhomogeneities approach the mean free path of heat carriers [19, 119]. It is well known that the Fourier law has a weak point, because it allows infinitely large velocities of heat dissipation, contradicting the fact that phonons cannot exceed the velocity of sound. There have been some attempts in track calculations to modify the Fourier law to limit heat dissipation velocities [119] or to take the thermal flux relaxation into account [120]. The Boltzmann transport equations have to be solved to better assess the applicability of the Fourier law. With the help of the thermodynamic fluctuation theory in [109, 121], numerical estimates have been made of defect formation, phase transformation, creep, diffusion, etc., in various materials, caused by thermoelastic stresses and thermoelastic waves that develop coincidentally with thermal spikes [23]. The acoustic pulses generated by particles stimulate crystal lattice transformations and can manifest themselves far from the ion path (long-range effects) [23].

An approach based on the rupture of atomic bonds in solids caused by intense electronic excitations has been proposed by Tombrello et al. ([110] and [194–197], cited in Ref. [1]). It enables calculating the latent track radius as a function of the ion energy E, the inelastic energy loss $(\mathrm{d}E/\mathrm{d}x)_e$, and the density of the material ρ in dielectrics, including organic materials [1]. However, an empirical tuning of two parameters e_c^* and γ (where e_c^* is the critical released energy density in the track core when the rupture of atomic bonds takes place and γ is an adjustable parameter, $0 < \gamma < 1$)

is needed if we want all the experimental data to agree with the calculated values with an accuracy of at least 10% [1]. With $e_c^* = 24$ eV nm$^{-3} = 0.4$ eV/atom, good agreement between the measured and calculated track radii can be achieved for a variety of materials, including quartz [1, 110]. In the case of quartz with the energy gap of 10 eV, the value 0.4 eV/atom, which corresponds to the excitation of about 4% of the atoms, is sufficient to destabilize the crystal lattice. A quantum mechanical treatment was used in [111] to describe the 'athermal melting' mechanism, yielding an estimate of this parameter that is somewhat higher than that predicted in [122].

In the framework of the inelastic (electronic) thermal spike (i-TS) concept, the electron and lattice subsystems are included as two coupled systems [123]. The kinetic energy of SHIs is deposited into the electron subsystem of the target, where thermalization occurs within about 10^{-15} s. The hot electrons then transfer their energy by electron–phonon coupling (equivalent to electron–atom collisions) to the cold lattice, in which thermal equilibrium is reached after about 10^{-13} s. The process of formation and development of an energy track is described in terms of the two-temperature model. The electron temperature T_e and the lattice temperature T_i are introduced, and then a system of two nonlinear heat conduction equations is solved, which in cylindrical coordinates take the form

$$C_e(T_e)\,\frac{\partial T_e}{\partial t} = \frac{1}{r}\,\frac{\partial}{\partial r}\left(rK_e(T_e)\,\frac{\partial T_e}{\partial r}\right) - g(T_e - T_i) + A(r,t)\,, \tag{3.1.1}$$

$$C_i(T_i)\,\frac{\partial T_i}{\partial t} = \frac{1}{r}\,\frac{\partial}{\partial r}\left(rK_i(T_i)\,\frac{\partial T_i}{\partial r}\right) + g(T_e - T_i)\,, \tag{3.1.2}$$

where $C_{e,i}$ and $K_{e,i}$ are respectively the specific heat capacity and the heat conductivity; the subscript k corresponds to e for the electron subsystem and to i for the ion (lattice) subsystem; g is the electron–phonon coupling constant, $A(r,t)$ is the density of the energy imparted by an incident ion to the electron subsystem of the solid, r is the radial coordinate, and t is the time variable. The heat diffusion in the electron and lattice subsystems is described by the classical heat conduction equations, with the electron energy loss being the heat source term. The energy exchange term is given by the product $g(T_e - T_i)$, where $T_e - T_i$ is the temperature difference between the two systems.

The energy density $A(r,t)$ denotes the spatio-temporal energy deposition of an ion to the electron subsystem and, in accordance with the theory of δ-electron formation accompanying the passage of swift ions [27], it can be written as

$$A(r,t) = bS_e \exp\left(-\frac{(t-t_0)^2}{2s^2}\right) F(r)\,,$$
$$F(r) = \frac{1}{2\pi r\lambda_w(E)} \exp\left(-\frac{r}{\lambda_w(E)}\right). \tag{3.2}$$

Here, the half-width s of the Gaussian distribution corresponds to the time the electrons need to reach thermal equilibrium, $t_0 \approx 10^{-15}$ s [124, 125] (the choice of t_0 has only a small effect on the radius of the melt area [1, 65]); $S_e = (1/N)(dE/dx)_e$, where N is the number of atoms per unit volume of the stopping medium; b is the normalization constant that ensures that the integration of $A(r,t)$ in space and time yields the electron energy loss S_e [see Eqn (3.6) in Ref. [1]); and λ_w is a parameter determined by fitting $F(r)$ to the actual expression [27], which therefore strongly depends on the incident ion energy E.

For example, about 70% of the energy deposited to the electron subsystem of silicon is confined to a domain 0.2 nm in diameter for a C_{60} ionic cluster with the energy 0.025 MeV a.m.u.$^{-1}$ and in domains 5 nm and 12 nm in radius for Pb^{208} ions with the respective energies 3 and 20 MeV a.m.u.$^{-1}$.

The electron–phonon coupling constant for metals has been presented in Refs [126, 127]. This parameter is linked to the electron mean free path λ as $g = K_e/\lambda^2$. Because the coefficients C_e, C_i, K_e, and K_i are temperature dependent, coupled differential equations (3.1.1) and (3.1.2) are nonlinear and can be solved numerically. A procedure to calculate these parameters in insulators and semiconductors is discussed in Ref. [1]. Using the numerical analysis of Eqns (3.1.1) and (3.1.2), the electron and lattice temperatures $T_{e,i}(r,t)$ can be calculated at any time t and radius r. Taking the latent heat of fusion into account (when the lattice temperature reaches the melting point), the radii of molten cylinders caused by swift ions have been calculated for a wide variety of materials (see [1, 118, 125] and the references therein). In many cases, this model has successfully predicted track radii and sputtering rates [125, 128–133]. The i-TS model assumes that the latent track results from the very rapid quenching of a molten region created along the ion path. We note that such a process can occur if the cooling rate is fast enough to avoid complete epitaxial recrystallization. For many insulators, the damage caused by SHIs typically amounts to latent tracks of amorphous or lower-atomic-density materials, which are micrometers in length and nanometers wide. In this model, the only free parameter for fitting the track size is the electron–phonon mean free path λ. The i-TS model correctly reproduced the observed influence of the ion velocity on the track radii for many amorphizable oxides [125] and for some nitrides [134].

Oxide materials that can exist in an amorphous state, such as SiO_2 (with the band gap $E_g = 12$ eV), $Y_3Al_5O_{12}$ ($E_g = 6.3$ eV), $Gd_3Ga_5O_{12}$ ($E_g = 4.8$ eV), $LiNbO_3$ ($E_g = 4.8$ eV), $Y_3Fe_5O_{12}$ ($E_g = 3$ eV), $BaFe_{12}O_{19}$ ($E_g = 1$ eV), and $YBa_2Cu_3O_{6.9}$ ($E_g \approx 0$), exhibit an interesting empirical dependence of λ on E_g (Fig. 2). The figure shows λ values obtained in thermal spike calculations based on the melting criterion by fitting the evolution of experimental radii with $(dE/dx)_e$ for various oxides. The extracted values are related to the inverse band gap energy E_g.

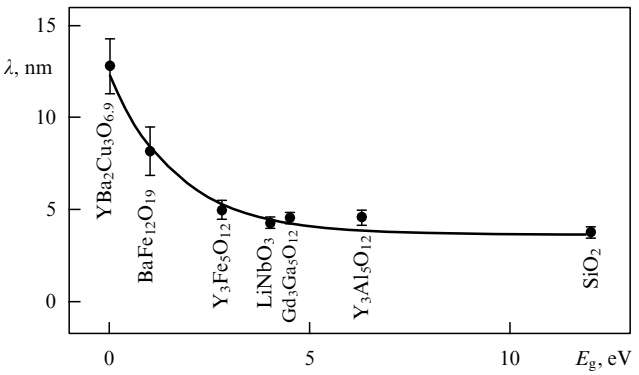

Figure 2. Electron mean free path λ from thermal spike fitting as a function of the band gap energy for several crystalline oxide materials [125].

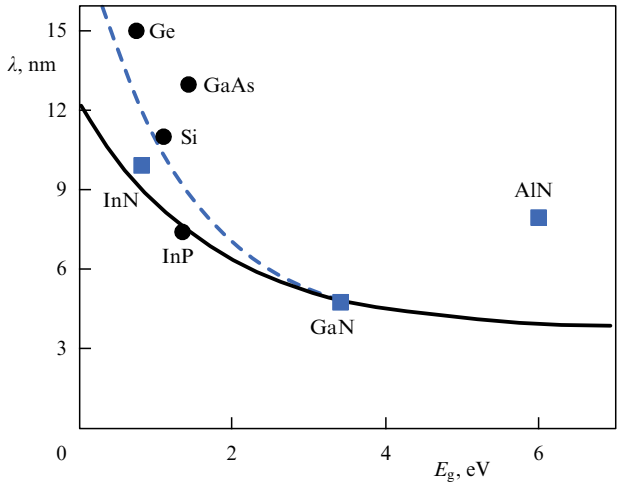

Figure 3. Evolution of λ versus the band gap energy using the melting phase as the criterion for track formation. The solid black line represents the empirical relation established for oxides (λ_{ref}) [128]. The blue squares are the λ values extracted from experiments [134] for InN, GaN, and AlN, and the black dots are the λ values extracted from the track size measured in InP, GaAs, Si, and Ge [134]. The blue dotted line is a fit of the data for semiconductors, excluding AlN.

However, this is not generally the case for the semiconductors presented in Fig. 3. As was indicated in Refs [1, 134], thermally stimulated solid-phase epitaxial growth (SPEC) can occur in several cases (AlN, GaAs, InP, Si, Ge), and this can lead to the radius of the amorphous track being smaller than the radius of the molten region, or even to track formation being inhibited. It is also assumed that the electron–phonon coupling constant does not reduce to a functional dependence on a single parameter, E_g, in general [134].

The response of nonamorphizable solids to SHIs is not just an amorphous cylindrical track; it exhibits manifold effects [1, 125]. In ionic crystals such as alkali and earth alkali halides, point defects and defect clusters are created [1]. Tracks in SnO_2 and CaF_2 are not described by thermal spike calculations using the melting criterion [125].

The principal criticism of the i-TS model involves several main issues [19, 65, 113]. First of all, large gradients in T_i at extremely short distances, comparable to the mean free path between phonon–phonon collisions, and the strong space and time limitation (nanometric volume and very short time) raise serious questions about the applicability of classical heat diffusion [19, 65, 113]. As discussed above, the deficiency of this model in allowing infinitely large velocities of heat dissipation requires some corrections or a more sophisticated description of the nonequilibrium processes.

In the i-TS model, the melting point T_m is a key parameter. Klaumünzer [65, 113] criticized this approach and claimed that superheating, supercooling, and the limited mobility of the melt–solid interface are completely ignored. In the case of semiconductor targets, this problem was discussed in Ref. [134]. Indeed, nucleation of a new phase requires some time, leading to superheating [135]. A similar problem appears upon cooling the molten track below T_m when recrystallization (solidification) starts at the melt–crystal interface, which causes the measurable track size to diminish [65]. This behavior of the kinetics of the crystalline order decay and the subsequent recrystallization (solidification) must be taken into account in calculating the track radius.

Second, all the processes in SHI tracks are significantly prolonged due to the energy storage in holes via secondary electron creation by the first generation of excited electrons in dielectrics and semiconductors (see Section 2.2.2). As noted in [98], this secondary electron creation plays a very important role as storage for and later source of energy, and can be described by an additional term related to holes in the heat diffusion equation. Electrons and holes are not distinguished in the thermal spike model. Spatial and temporal characteristics of energy deposition events and electron–hole distributions studied using Monte Carlo simulations [35, 98, 136] clearly show that $A(r,t)$ in Eqn (3.2) cannot be represented as a product of a temporal function (like an exponential or a Gaussian one) with a time-independent function $F(r)$. This means that the evolution of the track is a spatio-temporal event with no possibility of separating the spatial distribution from the time evolution [35, 98]. Moreover, the assumption that $C_i = 1$ J cm^{-3} K^{-1} and $K_i = 2$ W cm^{-1} K^{-1} for all insulators, constant in space and time, which was used in the i-TS track calculations in [132, 133], is also an oversimplification. Of course, there are doubts regarding the use of the i-TS model at short times ($t \leqslant 100$ fs), when the cascading electrons are still energetic and the electron–phonon coupling is weak.

Thus, the calculations of electron temperatures in the i-TS model may noticeably underestimate the experimental values obtained by Auger-electron spectrometry (see Fig. 11 in Ref. [137]).

In our opinion, the i-TS model gives quantitative information without using complex atomistic simulation codes when the removal of energy of electron excitations from the track is hampered. In materials with poor thermal conductivity or in fine-grained materials, the contribution of the thermal mechanism to the phase transformation and to the generation of structural defects becomes decisive.

Experimental studies [106, 138, 139] and MD simulations [140] demonstrated that nanoparticles of metals deposited on a target surface are desorbed when they are irradiated with SHIs or energetic C_{60} ions and thereby heated to their melting point. By using this desorption mechanism, a method to estimate the local temperature during track formation was proposed in Ref. [106].

Strictly speaking, the thermal spike models, as well as the other models discussed above, do not provide atomic-scale details of the internal structure of the latent tracks observed by high-resolution TEM, AFM, or other methods. They do not consider phase transitions (other than melting, vaporization, and sputtering), disordering, defect annealing, or recrystallization, including SPEC. Fortunately, MD simulations can provide atomic-scale details and are used to simulate track formation in a number of materials [116, 117, 141–143].

4. Extending the track formation models for band-gap materials

4.1 Extending the track formation models for semiconductors

The thermal spike model was originally developed for metals, and it has been used extensively in this area. Later, this model was applied to semiconducting and insulating materials [108,

144, 145], following the argument that the excited electrons have properties similar to those of the conduction electrons in metals. This is a rough approximation, because the number of conduction electrons varies in space and time in band-gap materials, but is constant in metals.

Recently, Daraszewicz and Duffy [146] extended the thermal spike model [Eqns (3.1.1) and (3.1.2)] by including an additional conservation equation for the carrier density

$$\frac{\partial N^*}{\partial t} + \nabla J = G_e - R_e\,, \tag{4.1.1}$$

where N^* is the concentration of electron–hole pairs, G_e and R_e are the respective source and sink terms, and J is the carrier current density, which is related to the concentration, the electron temperature T_e, and the band gap E_g as

$$J = -D(T_l)\left(\nabla N^* + \frac{2N^*}{k_B T}\nabla E_g + \frac{N^*}{2T_e}\nabla T_e\right). \tag{4.1.2}$$

Here, the current prefactor $D(T_l)$ is the ambipolar diffusion coefficient. The local charge neutrality condition is imposed in this model. Therefore, the local concentration of electrons and holes is equal everywhere. In general, the gradient of the band gap should be included because the band-gap varies with the lattice temperature in some materials. The total carrier energy density U is a combination of E_g and T_e: $U = N^* E_g + 3N^* k_B T_e$. This leads to the carrier specific heat capacity $C_{eh} = 3N^* k_B + N^*(\partial E_g/\partial T_e)$. In the framework of this model, the electron energy balance equation takes the form

$$\frac{\partial U}{\partial t} + \nabla W = U_S - U_I\,, \tag{4.1.3}$$

where U_S and U_I are source and sink terms and

$$W = (E_g + 2k_B T_e)J + (k_e + k_h)\nabla T_e \tag{4.1.4}$$

is the ambipolar energy current density. Here, k_e and k_h are the electron and hole thermal conductivities. In semiconductors and insulators, N^* is space and time dependent; therefore, the electron temperature diffusion of the two-temperature model [Eqn (3.1.1)] must be replaced with Eqns (4.1.3) and (4.1.4). Moreover, the electron–phonon coupling term $g(T_e - T_i)$ in Eqn (3.1.1) is replaced with

$$U_I = C_e\,\frac{T_e - T_i}{\tau_e}\,, \tag{4.1.5}$$

where τ_e is the electron–lattice relaxation time and the electron heat capacity C_e is proportional to N^* ($C_e = 3N^* k_B$).

This extended treatment [146] enables us to include processes such as Auger recombination and impact ionization in the model, in addition to energy exchange between the lattice and the carriers. The temporal and spatial evolution of the carrier density, the electron, and lattice temperatures, and the track radii were calculated in Ref. [146] for a range of electron stopping powers (from 10 to 80 keV nm^{-1}) in silicon. The parameters used in this model for silicon samples are summarized in Table 2. The results of track radius estimations are presented in Fig. 4 with experimental points included [147, 148]. They demonstrate that the lattice and electron temperatures come to thermal equilibrium in about 20 ps. At times later than ~ 3 ps, the lattice temperature falls below the melting temperature and therefore resolidification occurs. It is obvious that none of the lines fully reproduces the experimental data, with $\tau_{e-ph} = 0.4$ ps ($\tau_{e-ph} = C_e/g$) providing the closest fit. A possible source of this discrepancy includes the simplification introduced to the model (such as a constant (zero) electron temperature gradient, the band gap with a constant value, the 'velocity effect', electron–hole recombination, and impact ionization processes being ignored).

Table 2. Model parameters for Si.

Quantity	Symbol	Value
Carrier ambipolar diffusivity	D_0	$18(300\ \mathrm{K}/T)\ \mathrm{cm^2\ s^{-1}}$
Band gap	E_g	1.16 eV
Melting point	T_m	1683 K
Vaporization temperature	T_v	2953 K
Solid density at $T = 300$ K	ρ_s	2.32 g cm^{-3}
Liquid density at T_m	ρ_l	2.50 g cm^{-3}
Latent heat for fusion at T_m	H_f	1797 J g^{-1}
Latent heat for vaporization at T_v	H_v	13.722 J g^{-1}
Lattice specific heat	C_a, J g^{-1} K^{-1}	$C_a = -0.1354 + 4.486\times10^{-3}T - 5.207\times10^{-6}T^2$ (60 K $\leqslant T <$ 300 K), $C_a = 0.7007 + 1.469\times10^{-4}T + 3.183\times10^{-8}T^2$ (300 K $\leqslant T \leqslant T_m$), $C_a = 1.045$ ($T > T_m$)
Lattice thermal conductivity	K_a, W cm^{-1} K^{-1}	$K_a = 1042\times T^{1.158}$ (60 K $\leqslant T \leqslant T_m$), $K_a = 0.14$ ($T_m \leqslant T \leqslant T_v$), $K_a = 8.76\times10^{-5}T^{1/2}$ ($T > T_v$)

More recently, Daraszewicz and Duffy [149] developed their extended thermal spike model for band-gap materials

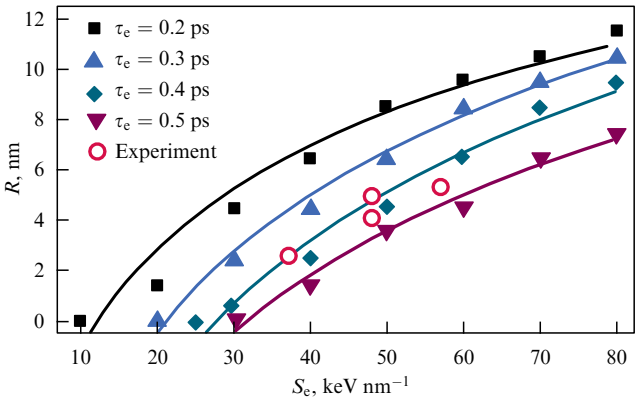

Figure 4. Calculated track radius (molten phase) versus the electron stopping power for $\tau_e = 0.2$, 0.3, 0.4, and 0.5 ps [146]. The experimental values of amorphous track radii [147, 148] are included as circles. The value 0.4 ps for the electron–phonon relaxation time τ_e, the only free parameter in the model, gives a reasonable fit to the limited experimental data.

into a hybrid continuum-atomistic model, which allows accessing the atomistic behavior via trajectories of the track region atoms. Continuum-only models [150] disregard a few important processes in the target, such as generating elastic or shock waves, lattice straining, and volume change by a phase transition.

The transport of momentum and mass is included in the modified continuum-only model [150] and in molecular dynamics (MD). An integrated model for band-gap materials was recently applied in laser irradiation studies [151, 152]. In Ref. [149], the coupling of the extended thermal spike model [146] to MD was performed by replacing the equation for the lattice temperature in Ref. [146] with modified MD equations of motions, according to Refs [153–155]:

$$m\,\frac{\partial \mathbf{v}_i}{\partial t} = \mathbf{F}_i(t) - \gamma_i \mathbf{v}_i + \tilde{\mathbf{F}}_i(t)\,, \qquad (4.1.6)$$

where i runs over all atoms and $\mathbf{F}_i$ is the Newtonian force acting on an atom, while $\tilde{\mathbf{F}}_i$ and $\gamma_i \mathbf{v}_i$ are additional driving and friction forces, based on the Langenvin thermostat formulation that takes the electron–phonon coupling into account. The energy gain represented by a stochastic force $\tilde{\mathbf{F}}_i(t)$ has a random magnitude and orientation, $\tilde{\mathbf{F}}_i(t) = \sqrt{\Gamma}\tilde{\mathbf{A}}_i(t)$, where $\Gamma = 2\gamma_i m_i k_B T_e$, with γ_i being the friction term.

Using the hybrid continuum–atomistic model [149], simulations were performed for various electron–phonon relaxation times ($\tau_{e-ph} = 0.05-0.15$ ps) for stopping powers in the range 10–70 keV nm^{-1}. A reasonable agreement with limited experimental data (carbon cluster ions) [156] was achieved for $\tau_{e-ph} = 0.05$ ps. This model takes temporal and spatial evolutions of the atom temperature, carrier density, and energy into account, but does so using one fitting parameter, the electron–phonon relaxation time τ_{e-ph}.

In [136], silicon samples were exposed to an Xe ion beam irradiation with two kinetic energies, 0.625 MeV a.m.u.$^{-1}$ and 0.916 MeV a.m.u.$^{-1}$. This corresponds to a maximum stopping power of 12.1 keV nm^{-1}. Irradiation under $\theta = 90°$, as well as under glancing incidence angles $\theta = 1.5°-2°$ with respect to the surface, did not produce any tracks. To identify the damage threshold for silicon crystals, the authors performed various calculations in the framework of the standard and modified thermal spike models. According to the first model, the melting (damage) threshold is found to be around $S_{e,th} = 8$ keV nm^{-1}. In their opinion, the discrepancy between the experimental and theoretical observations can be explained by the fact that the modification induced by the melting of the target material anneals during the cooling stage. This recrystallization process would not be possible if the material were actually vaporized. That is why the same calculations were repeated under the assumption that the modified target material had to reach the vaporization temperature $T_{vap} = 3107$ K. Using the criterion of vaporization, the damage threshold in c-Si is found to be $S_{e,th} = 25$ keV nm^{-1}. However, this threshold is still significantly smaller than the experimentally determined values for bulk c-Si.

Because the electron–phonon coupling constant is a crucial parameter, a series of calculations was performed in [136] with this coupling constant varied in a physically reasonable range from 5×10^{17} to 1×10^{19} J s^{-1} m^{-3} K^{-1}, and the melting criterion was applied. The decrease in g from 5×10^{18} to 5×10^{17} J s^{-1} m^{-3} K^{-1} leads to an increase in the damage threshold from 8 to 21 keV nm^{-1}. A change in g within one order of magnitude leads to roughly the same change in the calculated track formation threshold that was determined when changing the criterion required for material modification. Furthermore, it was shown that highly energetic excited electrons, δ-electrons, transport their energy away from the SHI trajectory, rather than confining the energy locally, as was assumed in many theoretical papers. Next, a series of calculations was performed with only a certain percentage of the stopping power S_e used in Eqns (3.1.1) and (3.1.2). The calculations were performed using the electron–phonon coupling constant $g = 5 \times 10^{18}$ J s^{-1} m^{-3} K^{-1} and the melting criterion. The corresponding damage threshold is shown in Fig. 5. Reducing the effective energy loss from 100% to 20% increases the track formation threshold from 8 keV nm^{-1} to 42 keV nm^{-1}, making this change the most effective parameter studied in [136]. An approach that deals with these nonequilibrium electrons has been treated in detail in Refs [157, 158]. Within this approach, the dynamics of excited electrons was studied using the Monte Carlo method.

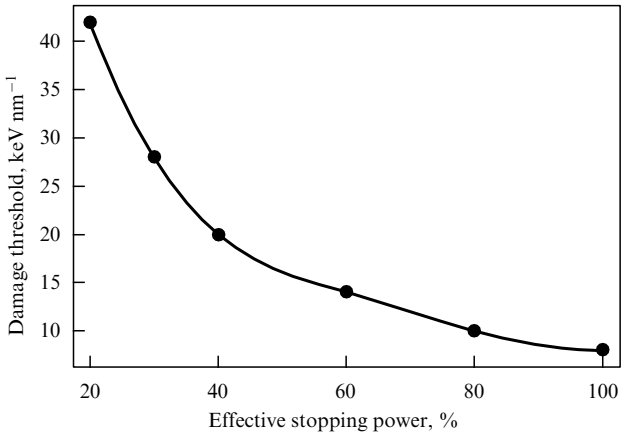

Figure 5. Damage threshold vs. the effective stopping power [136].

The CDF theory was used in [22, 35] for systematic calculations of the inelastic and elastic processes in silicon for incident ion energies in the range 0.5–100 MeV a.m.u.$^{-1}$. This information then served as a database for Monte Carlo simulations of spatial and temporal characteristics of energy deposition, electron–hole distributions, and track-structure effects in silicon devices (single-event effects). Ion track radii as a function of the incident ion energy were calculated. According to their estimates, melting in the track region can happen for Au and heavier ions with energies 0.5–2 MeV a.m.u.$^{-1}$ [35]. To predict this phase transition, the authors calculated the average energy E_{ta} deposited by an ion per target atom within a track-core cylinder (65% energy deposition) as $E_{ta} = 2\pi N^{-1} \int_0^{r_c} rD(r)\,dr/\pi r_c^2$, where $N_{Si} = 5 \times 10^{22}$ cm^{-3} is the atomic density of silicon. Then E_{ta} was compared with the energy per atom, $E = 0.88$ eV, needed to start the melting of this volume in the framework of the i-TS model [145]. It was assumed that E_{ta} is fully converted to the Si atom heating through the electron–phonon interaction, which is only a crude approximation. At least, the high lattice heat conductivity in silicon should be taken into consideration in these estimations (see Section 2.2.2).

The specific energy losses $(dE/dx)_e$ for any elemental ions in silicon do not exceed 28 keV nm^{-1}. However, experiments [147, 148] on irradiation of crystalline silicon by fullerene ions C_{60}^{2+} with $E = 30$ MeV and $(dE/dx)_e = 48$ keV nm^{-1} and with $E = 40$ MeV and $(dE/dx)_e = 57$ keV nm^{-1} revealed the

formation of tracks with the respective entrance diameters 8.4 and 10.5 nm. The track diameters remain constant to a depth of roughly 80–100 nm [147], and at larger depths gradually decrease. Very often, the tracks end in a series of droplets of defective material along the ion paths (the discontinuous section of the tracks). The threshold values of the energy losses $(\mathrm{d}E/\mathrm{d}x)_\mathrm{e}$ for track formation in Si by fullerenes are roughly 30 keV nm^{-1}.

When semiconductors are irradiated by fullerene ions, the density of the energy released near the ion paths (over the correlation length) is very high, because the maximum paths r_max of the δ-electrons amount to only 1.9 and 2.9 nm for C_{60} with $E = 30$ and 40 MeV, respectively, while for an ion of ^{238}U with $E = 1$ GeV, $r_\mathrm{max} = 1050$ nm. Hence, the entire released energy is localized near the path of the fullerene ion. This is an important factor in the description of track formation in semiconductors irradiated by ion clusters.

The results published to date show that the formation of visible tracks in crystalline semiconductors, as in metals and insulators, requires a threshold value of the electron energy deposition characteristic of the corresponding material, which obviously cannot be reached with individual ions in Si. It should be mentioned that the data available presently do not show any clear correlation between track formation and the macroscopic physical properties of the semiconductors, e.g., the band gap, melting temperature, and electrical properties.

Evidence of track formation in Ge single crystals irradiated by 710 MeV Bi and 1.3 GeV U ions, respectively corresponding to energy deposition of 37 and 42 keV nm^{-1}, was found by Komarov et al. [159]. Single dot-like defects as well as discontinuous tracks have been registered along the ion trajectories. The density of the discontinuous tracks is about two orders of magnitude lower than the ion fluence, which is similar to the behavior found for Xe irradiation in InP [160, 161]. The periodic appearance of dot-like defects within discontinuous tracks is explained by fluctuations of the ion charge state along the ion trajectories, which periodically reduces the electron energy deposition below the threshold value for track formation [1, 162, 163]. The distance between the defects can be explained by a periodic simultaneous loss of three electrons, increasing the energy deposition by about 4–6 keV nm^{-1}. From this, it was concluded in [159] that the formation of continuous tracks in Ge crystals requires the electron energy loss not less than 46–49 keV nm^{-1}. The discontinuity of the tracks and the fact that not each impinging ion forms a track indicate that the electron energy deposition value in this case is only slightly above the threshold value for the formation of registered damage.

Proof of discontinuous track formation in group IV of binary semiconductors was presented in [164, 165]. As discussed in Section 2.2.2, the lattice heat conductivity in silicon, germanium, and diamond is comparable to or higher than the heat conductivity of metals. Therefore, a high efficiency of energy removal from the track core can hamper latent track formation.

Amorphous tracks were also found in C_{60}-irradiated Ge and GaAs in [156, 166]. The diameter of the tracks increases with the energy of the clusters. The threshold values for the electron energy loss $(\mathrm{d}E/\mathrm{d}x)_\mathrm{e} = 36$ keV nm^{-1} for GaAs, $(\mathrm{d}E/\mathrm{d}x)_\mathrm{e} = 33$ keV nm^{-1} for Ge, and $(\mathrm{d}E/\mathrm{d}x)_\mathrm{e} = 28$ keV nm^{-1} for Si were determined from high-resolution TEM images. However, we note that not each impinging cluster ion directly forms a visible track in GaAs; instead, the material first has to be predamaged [166]. On the contrary, irradiation of Ge with monoatomic swift Bi and U ions, yielding significantly higher values of $(\mathrm{d}E/\mathrm{d}x)_\mathrm{e,\,thr}$ ($\geqslant 37$ keV nm^{-1}), generates only discontinuous tracks [159]. As was mentioned above, these results illustrate the importance of the radial distribution of the released energy near the path of the ion.

Track formation processes in (100) GaAs crystals irradiated with swift Bi (710 MeV) and U (1.3 GeV) ions to fluences in the range $5 \times 10^{10} - 1 \times 10^{12}$ cm^{-2} have been investigated by means of selective chemical etching (SCE), atomic force microscopy (AFM), and computer simulation (CS). Ion tracks in GaAs samples irradiated with U and Bi ions to the fluence of 5×10^{10} cm^{-2} were registered by means of AFM and SCE. The density of tracks obtained from AFM data coincides well with the irradiation fluence. A fluence increase to 1×10^{12} cm^{-2} (overlapping of tracks) leads to the annealing of tracks formed in GaAs at the early stages of irradiation [167].

For the computer simulation of track formation processes in semiconductors, the modified thermal spike model has been developed by our team [167, 168]. The temperature dependences of model parameters, such as the specific heat, thermal conductivity, and electron–phonon coupling coefficient, were obtained or taken from Refs [169, 170]. A system of heat flow equations [Eqns (3.1.1) and (3.1.2)] was used to describe local temperature fields along the ion trajectory. The latent heat of melting was taken into account. The electron–phonon coupling constant g is usually treated in the i-TS model as a free parameter or expressed in terms of other model parameters (λ). To determine g, all possible types of electron–phonon interactions in different semiconductors in a broad range of electron and lattice temperatures were considered in our paper [167]. Generally speaking, in the case of A^3B^5 semiconductors, it is necessary to take into account the deformation interaction with acoustic phonons (DA), the deformation interaction with optical phonons (DO), the piezoelectric interaction with acoustic phonons, and the polar interaction with optical phonons [171]. The results of these calculations [167] show that for all possible electron and lattice temperatures in the track region, only DA and DO interactions contribute to the g parameter in GaAs and InP crystals.

However, for time intervals less than at least one period of lattice vibrations ($\sim 10^{-13}$ s) after the passage of an ion, the electron plasma interacts with practically immobile individual ions, rather than with collective ion oscillations. That is why the model of electron–ion energy exchange proposed in Ref. [172] was used for such short times [167]. In the framework of this model, the rate of electron–ion energy exchange can be written as

$$g = \frac{4LZn_\mathrm{e}e^4m_\mathrm{e}^2}{\pi M\hbar^3\left[1+\exp\left(-\mu/T_\mathrm{e}\right)\right]}\left[\frac{T_\mathrm{i}}{1+\exp\left(\mu/T_\mathrm{e}\right)} - T_\mathrm{e}\right], \quad (4.1.7)$$

where M and Z are the ion mass and ion effective ionization factors in the lattice, e and m_e are the electron charge and mass, n_e is the concentration of electrons excited from bonding states in the valence band to anti-bonding states in the conduction band, L is the Landau integral, and μ is the chemical potential. The procedure for obtaining n_e, based on the quantum dielectric formalism, was described in Ref. [173].

The electron–ion heat transfer calculated by Eqn (4.1.7) at high electron temperatures existing in the first moments after

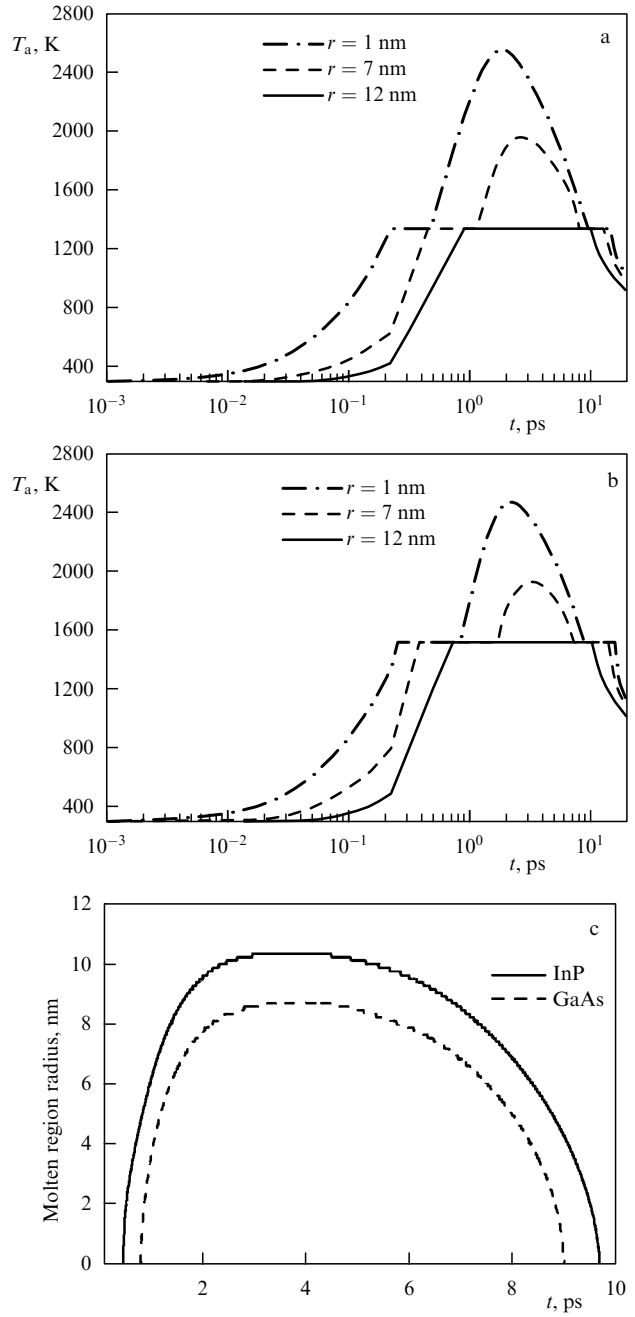

Figure 6. Calculated evolution of the atomic temperature at different distances from the trajectory of a 710 MeV Bi ion in (a) InP and (b) GaAs crystals and (c) calculated radii of molten regions.

the ion passes, is at least one order of magnitude less than that obtained using the electron–phonon interaction approach. No melting of the track core in silicon crystals irradiated by any elemental SHIs is predicted in the framework of this model [173].

Figure 6 shows the results of calculations of temperature fields along the ion trajectory taking the electron–ion interaction into account in form (4.1.7) at times shorter than 10^{-13} s and the DO and DA interactions thereafter. The maximum radius of the molten region formed during 710 MeV Bi ion irradiation amounts to 10.3 nm for InP crystals and 8.7 nm for GaAs crystals. The respective molten region lifetime is 9.2 ps and 8.2 ps for InP and GaAs. The calculated lifetimes of molten regions allow us to speak about the presence of the liquid phase and its subsequent solidification in both semiconductors. However, amorphous track cores cannot be formed if epitaxial recrystallization of the melt occurs during the cooling process. Therefore, the velocity of the solidification front must be calculated. It is about 2000 m s^{-1}, which is two orders of magnitude higher than the velocity of epitaxial crystallization of the discussed semiconductors. These results indicate that there is no crystallization of this region even in the surrounding perfect crystalline matrix. Therefore, according to the performed calculations, an amorphous track should be formed after an individual ion passes in both InP and GaAs crystals.

As mentioned above, the calculated diameters of molten regions near the surface of InP and GaAs crystals irradiated with 710 MeV Bi ions are respectively 20.6 nm and 17.4 nm. A reasonable agreement between calculated [167] and measured track radii is obtained for GaAs [167] and InP [160].

4.2 Extending the track formation models for insulators

Possible mechanisms of track formation in insulators are still under discussion.

In [174, 175], the thermal spike mechanism was used to construct a simple empirical model for calculating the track radii in amorphizable insulators (oxides). In the analytic thermal spike model [174, 175] (also see the references therein), the ion-induced temperature increase $\Delta T(r, t)$, when it has a maximum value, is given by the formula

$$\Delta T(r, 0) = \frac{g\langle S_e\rangle}{3\pi k_B a^2(0)} \exp\left[-\frac{r^2}{a^2(0)}\right], \qquad (4.2.1)$$

where $\langle S_e\rangle = S_e/N$ is the atomic stopping power, N is the number density of atoms, the initial width is $a(0) = 4.5$ nm for all insulators, and $\varepsilon = gS_e$ is the thermal energy of the spike. The efficiency factor g equals 0.4 or 0.17 in the respective energy ranges $E < 2$ MeV a.m.u.$^{-1}$ and $E > 8$ MeV a.m.u.$^{-1}$. These values of g were found by a comparison with the existing experimental data. For $S_e = \text{const}$, these values lead to higher peak temperatures and a larger diameter of tracks for the ion energies less than 2 MeV a.m.u.$^{-1}$.

Assuming the simple Gaussian function

$$\theta(r) = T_{PL,H} \exp\left(-\frac{r^2}{w^2}\right) \qquad (4.2.2)$$

to describe variation of the experimental track radii R_e (which are quoted in Ref. [175]) with the melting temperature T_m in insulators, Szenes [175] showed that the Gaussian width w is about 4.5 nm. Here, T_{PL} and T_{PH} are the respective peak temperatures for low and high energies. Track radii can be obtained from the equation $\theta(R_{tr}) = T_m - T_{irr}$ (where T_{irr} is the irradiation temperature); $\theta(r)$ does not depend on the experimental or material parameters. The calculated and experimental data were compared for sixteen insulators in [175].

The existence of a universal function $\theta(r)$ implies the same temperature distributions and corresponds to the relation $\theta(r) = \Delta T(r, 0)$ in a number of insulators when $\langle S_e\rangle = \text{const}$. Keeping in mind its simplicity, the Szenes model, dealing only with the lattice heat transport, is successful for this type of insulators with amorphous tracks. This model could come close to reality for amorphizable insulators with low lattice heat conductivity when the self-trapping of excitons is the prevailing and rapid mechan-

ism [65]. There is an obvious correlation of the $a(0)$ parameter (4.5 nm) with the track-core diameter r_c (4–5 nm), which was discussed in Section 2.1. The velocity effect is incorporated into the coefficient g, but the fate of the other part of the electron excitations remains unclear.

The function $\theta(r)$ does not exist for semiconductors and insulators such as Al_2O_3 and $MgAl_2O_4$ [175], and the discussed formalism can be used, in general, only for a certain number of insulating materials and a particular range of ion energies.

However, we must note a morphological difference between tracks (see Section 8.2 in Ref. [1]) in amorphizable and nonamorphizable materials and also the previously mentioned ambiguity in interpreting the results on track formation in nonamorphizable materials in the thermal spike model. For such materials, and especially alkali–halide crystals, the excitonic model is probably the most adequate one. A qualitative picture of this model was given in [176], while the quantitative aspects were discussed in [177].

The dynamics of structural modifications of insulators by SHIs were studied in Refs [92, 98] by using a combination of the Monte Carlo (MC) method and the thermal spike model [154]. The first method was used to describe SHI penetration and the subsequent excitation and relaxation of the electron subsystem and the second one for describing the heating of the lattice. It was shown in [98] that all processes in ion tracks are significantly prolonged due to energy storage in holes via secondary electron creation by the first generation of excited electrons. Such processes were described by an additional term in the heat diffusion equation related to the energy stored in the hole subsystem [98]. The delay caused by this energy storage leads to an electron–lattice equilibration time up to tens of picoseconds.

In the framework of this treatment, it was shown in [178] that due to the transient nature of the number of excited electrons in the conduction band, the electrical conductivity is also highly time dependent during the motion of SHIs in the insulator. As a model system, the irradiation of SiO_2 with high-energy Ca ions ($dE/dx = 2.7$ keV nm^{-1}) was chosen in the calculations. It was found that the enhancement of the transient electrical conductivity is comparable to that in metals like gold. Such a switching of the band structure from an insulating ionic to a metallic character (corresponding to the complete closure of the energy gap) was revealed in Ref. [77] for amorphous BeO targets irradiated with 3 MeV a.m.u.$^{-1}$ Ar^{7+} and 1.78 MeV a.m.u.$^{-1}$ Xe^{15+} ions. In this case, an ultrafast cold melting of the lattice [111, 179] can be treated as the dominant effect.

A combined model to simulate structural heterogeneities of swift heavy ion tracks in complex oxides (isometric $Gd_2Ti_2O_7$ pyrochlore and orthorhombic Ga_2TiO_5) was presented in Ref. [180]. The i-TS model was used to calculate the energy dissipation over time and space. Using the temporal and spatial energy profiles generated from this calculation, molecular dynamics simulations were performed to model the atomic-scale evolution of the tracks. According to those calculations, the simulated internal structure of the tracks consists of an amorphous core and a shell of disordered, but still periodic, domains. These results show that track formation is controlled by the coupling of several complex processes, involving different degrees of amorphization, disordering, and dynamic annealing [180]. During the time of cooling the system to room temperature, the track region could stay near the recrystallization temperature for a sufficiently long time (up to 50 ps) to allow a partial recrystallization of the amorphous track core into crystalline shells [180]. The differences in the details between simulations and experiments (track size and structure) are observed and discussed in Ref. [180]. We stress again that the early stage of track evolution is not described properly in the framework of the thermal-spike model.

We note that a mechanism of 3D nanosize ($\sim 10-20$ nm) defect formation in wide-gap ionic crystals ($E_g = 5-15$ eV) such as Gd_2SiO_5 and $Lu_3H_5O_{12}$ is discussed in detail in Ref. [181]. The formation of intrinsic 3D defects is observed: a relatively large group of host ions undergo a local phase transition under a high excitation density in the tracks of SHIs and remain stable even after annealing to a temperature of $0.7T_m$. According to the treatment in Ref. [181], the experimental data obtained in complex metal oxides under irradiation with SHIs can be regarded as possible manifestations of the collapse of solitons with the formation of intrinsic nano- and mesodefects. The damaged part of a crystal lattice at the end of the ion range (where nuclear stopping dominates) serves as a certain wall for a mobile discrete soliton formed in the track with the frequency above the acoustic phonon branch. Back reflection from this wall is followed by interference between the breathers moving in opposite directions. As a result, a set of lattice points with an increased amplitude and anharmonicity is generated [181].

The conditions for formation, localization, and collapse of discrete 3D solitons were theoretically considered previously (see Refs [182, 183] and the references therein). The discussed mechanism of such radiation damage has been described in [182–86]. The efficiency of the collapse of 3D solitons depends on several parameters, including the mass ratio of heavy and light ions in the irradiated material, and on the presence of an energy gap between the acoustic and optical branches in the phonon spectrum. In the discussed system, $GdSiO_5$, the mass of gadolinium (157) exceeds the masses of silicon and oxygen by a factor of 5.6 and 9.8. SHI irradiation of MgO single crystals with fluences up to 3×10^{13} ions cm^{-2} does not generate any nano- or mesodefects [181]. The mass ratio of elements in MgO is close to unity (0.67).

Recently, computational molecular dynamics simulation results on track formation in several insulating materials, including quartz, amorphous silica (α-SiO_2), zinc oxide, and diamond were reported in [116, 117]. In particular, MD methods were used to model mass transport leading to density variations in the track volume during the track formation stages. As in Ref. [180], this MD simulation incorporates a time-dependent energy deposition based on the i-TS model. At early stages up to 4 ps after the ion passage, the rapidly heated material at the track core expands outwards as a pressure wave [116]. In Table 3, a list of density variations at 4 and 150 ps after the ion passage are presented for a few values of electron stopping. At an energy loss of 13 keV nm^{-1}, only amorphous silica showed a significant (over 5%) density drop in a cooled track. At an energy loss of 15 keV nm^{-1}, however, quartz also shows a 10% lower density core after cooling, and a similar 11% drop in density can also be seen in the tracks formed in diamond at 19 keV nm^{-1}. Of the discussed materials, amorphous silica illustrates the importance of the decrease in density most clearly, even at relatively low stopping powers. Such a low-density-core–high-density-shell fine structure was revealed experimentally in amorphous SiO_2 [187, 188]. In quartz, the

Table 3. Density differences at an early stage of track formation (4 ps) and after cooling (150 ps) compared to the initial density for different materials [116].

$(dE/dx)_e$	3 keV nm^{-1}	6 keV nm^{-1}	9 keV nm^{-1}	13 keV nm^{-1}	Other
α-SiO_2					
4 ps 150 ps	−2% −2%	−14% −4%	−27% −10%	−41% −16%	
Quartz					15 keV nm^{-1}
4 ps 150 ps	−2% 0	−2% −1%	−15% −2%	−23% −5%	−25% −10%
ZnO					27 keV nm^{-1}
4 ps 150 ps	−9% 0	−15% 0	−20% −1%	−21% −1%	−20% −1%
Diamond					19 keV nm^{-1}
4 ps 150 ps	−1% 0	−3% −2%	−4% −3%	−9% −5%	−14% −11%

molten region is almost completely frozen into an amorphous track, whereas in ZnO recrystallization occurs upon cooling, and therefore high stopping powers are needed to register a visible track [116]. The experiments in [189] show clear amorphous tracks in diamond-like carbon, but not in crystalline diamond even after irradiation with 1 GeV U ions.

The authors of Refs [116, 117] recognize that their simulations suffer from some limitations (concerning the use of the i-TS model), which will need to be addressed for a quantitative comparison, but these constraints do not impact the qualitative conclusions drawn here.

Very recently, a new and very informative approach was proposed and developed in a series of papers by Russian scientists [57, 58, 93, 99, 190] to provide an suitable description of energy transfer from excited electrons to the lattice in SHI tracks in insulators. The approach consists of three different approximations combined into one system. At the first stage, up to tens of femtoseconds after the projectile passage, the Monte Carlo model is used to simulate the initial excitation of electrons by an SHI and the further kinetics of fast electrons in ionization events. Next, at $t > 10$ fs, spatial spreading of electrons is treated in the framework of the molecular kinetic method. The energy and momentum exchange of excited electrons with the lattice is described, tracing the atomic trajectories with the MD method up to picoseconds after the SHI passage. The complex dielectric function formalism is used to calculate the cross sections of interactions of an ion and δ-electrons with the electron subsystem of a sample. It takes all collective modes of excitations (plasmons) in the electron subsystem into account.

Calculations performed for Al_2O_3 irradiated with 167 MeV Xe ions [99] and for LiF irradiated with 0.96 GeV Kr ions and 2 GeV Au ions [93] showed that the lattice heating by the delocalized electrons (~ 200 and ~ 100 K respectively) is not sufficient to create any structural transformations. It was demonstrated that including the excess energy of valence holes can initiate structure transformations with sizes similar to those detected in experimental studies [191, 192]. This means that the kinetics of the valence hole subsystem should be taken into consideration when modeling the SHI track formation in dielectrics. We note that only such cumbersome multi-scale simulations can simultaneously provide atomic-scale details of the track structure and the morphology in different types of materials.

5. Intermixing in layered structures

Intense electron excitations are the cause of ion–beam mixing in layered structures. Such an effect has been observed in many double-layer and multilayer systems: metal–metal, metal–semiconductor [193–198], metal–insulator [199, 200], ceramics–insulator [201, 202], and ceramics–semiconductor [202, 203].

Intermixing of bilayer metallic systems induced by SHIs has been clearly evidenced, and it was suggested that the energy transferred from the incident ion to the target electron subsystem could play a dominant role in the mixing process. However, the mechanism of the intermixing in metallic bilayer systems is still an open question. Based on numerical simulations of the lattice temperature with a three-dimensional code developed in the framework of the i-TS model, thermal-spike effects in intermixing at the interface of Ni/Ti bilayers irradiated by SHIs have been studied [204]. For these systems, the simulation results suggested that melting could be achieved at the Ni/Ti interface with GeV Ta or U ions, even though bulk Ni is insensitive to SHI irradiation when it is irradiated alone. The molten phase can last up to about 1 ps, which is sufficient for the occurrence of interdiffusion at the interface.

Under such assumptions, the intermixing at the interface of irradiated bilayers is attributed to interdiffusion in the molten ion tracks. The mean diffusion length after irradiation to a fluence Φ can be roughly estimated as

$$\lambda_d^2 = 2\pi R_m^2 \Phi D^* \tau_m ,$$

where D^* is the interdiffusion constant, R_m is the radius of the ion tracks at the interface, and τ_m is the molten stage duration. The deduced values of D^* are $\sim 1.4 \times 10^{-4}$ cm^2 s^{-1} (Ti in Ni) and $\sim 8.7 \times 10^{-4}$ cm^2 s^{-1} (Ni in Ti). These values are much larger than those known for solid-state diffusion, but are of the order of the liquid interdiffusion.

SHI-induced mixing in metal–semiconductor systems up to the complete intermixing occurs at the interface, and it increases with the fluence, electronic energy loss, and irradiation temperature [205–207]. It appears that most of the observed phenomena addressed here are not directly related to the primary energy deposition of the ions, but depend on the properties of thermal spikes after the energy transfer to the lattice, including the case of transient melt phase formation [207].

The thermal spikes created by SHIs can be the driving force behind the mixing of metal–ceramic material systems (Fe, Cu, Ni, Ti, Au, Ag)/(MgO, Al_2O_3, SiO_2, ZrO_2) and the increase in interphase adhesion, as in the case of thermal spikes created by atomic displacement cascades in the keV–MeV energy range [199, 200].

SHI irradiation of ceramic thin-layer systems leads to strong intermixing effects if the electron stopping power exceeds the track formation thresholds for both interface-forming materials [201, 202]. Above the threshold, the mixing rate scales with the square of the electron stopping power. The estimation of the effective diffusion constant shows that the mixing occurs in a molten track [202].

As was discussed in Section 4.2, the track formation threshold $S_{e,th}$ in many insulators can be predicted by a simple empirical model [174, 175] based on the thermal spike approach. According to this model, the track formation threshold is determined only by the energy Q necessary to heat the track region from the ambient temperature to the melting point of the matrix material, i.e., by its heat capacity c and the melting temperature T_m [$Q = \rho c(T_m - T_{irr})$, where c is the heat capacity of the atomic system, ρ is the material density, and T_{irr} denotes the irradiation temperature]. In Fig. 7, the intermixing thresholds derived from the experiments in Ref. [202] are presented by the data points when the heat capacity and the melting temperature are taken from the less sensitive component. Here, good agreement is observed between the prediction for track formation thresholds in [208] and the experimental mixing thresholds [202].

High-quality adhesion of metallic coatings on polymers is important for the fabrication of multilayer electronic systems and microtechnology. High cohesive strengths have been achieved (via irradiation by beams of Bi ions with $E = 0.3-2.6$ GeV and relatively low fluences of $10^7 - 10^{13}$ cm^{-2}) with a double-layer system consisting of a 300 nm thick copper film on a polychlorotrifluoroethylene (Teflon) substrate [209].

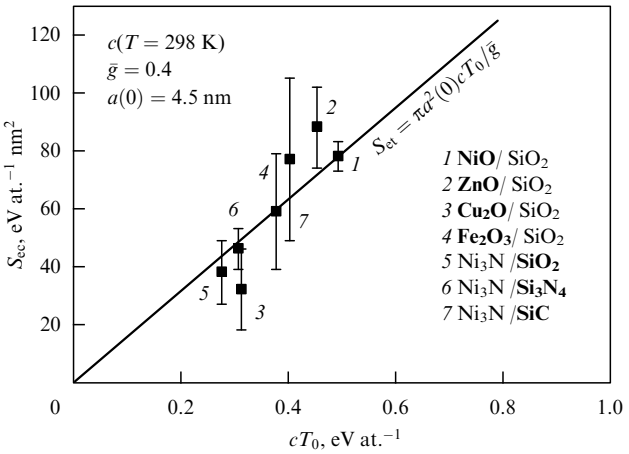

Figure 7. Experimental bilayer mixing thresholds S_{ec} (symbols) [202] compared with the semi-empirical track formation thresholds S_{et} predicted by the Szenes model [208] (solid line) (ρ is the mass density, c is the heat capacity, $T_0 = T_m - T_{irr}$, T_m is the melting point, and T_{irr} is the irradiation temperature).

6. Nanostructuring of solids by SHIs followed by track etching

Present-day heavy-ion accelerators provide beams with ion energies in the range 1–10 MeV a.m.u.$^{-1}$ and even 100 MeV a.m.u.$^{-1}$, which extends the treatment depth of materials to millimeters. However, the use of ions in the 10–100 MeV a.m.u.$^{-1}$ energy range is still very limited because of lower beam intensities and high costs. Commercial processes based on swift ion beams cover the energy range 1–10 MeV a.m.u.$^{-1}$. Latent ion tracks formed by SHIs can be preferentially etched, opened, and radially enlarged by attack with suitable corrosive solutions, which has been the basis for the wide use of irradiated foil materials as particle detectors and filtration membranes [1, 3]. With the advent of techniques that allow etched tracks to undergo controlled coating, doping, or filling with different elements or molecules, ion tracks are now viewed as attractive containment and templates for the fabrication of devices of micro- and nanoelectronics, nanooptoelectronics, and nanophotonics.

6.1 Threshold energy losses for etchable track formation in SiO_2 and Si_3N_4

Among other insulators, SiO_2 and Si_3N_4 play an exceptional role as materials of silicon micro- and nanoelectronics. The track technology to be developed for these materials is of great interest from the practical standpoint.

Two different approaches to the problem of correct interpretation of the amorphous track regions detected in quartz SiO_2 have been developed by French researchers [210, 211]: Toulemonde et al. [210] constructed the thermal spike model, which has become the standard in this area of research, while Douillard and Duraud [211] invoked the mechanism of the point defect peak. The defect structure of ion tracks in α-SiO_2 created by SHIs has been studied by IR absorption, XPS, and ESR [212]. These techniques showed that the atomic ring statistics and the number of bond scissions change differently with the ion dose.

The enhanced etching rate of irradiated α-SiO_2 has been tentatively attributed to the generation of planar three- and four-member rings of SiO_4 tetrahedra along the tracks instead of conventional six-member rings, with little evidence for a major role of E' centers (oxygen-deficient centers). The increased number of small rings, with a reduced mean bridging bond angle, has been linked to the revealed densification up to 3% of bombarded α-SiO_2 at large fluences of SHI [213–215]. Even with a reduced free volume, the strained Si–O bonds around the small ring structures can explain the increased etching rate along the track [216]. The formation of well-shaped cylindrical ion tracks requires electron excitation levels surpassing material-dependent thresholds S_e. The precise values somewhat depend on the experimental track detection method, the ion velocity, and the irradiation temperature [213, 217, 218]. At room temperature, continuous cylindrical tracks in quartz have been registered for $(dE/dx)_e$ larger than about 4 keV nm^{-1} [217, 219]. For vitreous silica, the track formation threshold is (2 ± 0.5) keV nm^{-1}, as obtained from ion hammering [220], and (4.0 ± 0.5) keV nm^{-1}, as derived from chemical etching [221]. Preferential track etching of vitreous SiO_2 thin films grown onto Si wafers and bombarded with swift ions requires a critical electron energy loss of ~ 2 keV nm^{-1} [215]. However, homogeneous etching, characterized by small cone opening angles and narrow distributions of pore sizes and associated with a continuous trail of critical damage, is only reached for $(dE/dx)_e > 4$ keV nm^{-1} [215]. The evolution of the etched track as a function of $(dE/dx)_e$ can be described by

the thermal spike model, assuming that the etchable track results from the quenching of a region that contains sufficient energy for melting [215, 217].

Some potential applications of ion tracks would benefit from cylindrical holes through a fused silica layer. In addition to being useful for nanometer and micrometer filters, such holes could be used as molds for electroplating electrical, optical, and magnetic structures and for other micro- and nano-science studies and technological applications [215, 222–224].

To control the etching of latent tracks and achieve a reproducible fabrication of SiO_2 layers with a high (up to 10^{11} cm^{-2}) density of nanochannels with a regular shape, it is very important to evaluate the crucial factors determining the process of track etching. Among these factors, the probability of latent track creation along each ion trajectory and the minimum size of a pore that can be etched in the track region are the most important ones. Under the condition that each swift ion creates a latent track, the pore density is determined by the ion fluence. A commonly used track 'etchability' criterion is the threshold electron stopping power S_{e0}. The corresponding values of S_{e0} range from 1.5 to 4 keV nm^{-1} for SiO_2. However, another criterion for the etchability of tracks was suggested in the interesting paper [215]. The i-TS model was used in Ref. [215] to calculate the conditions needed to produce etchable damage in the track region. The authors of Ref. [215] suggested that the etchable track results from the quenching of a zone that contains sufficient energy for melting. According to Ref. [215], track etching appears if the molten region radius is at least 1.6 nm. Homogeneous etching is achieved only for latent track radii larger than 3.0 nm.

Under the conditions that the latent track radii are larger than 3.0 nm and homogeneous etching take place, it can be expected that in the case of a larger molten radius, larger pores can be etched in the track region under the same etching conditions. This suggestion has been proved by recent experiments [225–227], which have revealed a correlation between the radii of molten regions calculated using the i-TS model and the sizes of nanopores etched in the track regions of vitreous SiO_2. The dependence of the pore characteristics (thickness, half-angle, upper and lower diameters) on the ion type, irradiation fluence, etchant concentration, and etching time have been studied [213, 225–227]. Moreover, it has been revealed that for $(dE/dx)_e > 16$ keV nm^{-1}, pore characteristics do not depend on the ion type [213]. In all cases, the half-angles of the etching cone are in the range of $17^\circ \pm 2^\circ$.

Table 4. Computer simulation results of track formation in SiO_2.

Ion type and energy, MeV	$(dE/dx)_e$, keV nm^{-1} (SRIM'2010)	Molten region radius r, nm (thermal spike model)	Molten region lifetime t, ps (thermal spike model)
Si (20 MeV)	3.6	1.5	1.2
Fe (56 MeV)	6.9	3.2	6.7
Kr (92 MeV)	9.2	4.4	12.1
W (180 MeV)	15.8	6.6	28.2
Bi (710 MeV)	23.8	7.8	41.1

In our study [227], a silicon oxide layer 930 nm thick was thermally grown on an Si (100) wafer. The SiO_2/Si samples were irradiated at normal incidence by different ions (20 MeV Si, 56 MeV Fe, 92 MeV Kr, 180 MeV W, and 710 MeV Bi) using three different accelerator facilities. The calculated values of the electron stopping power, radii, and lifetimes of the molten regions along swift-ion trajectories in SiO_2 are summarized in Table 4. We can see from this table that in the case of irradiation with 20 MeV Si ions, the molten region size is 1.5 nm. It nearly coincides with $r = 1.6$ nm reported in Ref. [215] as a threshold value of the melt region radius for the beginning of track etching. For 56 MeV Fe ions, this radius is 3.2 nm. Figure 8 shows sets of SEM images of irradiated samples after the etching procedure. The ion fluence did not exceed 10^9 cm^{-2} in any case. The irradiated samples were treated in a 4% hydrofluoric acid (HF) aqueous solution at room temperature for 6 min. To avoid artefacts, all samples were etched in the same etching process. The surface of the etched samples was then investigated using Hitachi S-4800 scanning electron microscope and a Solver P-47 atomic force microscope in the tapping mode. For the samples irradiated with 20 MeV Si ions, we can see that most of the ion impacts do not result in an etchable track formation and only a few of shallow and slightly defined pits with irregular shapes are

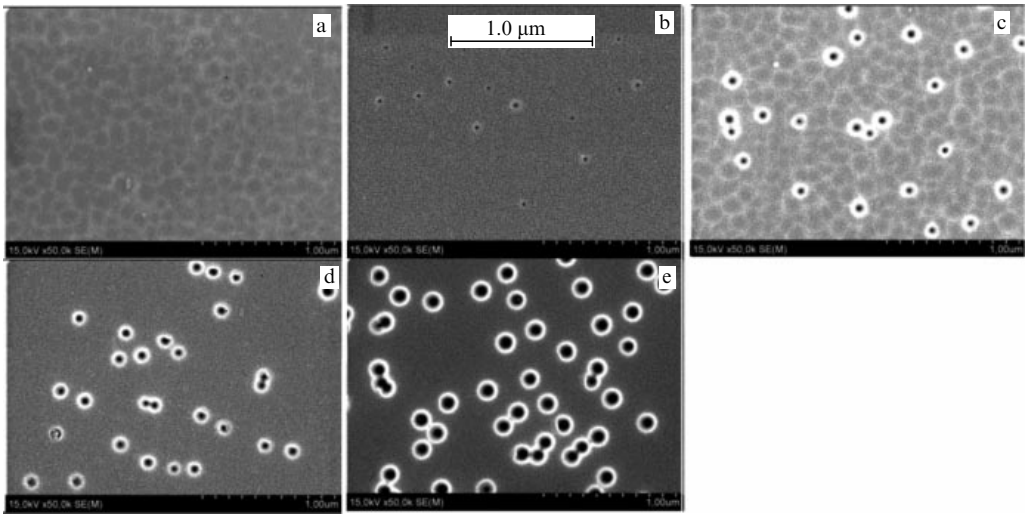

Figure 8. SEM images of etched SiO_2 surfaces: samples irradiated with (a) 20 MeV Si, (b) 56 MeV Fe, (c) 92 MeV Kr, (d) 180 MeV W, and (e) 710 MeV Bi ions.

Table 5. Irradiation regimes, mean densities, and sizes of etched pores and etching velocities V_t of SiO_2 in the track region.

Ion type and energy	Ion fluence, 10^8 cm^{-2}	Mean pore density N,* 10^8 cm^{-2}		Mean etched pore diameter D,** nm (SEM data)	V_t,*** nm min^{-1}
		SEM data	AFM data		
Si (20 MeV)	3.0 ± 0.23	0.09	0.1	—	—
Fe (56 MeV)	2 – 3	2.15	2.25	22.7 ± 5.1	19.4
Kr (92 MeV)	2.6	3.6	4.8	50.7 ± 10.8	22.1
W (180 MeV)	3	7.4	6.9	52.9 ± 14.0	29.1
Bi (710 MeV)	10	12.2	9.5	82.7 ± 5.6	33.3

* N was averaged over 3–5 images for each specific irradiation.
** D was averaged over 15–30 tracks for each specific irradiation.
*** $V_B = 18.3$ nm min^{-1} (V_B is the etching velocity of the bulk material). It has been calculated from the step height between the protected and unprotected regions of an etched virgin sample of SiO_2.

visible. These structures are difficult to estimate quantitatively because they merge with asperities of the surface roughness. In our case, for the 20 MeV Si irradiation, the calculated value of r is 1.5 nm (see Table 4), which is less than the discussed threshold value. Hence, the appearance of etched tracks for the samples irradiated with 20 MeV Si ions should not be expected. On the other hand, a distribution of clearly visible round pores appears after the etching of samples irradiated with other types of ions (see Fig. 8). AFM images were examined in Ref. [227] to make the track topologies clear. The mean values of the etched pore density and size, as well as the etching rates in the track region calculated from AFM and SEM images, are summarized in Table 5.

An analysis of Table 5 shows a reasonable correlation between the fluence and the calculated etched pore densities for all irradiation regimes, except for 20 MeV Si. We note that the smallest pore diameter ($D \approx 20$ nm) and the lowest etching velocity in the track region ($V_t \approx 19$ nm min^{-1}) are observed in the case of 56 MeV Fe. For this irradiation regime, the calculated radius of the latent track is 3.2 nm. This value is somewhat larger than the homogeneous track etching threshold [215]. A comparison between the fluence and the etched pore densities for the samples irradiated with 56 MeV Fe ions shows that practically each ion impact results in the formation of an etched track, which supports the good correlation between our results and the threshold latent track radius for homogeneous track etching predicted in Ref. [215]. An analysis of the data in Tables 4 and 5 reveals that under the conditions of our experiment, such parameters of etched tracks as D and V_t increase with the radius and lifetime of calculated molten regions. The tendency of pore size dispersion to decrease in the row from 56 MeV Fe to 710 MeV Bi should also be noted. Earlier, for α-SiO_2 samples irradiated with Bi (710 MeV), it was shown that the molten region radius can be used to estimate the smallest pore size that can be etched in the track region [228]. In this way, the results of track etching (pore density, size, and size dispersion) can be predicted based on the knowledge of the molten region radius. This procedure is of great importance for choosing the proper irradiation regimes aimed at preparing the nanoporous layers with high pore density ($\geqslant 10^{10}$ cm^{-2}) and small pore diameters.

We stress that the ion velocity effect plays an important role in nanopore formation. It was shown in [229] that the radii of the etched nanopores in SiO_2 glass irradiated with swift Cl ions significantly depend on the energy of the ions. Their radii have a maximum value at $\sim$ 15MeV and reduce with a further increase in energy. The role of this effect in SiO_2 glass and rutile TiO_2 single crystals was discussed in detail in [230].

The thermal stability of ion tracks in amorphous SiO_2 and the thermal stability of the system of pores produced by track etching in SiO_2 were evaluated in Ref. [225]. It was shown that defects in the regions of tracks were not annealed after 30 min of thermal treatment at 900 °C. Similarly, no changes were observed in the morphology of porous SiO_2 after 30 min of thermal processing at this temperature.

Presently, in contrast to results for SiO_2, less information is presented in the literature on track formation in Si_3N_4 [16, 231–237]. The observation of amorphous tracks in β-Si_3N_4 single crystals irradiated with 710 MeV Bi ions was reported in [232], and etched tracks in amorphous silicon nitride exposed to ions of 110 MeV Pb and 710 MeV Xe were examined in [233].

In our study [231], amorphous silicon nitride thin films 600 nm in thickness were deposited on p-type Si (100) substrates by gas-phase low-pressure deposition from ammonia and dichlorsilane. The Si_3N_4/Si samples were irradiated with Fe (56 MeV), Kr (84 MeV), and W (180 MeV) ions. The respective electronic energy losses of Fe, Kr, and W ions were 9.0, 11.9, and 20.4 keV nm^{-1}. Chemical etching was then performed in a 4% aqueous solution of HF at room temperature. The irradiated samples were studied by means of SEM and AFM. In the samples irradiated with Fe and Kr ions, no tracks were revealed even after a 60-min treatment in the HF solution. The etched tracks were observed only after the exposure of the Si_3N_4/Si samples to W ions, with the level of inelastic energy loss of 20.4 keV nm^{-1} being maximal in this experiment. Moreover, the low track etching efficiency and the considerable difference in the diameters of the etched pores allow us to assume that discontinuous tracks are formed in silicon nitride upon irradiation with 180 MeV W ions. Such a conclusion on the formation of discontinuous tracks in amorphous Si_3N_4 irradiated with Pb ions with the energy loss of 19.3 keV nm^{-1} was also drawn in [233].

Ion tracks in amorphous Si_3N_4 films (20 nm thick) produced by 120–720 keV C_{60}^{2+} ions were directly observed using TEM and HAADF-STEM [234]. The density at the track center was about 80% of the bulk Si_3N_4 density. This low-density core is surrounded by a higher-density shell (1–2% larger than the bulk density). In this study, continuous tracks 2 nm in radius were formed even if the inelastic energy loss was smaller than 20 keV nm^{-1}. Recalling that the nuclear energy loss is comparable to the electronic energy loss, the authors of Ref. [234] note the effect of nuclear stopping on the track formation. Recently, the important role of nuclear

stopping in the track formation in α-SiO_2 irradiated with 0.3–15 MeV Au ions was clearly demonstrated in [234]. To confirm the role of the nuclear stopping in the track formation, a film of α-Si_3N_4 was also irradiated with 200 MeV Au^{14+} ions [234]. The effective inelastic energy loss in these films was about 20 keV nm^{-1}, which is a few times larger than the electronic energy loss of 120–720 keV C_{60} ions. Although (discontinuous) ion tracks were clearly observed in Ref. [235], the radius of the registered tracks was much smaller than that for C_{60}. It was revealed that the length of ion tracks produced by 720 keV C_{60}^{2+} ions in 30 nm films is shorter than that produced in 20 nm films [235]. This can be qualitatively understood in term of the energy dissipation process in the near-surface region [235].

6.2 Track formation in polymers and modification of their properties

The interaction of energetic ion beams with polymers has been studied by numerous groups investigating radiation-induced degradation and track formation by means of spectroscopy (e.g., IR, FTIR, UV-Vis, Raman), high-resolution microscopy (e.g., scanning and transmission electron microscopy), X-ray diffraction, ESR, electrical conductivity, and other techniques [238–247]. Chemical etching of ion tracks has also been analyzed in great detail in order to control the fabrication of ion-track membranes and thus enable new applications [248–258].

SHI irradiation of polymers has been found to produce useful modifications of their physical and chemical properties. An increase in hardness, strength, and wear resistance [259–261], electrical conductivity [262–264], density [263], chain length [259–261], crystallinity [260–263], and solubility [259–263], and improvements in the optical transmission [261–264] properties of polymers have been reported. These changes depend on the sample parameters such as the composition, molecular weight, and temperature and the ion-beam parameters such as the ion energy, mass, and fluence. The primary phenomena associated with the interaction of ion beams with polymers are cross-linking, chain scissions, and emission of atoms, molecules, and molecular fragments [244–265]. In the last steps of degradation, it is generally believed that a carbonaceous material is formed with a variable sp^2/sp^3 ratio, where sp^2 bonding seems to be favored by the electron excitations [266].

The concentration of the transients and final degradation products is expected to be an increasing function of the energy locally deposited by the ion. For ions with an energy of 0.5–100 MeV a.m.u.$^{-1}$, 65–75% of the energy is transferred to and then transported by secondary electrons, 15–25% is spent to overcome their binding energies, and the residual 5–10% produces neutral excited states [267].

The most important products of the transient reactions in polymers are low-mass stable fragments and cross-linked two- or three-dimensional structures. Their local concentrations depend on the initial concentration of the transients, their type, and prevailing chemical reactions, the last two being affected by the polymer structure. On the other hand, the relative concentrations of different degradation products and intact polymer macromolecules affect local macroscopic properties of the irradiated material, such as its enhanced etchability by inorganic agents, which is important for the application of polymers in dosimetry [268] and micro- and nano-membrane production [250–254, 269]. The etching is also a valuable tool in studying the internal structure of latent tracks, especially the distribution of the degradation products [270].

Table 6. Radiation characteristics of generic polymers.

Mainly crosslinking	Mainly scission
Polyethylene	Polyisobutylene
Polyacrylates	Polymethacrylates
Polyvinyl chloride	Polymethylstyrene
Polysiloxanes	Polymethacrylamides
Polyamides	Polyvinylidene chloride
Polystyrene	Polytetrafluoroethylene
Polyacrylamides	Polypropylene ether
Ethylene vinylacetate	Cellulose

Table 7. G values for crosslinking and chain scission in common polymeric materials.

Polymeric material	Crosslinking $G(X)$	Scission $G(S)$	Ratio $G(S)/G(X)$
Low-density polyethylene	0.8 – 1.1	0.4 – 0.5	0.47
High-density polyethylene	0.5 – 1.1	0.4 – 0.5	0.56
Polyvinylidene fluoride	1.00	0.30	0.30
Polymethylmethacrylate	0.50	0.77	1.54
Polymethylacrylate	0.50	0.04	0.08
Nylon 6	0.67	0.68	1.01
Nylon 6,6	0.50	0.70	1.40
Polyvinylacetate	0.30	0.07	0.23
Atactic polypropylene	0.27	0.22	0.81
Isotactic polypropylene	0.16	0.24	1.50
Polystyrene	0.019 – 0.051	0.094 – 0.190	0.41
Natural rubber	1.05	0.1 – 0.2	0.14
Polybutadiene	5.3	0.53	0.1
Polytetrafluoroethylene	0.1 – 0.3	3.0 – 5.0	20
Polyisobutylene	0.5	5.0	10
Cellulose	(low)	11	(high)

Both polymer crosslinking and degradation by chain scission occur during radiation treatments, but one or the other of these effects can be predominant in some materials. Examples of both types are presented in Table 6 [271]. The G values for crosslinking $G(X)$ and for chain scission $G(S)$ in a number of pure polymeric materials are given in Table 7 [272]. Materials with the $G(S)/G(X)$ ratios below 1.00 are favored for crosslinking process. The values of $G(X)$ and $G(S)$ change with both ion fluence and irradiation conditions such as temperature.

A phenomenological model describing latent track formation and its radial structure in a simplified manner was proposed in [265, 273]. This model supposes that the latent track consists of three components: the low-mass degradation products, cross-linked material, and intact polymer macromolecules with radially dependent relative concentrations $C_f(r)$, $C_s(r)$, and $C_m(r)$. The relative concentrations are calculated from the initial concentration of the transients $q(r)$ as

$$\begin{aligned} C_f(r) &= k_f q(r) q(r) N^{-1}(r)\,, \\ C_s(r) &= k_s q(r)\big(1 - q(r)\big) N^{-1}(r)\,, \\ C_m(r) &= \big[1 - q(r) - k_s q(r)\big(1 - q(r)\big)\big] N^{-1}(r)\,, \\ N(r) &= 1 - q(r) + k_f q(r) q(r)\,, \end{aligned} \tag{6.1}$$

where k_f and k_s are the respective dimensionless effective reaction constants for mutual recombination of the transients leading to stable, low-mass fragments and for the reaction of

the transients with macromolecules leading to cross-linked structures. The normalization factor $N(r)$ in fact gives the total number of products of all kinds. No diffusion of transients or their reaction products from the site of their origin is supposed.

The local concentration of the transients is calculated as

$$q(r) = 1 - \exp\left(-Ge(r)\right), \tag{6.2}$$

where G is the radiation yield of transients and $e(r)$ is the density of the energy deposited by the ion and secondary electrons, which is approximated by Tombrello's formula (see Eqn (8.1) in Ref. [1]) with $\gamma = 0.27$ and $R_1 = 84\varepsilon/\rho$ (where ε is the ion energy in MeV a.m.u.$^{-1}$ and ρ is the polymer density in g cm^{-3}).

With this model, the radial distribution of different reaction products was calculated in [265] as a function of the energy deposited by the ion and penumbra radius in polyimides irradiated with 11.4 MeV a.m.u.$^{-1}$ Xe and Bi ions. These data were used to describe the results of etching experiments with this polymer [270]. As was noted in [265], the model can describe the observed radial dependence of the radial etch rate with reasonable values of free parameters (γ, k_f, and k_s). The discussed model could be developed further by accounting for different transient species, their specific reaction mechanisms, and diffusion.

Presently, two models are mainly used to describe the conversion of the energy of excited electrons to the kinetic energy of target atoms in polymers. The Coulomb-explosion model is based on the assumption that the intense ionization and excitation along the ion path leads to an unstable zone in which atoms are ejected into the nonexcited region of the sample by Coulomb repulsion [274]. The second model is the thermal-spike model adjusted by Szenez [275] for polymers. The analysis of polyimide (PI) films irradiated with 1.158 GeV Fe^{56} and 1.755 GeV Xe^{136} ions in [238] shows that the predictions of the thermal spike model [275] are in qualitative agreement with experimental results on the mean radii of degradation and alkyne formation in tracks.

In the 1990s, detailed studies were undertaken with the aim of clarifying basic chemical mechanisms of radiolysis in some SHI-irradiated polymers: polyethylene (PE), poly(vinylidene)difluoride (PVDF), polypropylene (PP), polybutene (PB), and polystyrene (PS) [276–279], as well as polycarbonate (PC) [280–283]. *In situ* Fourier-transform infrared (FTIR) spectroscopy indicates alkyne formation in all irradiated polymers. This method was used in Ref. [284] to study the chemical modifications in bisphenol A–PC induced by C^{13}, Ne^{20}, Ca^{48}, and Xe^{129} ions with an energy of a few MeV a.m.u.$^{-1}$. That polymer is widely used today to prepare track-etched membranes with a pore shape and size very well controlled within diameters from 10 to 100 nm [285]. These membranes are then used as templates for nanotubes and nanowire fabrication [286, 287]. *In situ* FTIR spectroscopy shows that low-$(dE/dx)_e$ SHI radiolysis of PC is characterized by a high sensitivity of carbonate groups to irradiation, as opposed to isopropyl and aromatic group sensitivity. As a result of the carbonate group destruction, phenol groups are formed in significant concentrations. Considering the value given to the phenol molar absoption coefficient, it could be assumed that one carbonate bond scission would lead to roughly one phenol creation. When $(dE/dx)_e$ increases, both isopropyl groups and aromatic groups show a higher sensitivity to radiolysis than at low

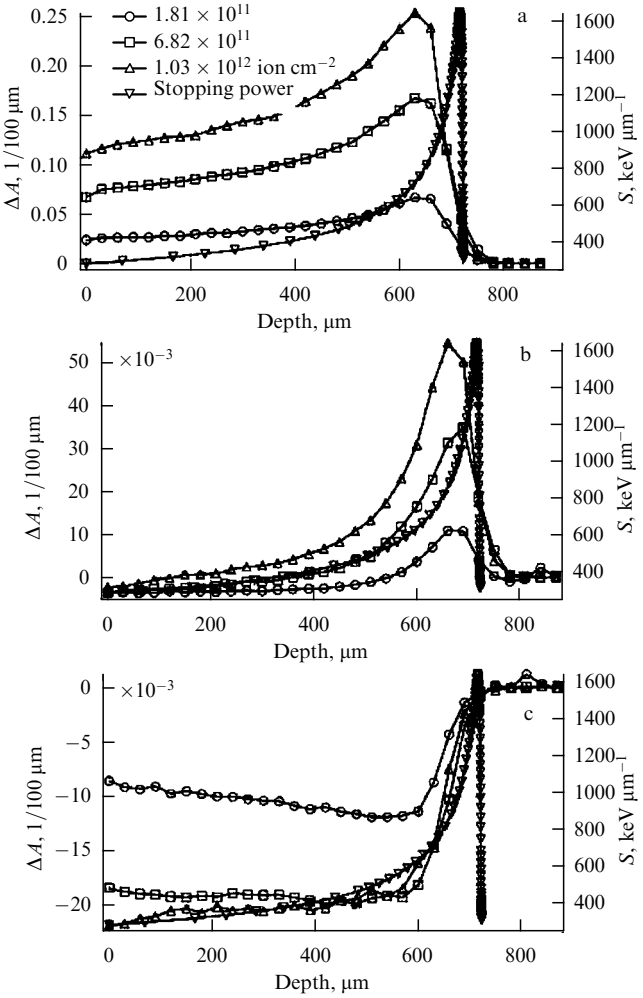

Figure 9. Depth profile of IR absorption due to (a) trans-vinylene, (b) end-vinyl, and (c) vinylidine of LDPE irradiated with 350 MeV Ne^{8+} under various fluences, together with the depth profile of the stopping power [289].

$(dE/dx)_e$. However, the carbonate groups are still the most sensitive. Furthermore, there is a $(dE/dx)_e$ value between 3.5 and 19.5 MeV mg^{-1} cm^2 at which a maximum for the radiochemical yield of phenol creation is attained.

PC (Makrofol kg) film stacks were irradiated with 15.14 MeV a.m.u.$^{-1}$ Xe^{136} and 11.4 MeV a.m.u.$^{-1}$ U^{238} in the fluence range $9 \times 10^9 - 1 \times 10^{12}$ ion cm^{-2} [288]. The FTIR results show that aromatic ether and methyl group are more sensitive to irradiation than para-substituted phenyl. The alkyne and alkene groups are induced by irradiation. Progressive amorphization process of this PC with increasing fluence is traced by XRD measurements [288]. The obtained cross sections of these processes are always augmented with increasing $(dE/dx)_e$ in the scope of the discussed experiment. Amorphization occurs with the largest radius in the latent track, and the formation radius of alkyne is larger than the destruction radius of the chemical group.

The distribution of the local transformations induced in low-density polyethylene (LDPE) irradiated with various ions was investigated by using micro-FTIR [289] (Fig. 9). The predominant transformations induced by irradiation are cross-linking, trans-vinylene, end-vinyl, and vinylidine formation. The depth profile of μ-FTIR for trans-vinylene

resembles the Bragg curve for energy losses, but each of the end-vinyl and the vinylidine shows a rather complicated profile (see Fig. 9). Under high-fluence irradiation, ion tracks overlap, causing a complicated dependence of the local chemical transformations on the stopping power. Semicrystalline high-density polyethylene (HDPE) samples were irradiated with 1.157 GeV ^{56}Fe ion beams to fluences ranging from 1×10^{11} to 6×10^{12} cm^{-2} [290]. SAXS investigations revealed that the track is composed of a core (possible clusters of carbon-rich materials) about 5.3 nm in radius, characterized by a significant density deficit compared to the virgin HDPE, surrounded by a shell about 4.3 nm in thickness with less density reduction [290].

Many experiments on low-energy ion irradiation (< 1 MeV) of intrinsically electron-conducting polymers were reported by several groups [273, 291, 292]. SHI ($E > 1$ MeV a.m.u.$^{-1}$) irradiation of polymers is a more novel technique to enhance/alter the conductivity. Polythiophene and its derivatives are some of the most important conducting polymers for their potential applications in various devices and also for their n-dopability [293, 294]. Poly(3-methylthiophene) conducting polymer thin films ~ 25 μm thick doped with $LiClO_4$ and $LiCF_3SO_3$ were irradiated with 120 MeV Si^{9+} ions at different fluences of 5×10^{10}, 5×10^{11}, and 3×10^{12} ion cm^{-2} [295]. The electric conductivity measurements show up to a 70% increase in the DC conductivity of the polymer films upon SHI irradiation, which is ascribed in [295] to the cross-linking of the polymer chains. Up to a 75% increase in the degree of crystallinity has been observed upon SHI irradiation, decreasing the interchain hopping resistance. The increase in the degree of crystallinity with the increase in fluence gives rise to an increase in the electric conductivity.

Stacks of polyimide (Kapton) foils were irradiated with various SHIs (Ti, Mo, Au) with the energy 11.1 MeV a.m.u.$^{-1}$ and fluences between 1×10^{10} and 2×10^{12} ion cm^{-2} [243]. Although Kapton is known to be highly radiation resistant, pronounced degradation is observed under irradiation by SHIs. An FTIR spectroscopy study in the UV and visible spectral range shows that the absorption edge is shifted to larger wavelengths, indicating carbonization. Such modifications are linked to the deposition of a critical dose of 2.7 MGy (Ti) and 1 MGy (Mo, Au). The conductivity of the irradiated Kapton foils was significantly increased, depending on the ion species and dose, up to three orders of magnitude (Fig. 10).

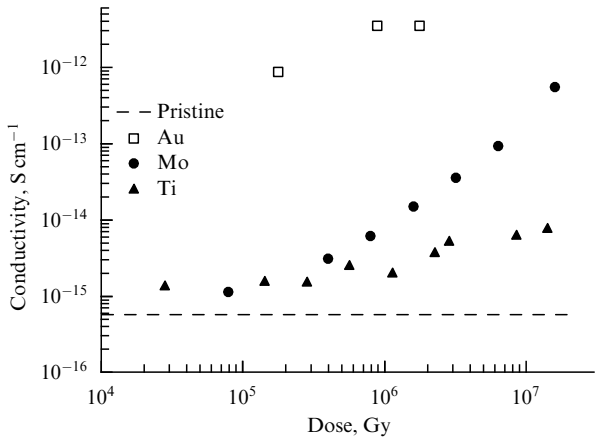

Figure 10. Electric conductivity (at 0.1 Hz) as a function of the irradiation fluence [243].

The dose D deposited on foils is

$$D_{\mathrm{Gy}} = 1.6 \times 10^{-10} \frac{E\Phi}{\rho d}\,, \tag{6.3}$$

where the dose D_{Gy} is given in Gy, E is the total ion energy in MeV, Φ denotes the fluence in ion cm^{-2}, $\rho = 1.43$ g cm^{-3} is the mass density, and d is the foil thickness in cm. Upon ion-beam irradiation, the absorbed dose should be different at local positions along the ion pathway because the stopping power is different along this pathway. We can calculate the local absorbed dose D_{Gy} given the depth profile of $(\mathrm{d}E/\mathrm{d}x)_{\mathrm{e}}$ and the fluence as

$$D_{\mathrm{Gy}}\ [\mathrm{kGy}] = \frac{1.60217}{10^{14}} \frac{(\mathrm{d}E/\mathrm{d}x)_{\mathrm{e}}\Phi}{\rho}\,, \tag{6.4}$$

where $(\mathrm{d}E/\mathrm{d}x)_{\mathrm{e}}$ is the electron energy loss in keV μm^{-1}, D is the fluence in ion cm^{-2}, and ρ is the target density in g cm^{-3}.

In the case of polyimide Kapton-H (pyromellitic dianhydride-oxidialinine, PMDA-ODA), an extensive study of thin films homogeneously damaged in the bulk by SHI irradiation was performed in [296, 297]. Irradiation with 30 MeV C, 30 MeV F, 50 MeV S, and 60 MeV Cu ions can induce an insulator–conductor transition with an electric conductivity increase by up to 18 orders of magnitude. Furthermore, the insulator–conductor transition in polyimide can also be obtained with light and heavy-ion implantations in the 100 keV energy range [297, 298]. Using conductivity and EPR data, it was shown that the transition induced by SHI irradiation proceeds through four stages (I, II, III, IV) [296, 297]. During stages II and III, the onset and growth of conduction corresponds to the progressive formation of a 3D graphite-like structure when track overlaps increase. In stage II, the material is a semiconducting polymer matrix doped with irradiation defects and graphitic clusters, whereas in stage III, hopping occurs between the clusters. In stage IV, true 3D percolation of the disordered π-bonded clusters occurs. A similar analysis was used for ion-implanted polyimide (PI), with a transition from the insulating phase to a true semiconducting one, and then to a conducting amorphous carbon, where electronic excitations were shown to play a major role in producing such an sp^2-bonded structure [297].

Irradiation of polyimide Kapton-H was also performed with 650 MeV Ni, 843 MeV Xe, 2.6 GeV Xe, 1.1 GeV Ta, and 707 MeV Pb ions that were transmitted through polymer films with $(\mathrm{d}E/\mathrm{d}x)_{\mathrm{e}}$ ranging between 3.5 and 17.7 keV nm^{-1} [299]. A conductivity about 8–9 orders of magnitude smaller was reached with the swifter ions with respect to the ions in the 1 MeV a.m.u.$^{-1}$ energy range. The slower ions were thus found to be more efficient in inducing sp^2-bond clustering and percolation. The damage yield deduced from EPR data is found to decrease with the ion energy. This is interpreted in terms of an ion velocity effect on damage due to the dilution of the deposited energy in the case of swifter ions.

Polytetrafluoethylene (PTFE) foils were irradiated with Xe, Au, and U ions with energies from 0.9 to 1.5 GeV and fluences between 1×10^8 and 1×10^{13} ion cm^{-2} [246]. PTFE is a semicrystalline material, with its linear chains adopting complicated helical configurations, where the F atoms cover the backbone chain and ensure the strong chemical stability of the polymer. The damage process is described in Ref. [246]

as essentially scission of the backbone chain accompanied by the split of F atoms, as well as the creation of double bonds and the cross-linked structures in the ion tracks. The damage area is directly related to the stopping power of the incident ion. Moreover, the damage process involves a decrease in the crystallinity of the polymer and an increase in its transparency. Estimated radii of the latent tracks reach 2.9 ± 0.8 nm for Xe (1.5 GeV), 4.5 ± 0.9 nm for Au (0.9 GeV), and 5.6 ± 0.8 nm for U (1.3 GeV) ions.

Structural, electrical and morphological properties of free-standing polyaniline (PANI) films irradiated with 50 MeV Li^{3+} and 90 MeV C^{6+} ions were studied in Ref. [300]. It was shown that the crystalline nature of the PANI films increases with the ion fluence, followed by a decrease beyond the critical ion fluence. The conductivity of films increases with the formation of clusters and craters at higher fluences [300]. A significant increase in DC conductivity for PANI films irradiated with Ni^{12+} and Si^{9+} ions was observed in Ref. [301].

The fluence of iodine ions (55 MeV) less than 10^{13} ion cm^{-2} in polyimide films produced semiconducting nanochannel arrays with good electric conductivity along the ion tracks and negligible charge transport between tracks [302]. Irradiation of PI films at fluences greater than 10^{14} ion cm^{-2} led to the formation of incorporated semiconductor nanochannel arrays with considerable overlapping. This provides polymers with enhanced electrophysical properties by means of mixed modes of charge transport: electron hopping along the tracks and electron tunneling between the tracks [303].

Oxygen and carbon were rapidly lost from the PI film, whereas little nitrogen was lost for fluences less than 5×10^{12} 55 MeV iodine ion cm^{-2} [247]. However, up to 60% of nitrogen was lost from the PI film irradiated to a fluence of 3.5×10^{13} ion cm^{-2}. The fluence dependence of gas loss indicates multi-step processes of structure transformation and gas release, as discussed above.

6.3 Current and future applications of etched tracks

The radiation-enhanced etchability of tracks created by SHIs in polymeric substrates has long been recognized as a property of technological importance. Ion tracks can be preferentially etched, opened, and radially enlarged by attack with suitable corrosive solutions, which has been the basis for the wide use of polymer foils as particle detectors and filtration membranes [3, 304]. With the advent of techniques that allow etched tracks to undergo controlled coating, doping, or filling with atoms or molecules, polymeric ion tracks are now viewed as an attractive containment and templates for the fabrication of materials and devices of nanoelectronics, nanooptoelectronics, and nanophotonics [250–254, 305–307].

The enhanced chemical etchability of polymeric ion tracks is attributed to the reactivity of alteration products. The highly porous structures of swift-ion tracks observed in PET [308], PI [309], and PC [310] strongly suggest that the track formation mechanism is the spatially confined radiolysis combined with the release of resulting gases and volatile molecules. This suggestion is supported by complementary data on heavy-ion-induced gas release [247]. Radiolysis is directly activated by primary reactive species formed upon energy deposition. The transport of gases and volatile alteration products to the foil surface occurs via permeation, most likely through depleted tracks. Porosity undoubtedly accelerates through-track transport of etchants and inert agents, and is therefore a desired property for track applications.

According to the well-known model [3], the process of track etching is mainly determined by two quantities: the etch rate of the highly damaged track core, V_T, and the etch rate of the bulk material, V_B. If V_T and V_B are of the same order of magnitude, the etch pit is a cone. The sharpness of the cone tip depends on the diameter d_T of the damage zone around the ion track. To obtain calibrated pores cylindrical in shape, the track etching rate must be considerably higher than the etching rate of the undamaged material. In polymers, the size of the highly damaged track core is normally a few nanometers.

Various surfactants are often added to the etching solution to improve the wetting of the sample [311]. The process of track etching in the presence of surfactants is significantly modified according to the following scheme [311]:

- Molecules of the surfactants can be absorbed on the surface and alter its susceptibility to chemical attack. The formed surfactant layer is quasi-solid and partially protects the surface from the etching agent.
- Molecules of most surfactants are a few nanometers in size, which is comparable to the radius of the preferentially etched track core.
- The diffusion rate of nanosize surfactant molecules within a restricted volume can differ significantly from the diffusion rate of smaller molecules responsible for chemical etching.

A surfactant-controlled method of design allows adjusting geometrical parameters of pore profiles, providing them with unusual properties (Fig. 11).

To increase the track etching rate, various methods of sensitization are also used: oxidization with oxygen in the air or with ozone, photo-oxidization, and the action of different solvents. At the stage of sensitization, the radiation damage in the track increases, which enables the track etching rate to be additionally increased tenfold or more [253, 312, 313]. In Ref. [313], the sensitization mode in Ar ion irradiated PET included two stages: UV illumination in the wave range 320–360 nm and treatment with dimethylformamide (DMF) at room temperature for 10 min. It was shown that after such sensitization at a relatively low etching temperature (55 °C) in a weak etchant (2N solution of NaOH), through pores were etched with diameters ranging from 70 nm to several micrometers. The film thickness barely changes under such a treatment. As with the irradiation with heavier ions, pores of all sizes have a regular cylindrical shape [313] (Fig. 12). In Fig. 12, a membrane with pores 0.25 μm in diameter is shown. The pore density is about 10^8 cm^{-2}. It is clearly seen in the inset that the pore diameter in the bulk of the film is the same as on the surface, and all the pores have a regular cylindrical shape. The porosity of such a membrane is about 10%.

Another option for revealing tracks is to initiate the polymerization of other monomers (radiation grafting process along the ion tracks) [314]. To produce track membranes with submicroscopic pores, PVDF foils have been irradiated with Cl, Ag, and Pb ions [314]. They were then chemically etched and grafted with acrylic acid. These PVDF polymers with grafted pores can be used in biomedical applications because of their variable permeability to a drug, which could make them suitable for controlled drug release devices [314]. Previous saturation of a kapton polymer with styrene for many hours was followed with the irradiation [315]. Thus, the

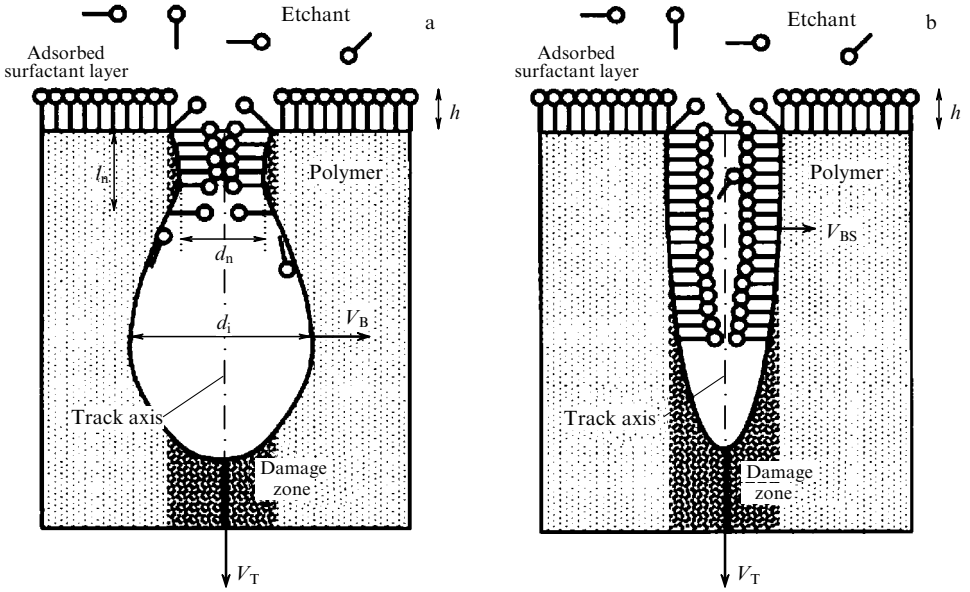

Figure 11. Initial stage of track etching in the presence of nanosize surfactant molecules: (a) fast etching; (b) slow etching. The circles represent hydrophilic head groups and the tails represent the hydrophobic parts of the surfactant molecules [311].

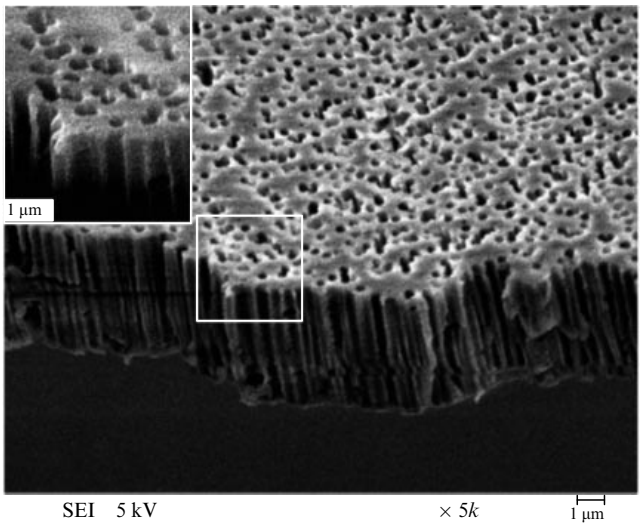

Figure 12. Membrane obtained by etching the PET film that was irradiated with argon ions [313]. The etching duration was 1 h 30 min. A cross section of the film under higher magnification outlined with a white rectangular is shown in the inset. The pore diameter is 0.25 μm.

grafting and irradiation occur simultaneously. For grafted ion-track membranes, reduced pore sizes that increase the H_2/D_2 separation ratio are observed [315].

PC and PET membranes are commercial products on the world market [316]. A high etch rate ratio is achievable, which makes it possible to produce a wide range of membranes with different pore diameters. Alkali solutions are used to develop tracks.

PCs are the materials that have been used for membrane production since the 1970s [3]. Compared to PET, the sensitivity of PCs to treatments is higher, which allows producing membranes with a pore diameter as small as about 0.01 μm.

Chemical etching in strong oxidizers is effective in developing latent tracks in PP [317]. PP is interesting as a material for membranes to be used for the filtration of some aggressive liquids, such as strong alkali solutions or inorganic acids.

PVDF is one of the most resistant commercially available polymers. Its bi-axial β-phase has additional interesting technological features, such as piezo- and pyroelectric properties. Production of track-etched membranes using chemical etching of irradiated PVDF films was reported more than ten years ago [318]. However, there is renewed interest in making membranes with pore diameters in the nanometer range.

Track membranes with pore diameters of molecular dimensions have direct application in molecule and ion sensing through the resistive-pulse sensor method [255, 257, 319]. Another interesting application comes from the introduction of chemical selectivity in order to perform molecular recognition by endowing membranes with the selective permeation function. Specific chemical interactions between solutes and the modified nanopore walls can alter the transport properties [320, 321].

However, most of the advances have been associated with commercial track-etched membranes modified with gold deposition by the electrolysis plating method to reduce the pore diameter [322]. Several authors have tested different oxidant solutions to produce tracks in PVDF foils [318, 323, 324]. Most chemical solutions failed to produce damage, with the exception of a permanganate solution in alkaline media. To produce nanometer-scale membranes, a solution of KOH 9 mol l^{-1} saturated in $KMnO_4$ was the best etching reactant in PVDF. A temperature ranging between 55 °C and 65 °C was optimal to produce cylindrical pores.

Nanowires with diameters in the range 10–100 nm have attracted increasing interest due to their fascinating properties and unique applications related to the restricted size [325]. The template-based method, which consists in filling a host porous medium with one or more desired materials, is now commonly used for the synthesis of polymeric, semiconducting, or metallic micro- or nanomaterials in wires or tubules [254, 326–328]. The track-etch templates enable synthesizing wires or tubules [326] (Fig. 13) with a well-controlled size and

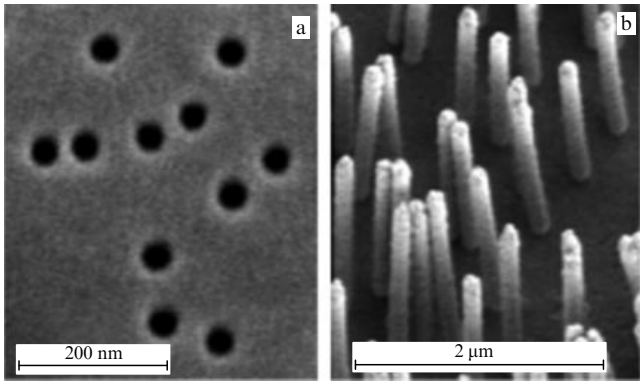

Figure 13. (a) Example of a polycarbonate track-etch template; (b) such track-etch templates enable synthesizing wires (Co) or tubules (Au, polypyrrole) with a well-controlled size and shape and exhibiting small roughness and a large aspect ratio (pictures by scanning electron microscopy) [326].

shape and exhibiting small roughness and a large aspect ratio; sizes from 10 nm to several μm with the length-to-diameter ratio in the range 10–1000 can be scanned from 10^5 to 10^{10} cm^{-2}, corresponding to the respective mean separation distance from several dozen μm to 10 nm. Polycarbonate ion-multitrack membranes with pore diameters on the nanometer scale are appropriate templates for electrochemical fabrication of arrays of metallic nanowires [3, 326, 329]. The high solubility of the PC templates in organic solvents provides access to the wires for further characterization. The orientation of the pores and hence of the nanowires with respect to the polymer layer surface can be easily monitored by SEM (see Fig. 13). Applications of track membranes as templates for the synthesis of micro- and nanowires and tubes, as well as textured surfaces with special optical properties are reviewed in [330].

Presently, conical and doubly conical nanopores are attracting great interest due to their potential in modern and rapidly growing fields including molecular sensors, logic gates, nanoactuators, and various nanofluidic devices (see [257] and the references therein). Special interest is attracted to single nanopores, because they can serve as a unique device for molecular recognition [257]. Such nanopores that are conical in shape possess ionic selectivity and diode-like voltage–current characteristics in electrolyte solutions [255, 257].

Electrochemical deposition in membranes containing only one etched ion track has been successfully used to fabricate single-metal and semimetal nanowires [331–333]. For an electrical contact, the wire remains embedded in a polymer matrix and is reliably connected to an external circuit by sputtering a second macroscopic electrode on the foil surface of its front-end side [327, 330]. Such a system enables measuring the electron transport properties of nanowires with well-defined sizes and shapes.

In Ref. [327], a system for fabricating a specified number of ion-track nanochannels and nanowires, from a few hundred to one, is described. The ion tracks can be etched to a proposed diameter and the system can be programmed to electroreplicate nanochannels in a preferable sequence of magnetic/nonmagnetic metals, alloys, or semiconductors [327]. Such individual nanochannels and nanowires have been variously used, including as weak links between adjacent superfluid volumes [334], as PH-sensitive, current-rectifying, and asymmetric apertures [335], for giant magnetic resistance-based magnetic field sensors [336], and for the detection and controlled translocation of single molecules [337].

The main limitation of track-etched templates made of thick polymer films is the low pore filling rate in electrodeposition experiments when the pore size is less than about 30 nm. Typical values of pore-filling rates are higher than 90% at 30 nm, but they rapidly decrease below 1% for pore sizes less than 15–20 nm [326], probably due to a low wetting of the pores by the electrolytic solution.

The filtration process, cell culture, and laboratory filtration are categories of commercial applications of track membranes [249, 330]. The purification of deionized water and air in microelectronics and blood in medical practice, the filtration of beverages and drugs, and the separation of various suspensions are typical examples [249, 330]. Porous membrane filters are now recognized as providing significant advantages for separating bacteria, cultivating cells, and studying cellular activities [338, 339].

Etched tracks can be filled, in principle, with any material. Various techniques to accomplish this procedure — such as galvanic deposition, chemical deposition, grafting, pressure injection, *in situ* polymerization, evaporation, and the introduction of colloidal solutions — have been developed over the past fifteen years [332, 340, 341]. Many novel applications of etched tracks in electronics have already been demonstrated, such as the development of field-effect transistors [342], light-emitting diodes [343] and transistors [344], magnetic field sensors [345], sensors for temperature [346], pressure [346], and humidity [335, 347], MEMS devices [348], molecular switches [349] and field emitters for displays [223], microcapacitors [340], and multiple wire microvia interconnects in printed circuit boards (PCBs) [350]. The MOS-type hybrid structures TEAMS (tunable electrically anisotropic material on semiconductor) [351] and TEMPOS (tunable electronic material with pores in oxide on semiconductor) [318, 352], consisting of a silicon/insulator bilayer system into which conducting tracks are inserted and which are eventually combined with nanoclusters (NCs), NC/polymer composites, or carbon nanotubes, were demonstrated in [351–353] to be of special electronic interest due to their great versatility. Electronic elements based on this concept combine many practical properties, such as negative differential resistances, sensing, AND/OR logic, and light emission in an unconventional way [353].

There is a wide range of other applications linked to direct patterning of irradiated materials or to depositing material into the pores of etched ion-track membranes.

The conducting ion tracks in diamond-like carbon films are useful structures for building nanodevices, such as single-electron transistors and field-emission cathodes [354].

Ion-track projection lithography has been demonstrated several times, e.g., in [355–357], with a recent extension into nanolithography with pattern transfer into amorphous SiO_2 and TiO_2 [357–359]. Ion-track lithography using homogeneously irradiated foils can be made affordable for use in flex PCBs [350]. Figure 14 illustrates through-hole vias fabricated by ion-track lithography in a metal-clad polyimide foil [341].

Ion-track membranes of high porosity constitute a randomly inhomogeneous medium that not only transmits X-ray or extreme ultraviolet (EUV) radiation and blocks long-wavelength UV radiation but also transfers a high-quality focused imaging pattern for further registration by

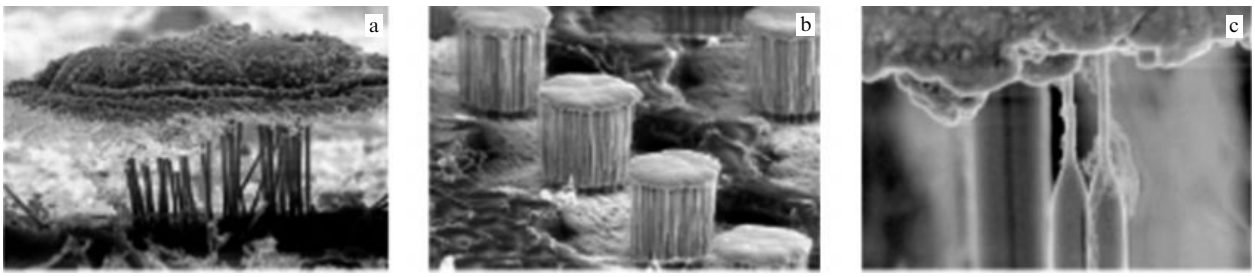

Figure 14. Metallized through-hole vias fabricated by ion track lithography in a metal-clad polyimide foil (Espanex) [341]. (a) Multiple wire via consisting of individual wires. (b) Solid via. (c) Candle-shaped top segment of two individual wires.

means of CCDs or other types of imaging detectors [360]. New types of optical filters were fabricated for the SPIRIT telescopes aboard the Coronas-F satellite to investigate the Sun with a high spatial resolution in the 17.1–30.4 nm spectral range [360].

Replica techniques allow extending track-etch technology to the production of convex (protruding) structures with a large specific surface area [361]. Moreover, metallic replicas of polymeric foils with arrays of etched tracks have been applied to the process of heat transfer [362, 363].

In recent years, the field-guided transmission of highly charged ions and electrons through track nanocapillaries in insulating materials has been demonstrated [364–368]. The guiding phenomenon implies that highly charged ions preserve their incident charge state during the transmission through the capillaries. When the capillary axis is tilted with respect to the incident beam, the transmission of highly charged ions in insulators was found to occur with negligible electron capture. To understand the guiding phenomena, it was proposed that the incident ions deposit positive charge at the inner wall of the capillaries in a self-organized process [364]. For a tilted foil, the deposited charge in the entrance region increases until the electrostatic field is sufficiently high for a deflection of the ions in the direction of the capillary axis. The discussed phenomenon can be used to develop systems of transformation, control, and transport of charged particle beams; in particular, to obtain micro- and nanosize beams [368].

Using electro-deposition, pores in ion-track membranes can be filled with different metals in order to fabricate wires consisting of multilayers of Co/Cu for studies of the giant magnetoresistance perpendicular to the layer plane [369–371] or Ag/Cu janus nanowires [372] and with semiconductor objects for optical applications [373].

Identification of a market product based on the optical properties of polymer foils containing arrays of etched ion tracks [332, 374] is one of the potential applications of this technique. A track membrane is a unique three-dimensional structure characterized by the number of pores, their diameter, length, position, and tilt angles. Reproduction of such a microstructure using optical, lithographic, mechanical, or xerographic methods is practically impossible. The track pores can be filled with dyes or luminophors, which impart special spectral and luminescent characteristics to the foil [332].

Recently, the authors of Ref. [375], using etched ion tracks, fabricated broadband (400–1700 nm) hard-coated optical absorbers with the spectral reflectance below 2%.

Being effective materials for track formation, plastics are currently widely used in radiobiological dosimetry as detectors of the radioactive gas radon, which is a health hazard [376, 377]. Such detectors are especially effective in monitoring the concentration of radon in living quarters by gathering data with the track technique. The material of the detectors is then chemically etched and the tracks are detected by SEM or conventional optical means. Measuring the emanation of radon from the ground over large areas by the track method allows predicting severe earthquakes [376].

To summarize, ion tracks, especially etched tracks, alone or in combination with lithography and other techniques, open many possibilities for creating novel deep micro- and nanostructures within a range of materials that are difficult or even impossible to produce by other techniques. The first prototypes of a number of ion-track-based devices mentioned above have been created and tested successfully. The industrial realization of these devices still requires much research work, but the proposals are realistic and the realization would be a big step forward in future technologies. The application potential of ion-track-based materials and structures is nevertheless still tremendous.

7. Nanostructuring of solids by SHIs

There are many techniques for creating nanostructures, like vapor phase condensation, thermal codeposition, molecular beam epitaxy, pulsed laser deposition, and various methods related to the use of ion beams. SHI beams are emerging as a powerful technique for the fabrication of different nanostructures and their modification, because it provides remarkable possibilities to control the structures by the energy transferred to the solid almost instantaneously into a highly localized volume of nanometer dimensions.

Surface instabilities in thin films can be triggered by SHIs, and the subsequent self-assembly of the surface can be controlled by fine-tuning the irradiation conditions. Among the key problems of material nanostructuring, control of the size of nanoparticles, the size distribution, creation of specially aligned particles, shape transformation of nanoparticles, and the alignment of nanoparticles in a row like a string of pearls are the more important ones.

One of the most striking examples of the ion-hammering effect of amorphous materials, which was discussed in Ref. [1], is the deformation of single colloidal particles under SHI irradiation [378–387]. This SHI beam deformation technique provides a unique method to tailor the structure, shape, size, and size distribution of colloidal particles and aggregates. Metallic and semiconductor nanoparticles (NPs) exhibit novel size-dependent structural, electronic, magnetic, and optical properties in comparison to their bulk counterparts, including ultra-fast optical response and a strong electric field

enhancement by the surface plasmon resonance, single electron transport, super-paramagnetism, and the finite-size effect ([388] and the references therein). Such a difference in properties stems from the nonnegligible influence of surface atoms and quantum confinement of charge carriers.

While this phenomenon has been extensively studied by many groups [378–387] since its discovery, its mechanism has not yet been clarified. It was suggested in [389] that the SiO_2 matrix plays an important role in the elongation of metal NPs; the elongation was ascribed to the in-plane stress induced by the ion-hammering effect (and radiation-induced softening of the NPs). Later, this mechanism was criticized because the ion-hammering energy threshold was different from the elongation threshold [383]. In [382], the observed elongation was shown to be too large to be explained by the hammering effect alone, even taking the radiation-induced softening of NPs into account. Moreover, the melting of NPs by the thermal spike effect has been discussed by many groups. Unlike embedded NPs, free-standing Ag and Au NPs showed no deformation under SHI irradiation, indicating that the deformation process necessitates the presence of an SiO_2 matrix [389, 390].

The elongation strongly depends on many parameters, such as the thickness of the SiO_2 covering layer, ion energy, and ion beam fluence [387].

As in the case of amorphous materials with metallic conductivity, the elongation process is clearly cumulative requiring fluences greater than 10^{13} cm^{-2} (or equivalently hundreds of overlapping impacts) for an ion track 10 nm in diameter [387]. Several authors have reported a lower limit on particle size of 5–7 nm (in the case of gold particles embedded in silica) required for the deformation to occur [391–393]. Upon irradiation, NPs with a below-threshold diameter remain spherical in shape and progressively decrease in size due to dissolution [387]. One study [392] found that particles larger than 50 nm do not deform, either. The saturation width of deformed nanoclusters and nanorods is linked to the diameter of the ion track [385, 391].

Gold NPs with a size distribution between 2 and 12 nm, embedded in crystalline AlAs, which highly resists amorphization were subjected to SHI irradiation in [385]. Deformation was induced by 30 MeV Cu^{5+} ions at liquid nitrogen temperature. In spite of some crystal damage, the AlAs samples remained crystalline after irradiation, and spherical Au NPs where observed with no indication of elongation. It was suggested that the particle deformation is a consequence of compressive stresses generated during the hammering deformation of the amorphous matrix surrounding these NPs [385].

Much attention is paid to Co NP deformation by SHIs due to their size, shape, and crystallographic-dependent magnetic properties important for applications in biomedicine and magnetic storage technology [13–15, 381, 387]. Nonspherical Co nanorods exhibit unique perpendicular magnetic anisotropy, remanence, and coercive force that are heavily dependent on the large nanorod diameter [394].

SHI irradiation of metallic nanocrystals (NCs) in SiO_2 leads to a shape transformation characterized by elongation along the direction of irradiation, as demonstrated for Co [381, 387, 388], Au [383, 395–398], Ag [399–401], and Pt [384, 402] NCs. The NC size, shape, and size distribution are fluence dependent (Fig. 15). The thermal spike model, which predicts the formation of a molten track around the ion path, is one plausible explanation for elongation of metallic NCs

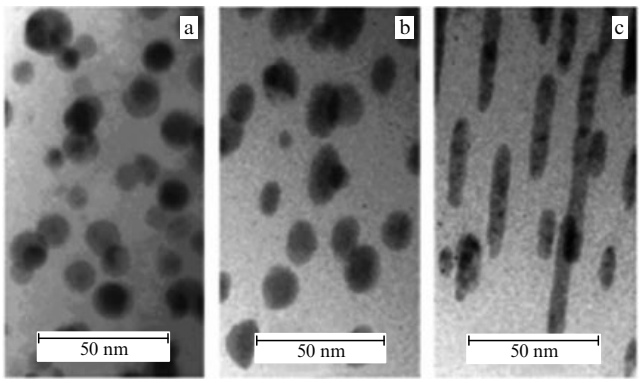

Figure 15. TEM micrographs of Pt NC samples before and after SHI irradiation at different fluences, as indicated in each panel: (a) nonirradiated, (b) 2×10^{13} cm^{-2}, and (c) 2×10^{14} cm^{-2}. The mean NC diameter prior to irradiation was ~ 13 nm.

embedded in an amorphous matrix [399, 403]. We note that one of the most widely accepted mechanisms is the interplay of the hammering effect of the SiO_2 matrix and the melting of NPs by the thermal spike effect. Several studies indicate that there is a correlation between elongation and the SHI track diameter. Moreover, the diameter of the molten track in silica confines irradiation-induced NP deformation. Irradiation of Pt NCs with the mean diameter 7 nm by 185 MeV Au ions in the fluence range $2 \times 10^{12} - 6 \times 10^{14}$ cm^{-2} leads to their elongation by more than 10 times [404]. According to observations, NPs that are less than 7 nm in size are not elongated at all, and their size decreases with increasing the fluence, until the complete dissolution of the NPs. The Pt NCs greater than 7 nm in diameter change their shape from a sphere (in the absence of irradiation) to an elongated spheroid (2×10^{13} cm^{-2}) and eventually take the shape of nanowires ($\sim 10^{14}$ cm^{-2}) with a diameter close to 7 nm. If the particle size is smaller than or comparable to the track diameter in SiO_2, there is isotropic growth or reduction in particle size due to dissolution [387, 405], because the NP is surrounded by transiently molten silica. The NPs above a certain size ($> 40-50$ nm) do not undergo shape transformation [405–407]. Metal NPs above this diameter behave like bulk material for SHI irradiation. The lower-size threshold is dependent on the temperature of irradiation [385]. Hence, the saturation width of deformed nanoclusters and nanorods is linked to the diameter of the ion track [385, 391].

The volume expansion of the NP material in the transformation from the solid to the molten state can also play an important role in NP deformation. For example, the volume expansion of Au particles under melting is more than that for silica under similar transformation. Therefore, the elongation of Au NPs along an ion track is expected [406].

Very recently, gold NPs embedded in a silica matrix have been irradiated with 2–40 MeV Cu or Si ions at fluences ranging from 1×10^{13} to 4×10^{15} ion cm^{-2}, and their deformation from spheres to prolate ellipsoids was studied [397]. Large gold NPs are more elongated than small ones, which indicates that for small particles, the ion-induced deformation competes with surface tension effects. The observed deformation exhibits a threshold value of (1.9 ± 1.3) keV nm^{-1} [397], which is the same as that for the deformation of silica, and likely related to the threshold for melting of silica along the ion track. The estimated diameter

of ion tracks ranged from 0.17 to 1.4 nm for the above-mentioned ions and their energies. Moreover, a mechanism of deformation whereby the ion irradiation first deforms the silica, which exerts a compressive stress on the NPs in a plane perpendicular to the ion beam (which can be relieved when an ion passes through a nanoparticle and melts it along the ion track), is discussed in Ref. [397].

SHI irradiation can also play the role of a size filter to NPs embedded in silica. Dissolution of Ag NPs smaller than ~ 2.0 nm was observed in silica irradiated with 73 MeV Ca ions [401]. The surviving Ag NPs show that the size dispersion of Ag NPs is reduced compared with that before irradiation [401]. There is an elongation threshold size ~ 6.5 nm for cobalt NPs irradiated with 89 MeV Au ions [387]. The NPs larger than this threshold diameter elongate with ion fluence, and the transverse size of NPs eventually saturates at approximately the same value as the shape transformation threshold. NPs below the threshold size remained spherical and progressively dissolved in the matrix with increasing fluence [387].

The results in Ref. [400] reveal that the processes of alignment, dissolution, growth, and elongation of embedded NPs (silver NPs in silica irradiated with 120 MeV Ag ions) depend on the volume fraction of metal in the matrices and the dipolar interactions among such NPs.

The shape transformation from spherical to rod-like occurs in Sn NPs embedded in a silica matrix under SHI irradiation [408, 409]. It has also been observed that 80 MeV oxygen ions could modify CdS NPs into elongated structures, such as nanoneedles and nanorods [410]. 210 MeV Xe irradiation from FePt nanoparticles with a diameter of 2 nm, embedded in alumina, causes the elongation of NPs, with the particle centers being enriched with Pt [411]. Contrary to the findings for metallic NPs, it has been revealed that Ge NPs were flattened into an oblate form, when 38 MeV I^{7+} ions were used to irradiate 26 nm Ge NPs [412]. Irradiation with low fluences (10^{14} ion cm^{-2}) transforms medium-size Ge nanospheres into disks, whereas smaller ones become rod-like and larger ones do not change. At higher fluences, the larger Ge nanospheres also transform into disks [412]. The observation of Ge NPs flattening is not consistent with the discussed mechanism that the elongation is caused by the flow of liquid material into the low-density core of the ion track. Elongation of high-melting-point (MP) NPs (vanadium, $T_{MP}^{bulk} = 1890\,^{\circ}C$) and low-MP NPs (zinc, $T_{MP}^{bulk} = 420\,^{\circ}C$) in silica was examined under irradiation with 200 MeV Xe^{14+} ions [386]. Irrespective of the large difference in their MPs, both V and Zn NPs showed comparable elongation. The insensitivity of elongation to the MPs of the NPs was explained by the asynchronicity of the melting process of the silica and the NPs [386].

Recently, ZnO NPs embedded in SiO_2 have been irradiated with 200 MeV Xe^{14+} ions up to 5.0×10^{13} ion cm^{-2} [413]. An elongated morphology of the NPs was observed. Furthermore, the elongated NPs were not ZnO but metallic Zn. The SHI irradiation induced deoxidation of ZnO NPs to Zn NPs by the thermal spike effect enhanced by the small-size geometry of the NPs embedded in thermally insulating silica [279]. A configuration of small particles separated by SiO_2, an excellent heat insulator (the heat conductivity of silica is 0.014 W cm^{-1} K^{-1}, i.e., ~ 100 times smaller than that of ZnO), is essential to increase the temperature and induce the deoxidation reaction. Finally, shape elongation occurs in deoxidized Zn NPs.

Silicon nanocrystallites 2–3 nm in diameter were fabricated in SiO_2 in the tracks as a result of irradiation of α-SiO by ions of Ni and Pb [414]. This system is of great interest from the standpoint of applications. This method allows creating quantum dots and wires and controlling the optical properties of materials.

Group-IV semiconductor (Si and Ge) NCs have attracted a great amount of attention because of their excellent optical and electronic properties, which can be utilized for applications in optoelectronic devices [415]. Moreover, there has been much interest in the suboxide thin films of SiO_x [416–418] and GeO_x [419, 420] because they can be used as precursors for the formation of their respective nanocrystallites [416, 419, 420]. Suboxides have a strong tendency to separate into two phases, semiconductor and oxide. SHI irradiation is an important tool for engineering materials in a controlled fashion [420, 421].

In Ref. [418], the distorted lattice phase of silicon after the SHI irradiation of SiO_x thin films was reported. The occurrence of a high-pressure phase of silicon NCs is explained on the basis of an ion-beam-induced pressure pulse.

Furthermore, SHI irradiation of In_xO_y films initiated the formation of In NCs [422]. The films irradiated with 120 MeV Ag ions show a phase separation of the In- and In_2O_3-containing nanometric crystallites 35 to 45 nm size. In all these experiments with suboxides of Si, Ge, and In, oxygen-rich regions in the material become more oxygen rich, and oxygen-poor regions become more oxygen poor during a temperature spike. Of course, the phenomenon of phase separation in suboxides is observed as a result of different activation processes, such as furnace thermal annealing, rapid thermal annealing, Ar-plasma treatment, UV laser irradiation, and white synchrotron radiation (see [418] and the references therein).

Relaxation of high-energy electron excitations generated by SHI causes the formation of nanosize precipitates in metals [423] and insulators [424] supersaturated with impurity atoms. Precipitation can occur when the temperature in the track reaches values at which the nucleation time becomes shorter than the track cooling time [425]. The GeAs NC precipitations are observed in $Si_{1-x}Ge_x$ alloy layers irradiated with U^{238} ions with an energy of 0.8–2.7 GeV and supersaturated with As atoms [164].

The authors of Ref. [407] noted that in performing the SHI irradiation of perfect oxides such as SiO_2, GeO_2, and In_2O_3, the formation of NPs does not take place. Contrary to this standpoint, Kachurin et al. [17] observed the formation of light-emitting Si-enriched nanostructures in stoichiometric SiO_2 layers irradiated with 167 MeV Xe ions and 700 MeV Bi ions in the respective fluence ranges $10^{12}-10^{14}$ cm^{-2} and $3 \times 10^{12}-1 \times 10^{13}$ cm^{-2}. The electron energy losses of the ions are regarded as responsible for the disproportionality of SiO_2 and nanostructure formation inside the tracks. From the fluence dependences of the photoluminescence (PL) intensity, the track diameters for Xe and Bi ions were respectively assessed as < 3 nm and ~ 10 nm. A shift of the PL bands induced by Xe and Bi ions agrees with the predictions of the quantum confinement effect for Si NPs [17].

Modifications of Si nanocrystals embedded in an SiO_2 matrix by SHI irradiation were reported in [426]. The response of *in situ*-formed Si nanostructures embedded in an Si-rich hydrogenated amorphous silicon nitride matrix to 100-MeV Ni^{8+} ions irradiation was studied in Ref. [16].

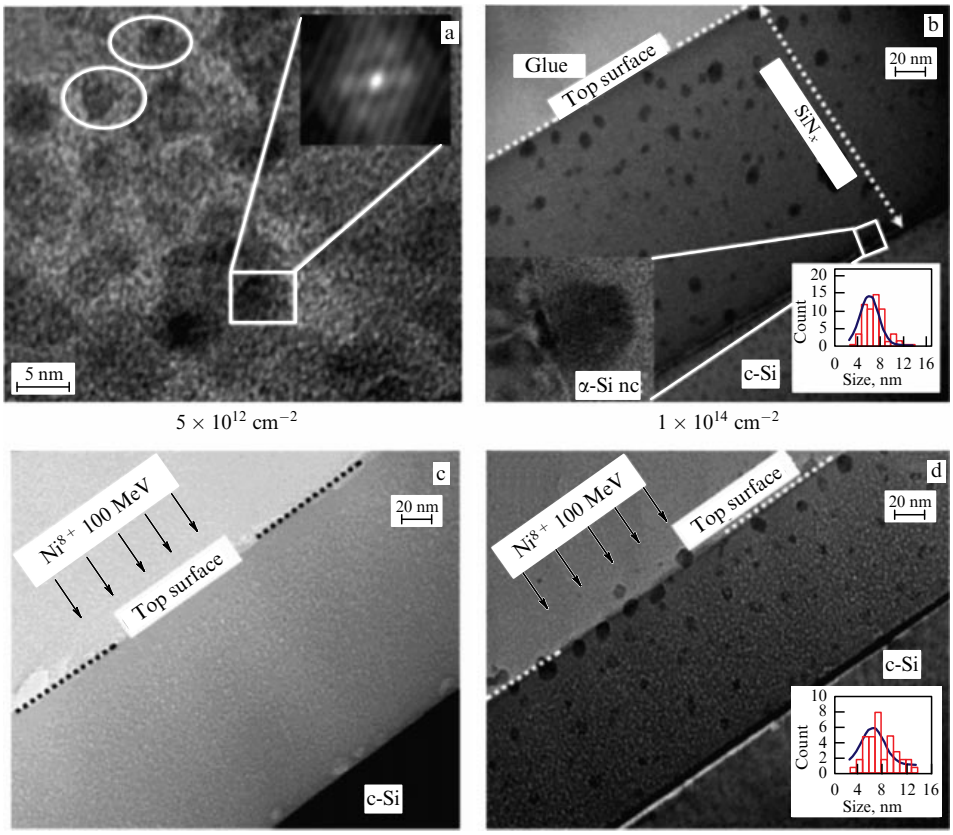

Figure 16. (a) HRTEM image of ASD SRSN sample showing *in situ*-formed Si nanostructures (as dark spots) in an SRSN matrix; the inset shows an autocorrelation image of the lattice plane of the crystalline Si-nanostructure. (b–d) XTEM images of nonirradiated and irradiated samples. The insets at the bottom right in (b) and (d) show the size distribution of Si nanostructures [16].

Irradiation with a fluence of 5×10^{12} ion cm^{-2} led to dissolution of Si nanostructures. Nevertheless, irradiation with a higher fluence of 1×10^{14} ion cm^{-2} enhances the nucleation and leads to the formation of amorphous Si-nanostructures in the film (Fig. 16). The results are explained on the basis of intense hydrogen desorption induced by electronic energy loss and the consequent rearrangement of the amorphous network under the thermal spike in the track.

In Ref. [427], 400 keV Ge^+ ions were implanted into SiO_2 films at a fluence of 3×10^{16} ion cm^{-2}. Then the implanted samples were irradiated with 150 MeV Ag^{12+} ions with various fluences. The diffusion of Ge atoms in the track regions resulted in nucleation leading to the formation of Ge nanocrystals. The size of these nanocrystals increases with an increase in the ion fluence, which means that the size and properties in Ge nanocrystals can be tuned by choosing the appropriate ion energy and fluence.

Very recently [428], Ge NCs embedded in SiO_2 were synthesized by rapid thermal annealing of composite thin films of Ge and SiO_2 deposited on Si by the RF magnetron cosputtering method. The Ge NCs were then irradiated by 120 MeV Ag and 80 MeV Ni ions at various fluences ($10^{13} - 10^{14}$ ion cm^{-2}). The influence of energy loss and fluence on the modification of Ge NCs was studied. It was observed that with an increase in fluence, the NC sizes reduce and partial amorphization of the embedded NCs occurs. The initial size of NCs plays an important role in the modification of Ge NCs by SHIs [428]. As presented in Ref. [423], the critical diameter of the embedded spherical Ge NCs to be melted is described by the expression

$$R_{\mathrm{Np}}^{\max} = \sqrt{\frac{3(\mathrm{d}E/\mathrm{d}x)_{\mathrm{e}}}{2\pi H_{\mathrm{Np}}^{\mathrm{melt}} \rho_{\mathrm{Np}}}}, \tag{7.1}$$

where R_{Np} is the radius of NPs, $H_{\mathrm{Np}}^{\mathrm{melt}}$ is the melting heat of the stopping matter (436 J g^{-1} for Ge), $(\mathrm{d}E/\mathrm{d}x)_{\mathrm{e}}$ is the electronic energy loss of incident ions, and ρ_{Np} is the density of NPs (5.32 g cm^{-3}) for bulk Ge. Therefore, for a given S_{e}, a spherical NP melts when Eqn (7.1) is satisfied. Hence, the size reduction and the appearance of more NPs of smaller sizes observed in Ref. [428] are in accordance with Eqn (7.1). The estimated critical diameters of the Ge NCs are 48 nm and 38 nm for 120 MeV Ag and 80 MeV Ni ion irradiation, respectively. Because the average sizes of Ge NCs in the nonirradiated samples were 31 nm (set A) and 40 nm (set B), these NCs would melt under SHI irradiation [426].

In our study [429], InAs nanoclusters were synthesized in Si wafers or 0.6 μm SiO_2 layers on Si by high-fluence ion implantation followed by furnace annealing and 167 MeV Xe ion irradiation (3×10^{14} ion cm^{-2}). The respective average size of InAs nanoclusters before the SHI irradiation amounted to 10 nm and 6 nm in the above-mentioned structures. The Xe ion irradiation stimulated an increase in the nanocluster sizes for both unannealed and pre-annealed silicon samples. The crystalline nature of the precipitates was proved by the presence of Moiré contrast in TEM images. In the 0.6 μm SiO_2/Si system irradiated by Xe ions, the ordering of nanoclusters was observed along the direction of the incident ion beam. Some of the nanoclusters changed their

shape from spherical to elliptical with the greater axis perpendicular to the sample surface [429].

Recently, the effects of 150 MeV Au ion irradiation (10^{13} to 10^{14} ion cm^{-2}) on Si NPs with a size in the range of a few nm to 80 nm synthesized by picosecond laser ablation of Si wafers in aceton were investigated in [430]. With an increase in fluence, it was observed that the average particle size was reduced on the whole and the growth of 6–9-nm NPs in the surroundings of bigger NPs was revealed. As a result of ion irradiation, the Si NPs were amorphized at higher fluences.

Examples of SHI irradiation effects in metallic and nonmetallic NPs, including partial amorphization of Bi NPs [431], the fcc-to-hcp phase transition in Co NPs [432], the amorphization and crystallization of SnO_2 NPs [12], as well as other transformations were discussed in detail in review papers [406, 407, 433].

However, further work is needed to prove the underlying mechanisms responsible for NC transformation and to explain the sometimes conflicting results reported thus far [383, 399].

The grain growth in SnO_2 films, caused by 120 MeV Ag ion irradiation, was observed up to the fluence of 1×10^{12} ion cm^{-2} with the roughness ranging from 9.4 to 14.9 nm, followed by a reduction in the grain size and roughness [12]. Such a change in surface morphology can play a significant role in gas sensing applications of this material and hence in the tuning of sensor characteristics.

SHI beams can induce magnetization in $ZnFe_2O_4$ spinel and Fe_3O_4 nanoparticle thin films because of a site exchange of Zn and Fe atoms leading to a new magnetic phase [434], due to induced enhanced magnetic anisotropy [435], or by the creation of an amorphous phase along the ion track in YCo_2 [436].

Fe films on c-silicon irradiated with 100 MeV Fe^{7+} ions at a fluence of 10^{14} ion cm^{-2} show a large increase in magnetoresistance, up to 2400% [437]. The results are explained by considering the formation of a nanogranular magnetic silicide phase (of Fe_5Si_3) due to intermixing at the interface.

Irradiation of high-T_c superconducting materials leads to insulating amorphous tracks [438]. Because the track size is of the same order as the coherence length of the superconductor, such columnar defects are very suitable to pin magnetic flux lines [495], leading to an increase in the critical current by more than an order of magnitude.

The gas sensing property of SnO_2 thin films improves with SHI irradiation [440]. After the 75 MeV Ni ion irradiation, the sensitivity of SnO_2 to ammonia increases by 213%. Such an enhancement of ammonia sensitivity was explained in terms of the surface chemistry modification due to SHI irradiation [440].

A single energetic ion can release enough charge in a critical circuit node to flip the logic state of a static random access memory (SRAM) cell, leading to a so-called single-event upset, or to trigger a potentially destructive single-event latch-up in a pair of parasitic bipolar junction transistors present in complementary metal oxide silicon technologies [441]. Indeed, the lateral dimensions of the track of an ion with an energy of several MeV a.m.u.$^{-1}$ become comparable to or even larger than the feature sizes of contemporary 24–45 nm technologies. In the space environment, single-event effects are essentially due to SHIs. MOS devices are extensively used in different radiation-rich environments like space and high-energy physics experiments such as the Large Hadron Collider. The effect of SHIs on semiconductor devices is studied by the use of energetic ion beams, as well as by simulation of the time and space evolution of ion tracks in such structures [51, 442, 443].

SHI irradiation increases the antioxidant activity and biocompatibility of polyaniline (PANI) nanofibers [444]. To improve their antioxidant activity, PANI nanofibers were preliminarily doped with hydrochloric acid (HCl) or camphor sulfonic acid (CSA), and then irradiated with 90 MeV O ions. The enhancement of antioxidant activity of nanofibers is due to the reduction in their size (from 40 nm to 10 nm for HCl-doped nanofibers and from 50 nm to 15 nm for CSA-doped nanofibers), which increases their surface-to-volume ratio [444]. *In situ* studies of biological processes induced in biological cells by SHIs are creating great interest [254, 407, 445]. The risks of human space travel to Mars related to the exposure to space radiation can be simulated by accelerator tests using a plethora of biological assays irradiated by SHIs [446].

Recently, SHIs with energy higher than 1 MeV a.m.u.$^{-1}$ were used to irradiate optical materials and achieve refractive index changes of certain regions [447–451]. SHIs are used efficiently to produce optical wavequides in photonic materials such as potassium sodium strontium barium niobate (KNSBN) [447] and lithium tantalate ($LiTaO_3$) [448], $Bi_4Ge_3O_{12}$ [449], Nd:YVO_4 [450], and LGS [451]. Photonic devices based on the photorefractive effect attract great attention because of their potential application in holographic storage, optical computing, and optical communications [452]. After irradiation of a KNSBN crystal with SHIs, near-surface regions of the crystal (Fig. 17) have a positive extraordinary refractive index change [447]. This change is attributed to partial amorphization of the lattice by electronic damage. Such a waveguide can support several guide modes without the tunneling effect, which is mainly due to the thick index-increasing region created by SHI irradiation. The propagation loss in this waveguide did not exceed ~ 0.8 dB cm^{-1} at 633 nm and 0.72 dB cm^{-1} at 1064 nm [447].

The experimental design of NP assemblies consisting of superstructures in a chosen host is of considerable interest for a great variety of future functional applications in optical [453], magnetic [454], or nanoelectronics devices [254, 455], for example. However, these unique nanomaterial properties are largely governed by the specific size on the nanoscale, shapes, and configurations of the clusters distributed in a suitable matrix. As an example, heavy-ion beam irradiation was shown to be a powerful technique to produce ion-fluence-dependent growth of nanosize cylindrical structures in the form of SiC wires in the Si backbone polymer PMPySi (Polymethylphenylsilane) [456].

Distinct NP self-organization in the nanocomposites (~ 100 nm) of Teflon AF containing different metallic clusters is reported in Ref. [457] upon SHI irradiation of 120 MeV Au beams at different ion fluences ranging from 1×10^{11} to 3×10^{12} cm^{-2} (Fig. 18). Two-dimensional uniformly distributed Au clusters are found to be transformed into long cluster chains of an apparently helical pattern in this matrix, resembling pearls on a string. In contrast, Ag nanoparticles (Fig. 5 in Ref. [457]) were found to concentrate in the formed network of quasi-1D carbonaceous zones upon a high-energy ion impact. Carbon-enriched zones induced and modified by intense electron excitations act as trapping centers for diluted Ag clusters.

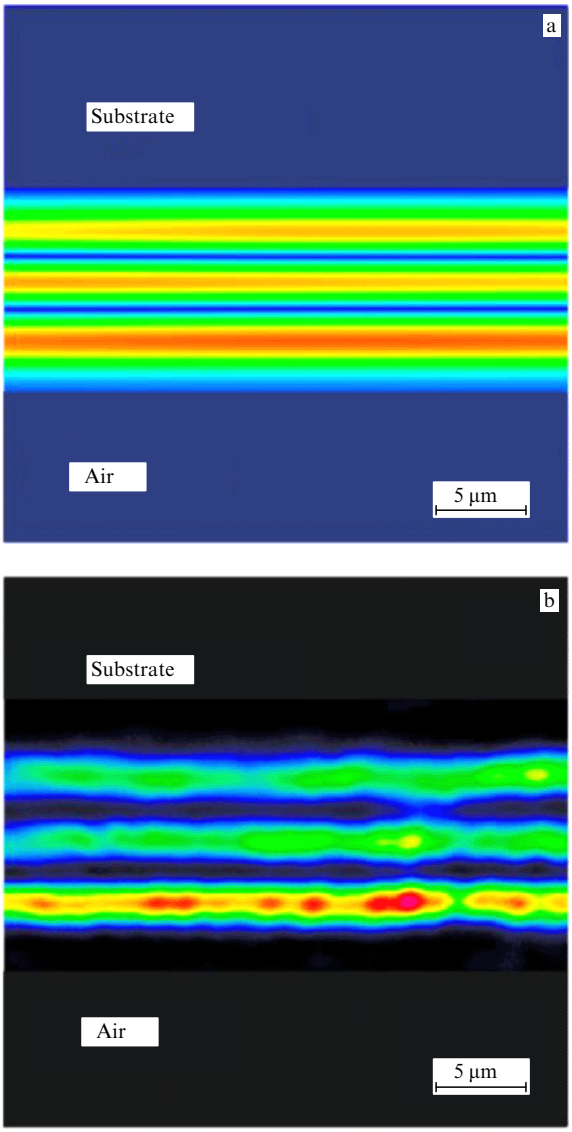

Figure 17. (a) Simulated and (b) experimental near-field modal profiles (TE2) of the 17 MeV C^{5+} ion-irradiated KNSBN waveguide [447].

8. Conclusions

Analysis of the processes accompanying the penetration of high-energy ions through solids suggests that intense electron excitations play an important role in generating structural defects in intense inelastic sputtering of materials and in the initiation of a number of specific effects, such as track formation, local melting, amorphization, and the production of high-pressure phases, fullerenes, and carbon nanotubes.

The possible mechanisms of track formation are still being discussed. However, the large volume of contemporary experimental data suggests that in many insulators, some semiconductors, and dispersed materials with metallic conduction, the processes of the formation of melted regions followed by their rapid solidification are the reason for the structural and phase changes recorded in irradiated materials. For materials such as alkali-halide crystals, the most proper model today is the excitonic model [176, 177]. Experimental data obtained in complex metal oxides [181] under irradiation with SHIs can be considered a possible manifestation of the collapse of solitons with the formation of intrinsic nano- and mesodefects.

The multiscale simulations discussed in this review can provide a proper description of the spatio-temporal evolution in track formation and deeper insights into the internal structure of damaged regions.

Atomistic models of hot dense matter are currently being developed to overcome the limitations of the existing models [458, 459]. A two-temperature atomistic model has been developed with an interionic potential depending on the electronic temperature and the pressure of delocalized electrons [458]. This model describes the ion subsystem within classical molecular dynamics, whereas the electron subsystem is treated in the continuum framework.

As was discussed above and in Ref. [1], depending on the type of metal and its structural state, the transfer of a large amount of energy into the electron subsystem can lead both to the annealing of previously produced and genetic structural defects and to the high effectiveness of defect formation, which is greater than the effectiveness of nuclear stopping processes by a factor of 20 or more. Some metals exhibit track-like formation of defective condensates, which accu-

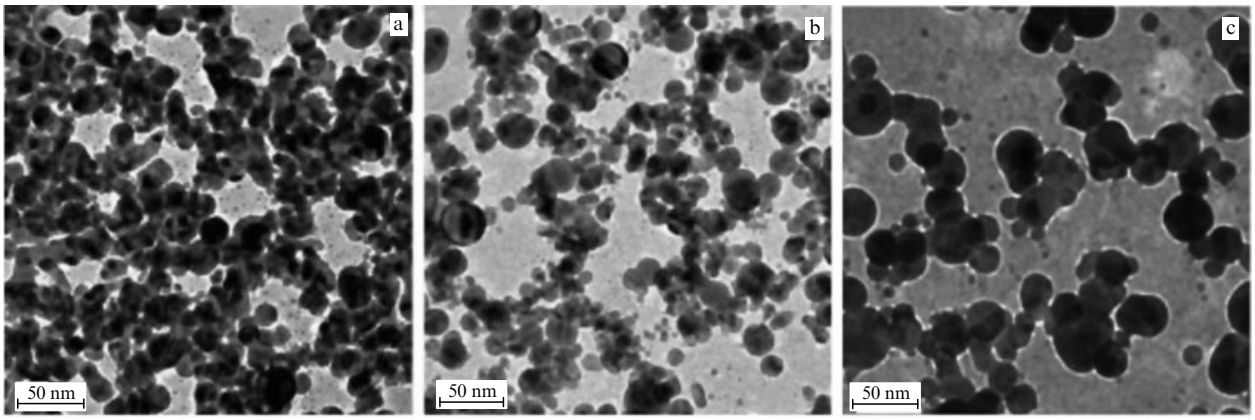

Figure 18. TEM images of a nanocomposite irradiated by 120 MeV Au beams at various fluences. (a) Emergence of long Au cluster chains at the lowest fluence of 1×10^{11} ion cm^{-2}. (b) Increasing the fluence to 5×10^{11} ion cm^{-2} witnesses apparently cooperative Au cluster motion in the form of relatively isolated long seemingly helical chains with an average width of 15 nm. (c) Sample irradiated at the chosen highest fluence of 3×10^{12} ion cm^{-2} shows transformation of long helical cluster chains into a staircase type of arrangement [457].

mulate in the cylindrical region along the ion path, as well as phase transformations [460].

The manifestation of track formation, the phase composition of the tracks, and the track morphology depend on a number of important factors:

— the electronic properties of the irradiated material (metal, semiconductor or insulator; the band gap and the electron–phonon relaxation time);

— the structural state of the target (single crystal, amorphous material, polycrystalline material, grain size; the presence and type of structural defects, boundaries, and impurities), which determines the electron–phonon relaxation time, the temperature near the ion path, and the possibility and rate of epitaxial recrystallization;

— the compositional and structural complexity of the irradiated material, which also determines the rate of epitaxial recrystallization of local regions; and

— the initial spatial distribution of the energy imparted to the electron subsystem and the energy spectrum of the electron excitations, which determine the temperature of a local region at the stage in which the excited region is thermalized. For instance, for equal values of $(\mathrm{d}E/\mathrm{d}x)_e$, the ion with a higher velocity generates a larger radial distribution of the energy imparted to the electrons of the stopping medium, which results in a smaller track radius. Excitations with the highest density correspond to the case where materials are irradiated by cluster ions (e.g., fullerene ions).

The process of forming latent tracks accompanied by brief chemical etching is widely used in practice to manufacture filters (based on polymer materials with pores whose dimensions are in the micrometer, submicrometer, and nanometer ranges) for the chemical, medical, and biological industries, and to fabricate metal or semiconductor nanowires in polymers and other materials, magnetic multilayer nanowires, and highly sensitive sensors.

Bearing in mind that the diameter of each track typically ranges from 1 to 10 nm, we can estimate the number of tracks within one square centimeter of the surface as 10^{12}. Thus, the packing density of elements in such a system of nanoelectronics can be as high as 10^{12} elements to each square centimeter, i.e., the density is 10^3 higher than the value that can be achieved today. The possibility of electron tunneling through the walls of neighboring isolating channels makes it possible to create new classes of nanoelectronic devices. The unique optical, photoelectric, and conducting properties of tracks can lead to a new generation of electronic and optoelectronic nanosize devices.

The processes of formation of continuous and discontinuous tracks in materials with supersaturated solid solutions are of interest if we want to fabricate ordered systems of quantum wires and chains of quantum dots. Here, ordinary ion implantation can be used to achieve supersaturation within impurities.

The specific structure of the track regions makes it possible to predict that in the 21st century they will be widely used in other industries and areas of human endeavor.

The author expresses his sincere thanks to Yulia Dziraeva for her help in preparing this paper.

References

1. Komarov F F *Phys. Usp.* **46** 1253 (2003); *Usp. Fiz. Nauk* **173** 1287 (2003)
2. Silk E C H, Barnes R S *Philos. Mag.* **4** 970 (1959)
3. Fleischer R L, Price P B, Walker R M *Nuclear Tracks in Solids: Principles and Applications* (Berkeley, Calif.: Univ. of California Press, 1975)
4. Apel P Y, Fink D, in *Transport Processes in Ion-Irradiated Polymers* (Ed. D Fink) (Berlin: Springer, 2004)
5. Ozin G A *Adv. Mater.* **4** 612 (1992)
6. Chakarvarti S K, Vetter J *Radiat. Meas.* **29** 149 (1998)
7. Wang X, Fujimaki M, Awazu K *Opt. Express* **13** 1486 (2005)
8. Schulz U et al. *Opt. Express* **15** 13108 (2007)
9. Vieillard J et al. *Microelectron. Eng.* **85** 465 (2008)
10. Jayalakshmi G et al. *Vacuum* **95** 66 (2013)
11. Kumar Y et al. *Mater. Sci. Eng. B* **177** 1476 (2012)
12. Abhirami K M et al. *Vacuum* **90** 39 (2013)
13. D'Orléans C et al. *Phys. Rev. B* **67** 220101(R) (2003)
14. Singh F et al. *Nucl. Instrum. Meth. Phys. Res. B* **267** 936 (2009)
15. Avasthi D K et al. *Nucl. Instrum. Meth. Phys. Res. B* **268** 3027 (2010)
16. Singh S P et al. *Nucl. Instrum. Meth. Phys. Res. B* **276** 51 (2012)
17. Kachurin G A et al. *Nucl. Instrum. Meth. Phys. Res. B* **282** 68 (2012)
18. Kumakhov M A, Komarov F F *Energy Loss and Ion Ranges in Solids* (New York: Gordon and Breach Sci. Publ., 1981)
19. Miterev A M *Phys. Usp.* **45** 1019 (2002); *Usp. Fiz. Nauk* **172** 1131 (2002)
20. Fain J, Monnin M, Montret M *Radiat. Res.* **57** 379 (1974)
21. Chatterjee A, Schaefer H J *Rad. Environ. Biophys.* **13** 215 (1976)
22. Akkerman A, Barak J, Emfietzoglou D *Nucl. Instrum. Meth. Phys. Res. B* **227** 319 (2005)
23. Kalinichenko A I, Strel'nitsky V E *Radiatsionno-Akusticheskie Effekty v Tverdykh Telakh* (Radiation-Acoustic Effects in Solids) (Kharkov: National Science Center Kharkov Institute of Physics and Technology, 2013)
24. Kaplan I G, Miterev A M *Dokl. Akad. Nauk SSSR* **280** 127 (1985)
25. Magee J Z, Chatterjee A *J. Phys. Chem.* **84** 3529 (1980)
26. Mozumder A *J. Chem. Phys.* **60** 1145 (1974)
27. Waligorski M R P, Hamm R N, Katz R *Nucl. Tracks Radiat. Meas.* **11** 309 (1986)
28. Lee E H *Nucl. Instrum. Meth. Phys. Res. B* **151** 29 (1999)
29. Miterev A M *High Energy Chem.* **31** 173 (1997); *Khim. Vysok. Energ.* **31** 197 (1997)
30. Bethe H A *Ann. Physik* **5** 325 (1930)
31. Bethe H A *Rev. Mod. Phys.* **22** 213 (1950)
32. Bloch F *Ann. Physik* **16** 285 (1933)
33. Barkas W H *Nuclear Research Emulsions* Vol. 1 (New York: Academic Press, 1963)
34. Schiwietz G, Grande P L *Nucl. Instrum. Meth. Phys. Res. B* **175–177** 125 (2001)
35. Akkerman A, Murat M, Barak J *Nucl. Instrum. Meth. Phys. Res. B* **269** 1630 (2011)
36. Ziegler J F, Ziegler M D, Biersack J P *Nucl. Instrum. Meth. Phys. Res. B* **268** 1818 (2010)
37. Sigmund P, Schinner A, Paul H "Errata and addenda for ICRU Report 73, Stopping of ions heavier than Helium" *J. ICRU* **5** (1) (2005)
38. Grande P L, Schiwietz G *Nucl. Instrum. Meth. Phys. Res. B* **267** 859 (2009)
39. Physics Reference Manual, Version: Geant4 9.5.0, 2nd, December (2011)
40. Bradt H L, Peters B *Phys. Rev.* **74** 1828 (1948)
41. Gryziński M *Phys. Rev.* **138** A322 (1965)
42. Garcia J D *Phys. Rev.* **177** 223 (1969)
43. Kaganovich I D, Startsev E, Davidson R C *New J. Phys.* **8** 278 (2006)
44. Khandelwal G S, Choi B-H, Merzbacher E *Atom. Data* **1** 103 (1969)
45. Choi B-H, Merzbacher E, Khandelwal G S *Atom. Data* **5** 291 (1973)
46. Ritchie R H *Phys. Rev.* **114** 644 (1959)
47. Tung C J et al., Report ORNL/TM-5188 (Oak Ridge, TN: Oak Ridge Natl. Lab., 1976)
48. Akkerman A et al. *Phys. Status Solidi B* **198** 769 (1996)
49. Slater J C *Phys. Rev.* **36** 57 (1930)
50. Khandelwal G S, Merzbacher E *Phys. Rev.* **151** 12 (1966)
51. Colladant T et al. *Nucl. Instrum. Meth. Phys. Res. B* **245** 464 (2006)
52. Kaliman Z et al. *Phys. Rev. A* **65** 012708 (2001)
53. Baranov A A et al. *Nucl. Instrum. Meth. Phys. Res. B* **286** 51 (2012)

54. Kuhr J-C, Fitting H-J J *Electron Spectrosc. Relat. Phenom.* **105** 257 (1999)
55. Rymzhanov R A, Medvedev N A, Volkov A E *Nucl. Instrum. Meth. Phys. Res. B* **388** 41 (2016)
56. Pines D *Elementary Excitations in Solids* (New York: W.A. Benjamin, 1963)
57. Rymzhanov R A, Medvedev N A, Volkov A E *Nucl. Instrum. Meth. Phys. Res. B* **326** 238 (2014)
58. Rymzhanov R A, Medvedev N A, Volkov A E *Nucl. Instrum. Meth. Phys. Res. B* **354** 292 (2015)
59. Van Hove L *Phys. Rev.* **95** 249 (1954)
60. Leibfried G *Bestrahlungseffekte in Festkörpern* (Stuttgart: B.G. Teubner, 1965)
61. Akkerman A, Murat M, Barak J *Nucl. Instrum. Meth. Phys. Res. B* **321** 1 (2014)
62. Brandt W, Kitagawa M *Phys. Rev. B* **25** 5631 (1982)
63. Sigmund P, Schinner A *Nucl. Instrum. Meth. Phys. Res. B* **382** 15 (2016)
64. Ritchie G G, Claussen C *Nucl. Instrum. Meth. Phys. Res.* **198** 133 (1982)
65. Klaumünzer S *Matematisk-Fysiske Meddelelser* **52** 293 (2005)
66. Insepov Z, Terasawa M, Takayama K *Phys. Rev. A* **77** 062901 (2008)
67. Johnson R E, Brown W L *Nucl. Instrum. Meth. Phys. Res.* **198** 103 (1982)
68. Leseur D, Dunlop A *Radiat. Eff. Def. Solids* **126** 163 (1993)
69. Schiwietz G et al. *Nucl. Instrum. Meth. Phys. Res. B* **225** 4 (2004)
70. Xiao G et al. *Phys. Rev. Lett.* **79** 1821 (1997)
71. Schiwietz G et al. *Nucl. Instrum. Meth. Phys. Res. B* **175–177** 1 (2001)
72. Sakata M et al. *Nucl. Instrum. Meth. Phys. Res. B* **269** 795 (2011)
73. Schiwietz G et al. *Phys. Rev. Lett.* **69** 628 (1992)
74. Schiwietz G et al. *Europhys. Lett.* **47** 384 (1999)
75. Schiwietz G et al. *Nucl. Instrum. Meth. Phys. Res. B* **193** 705 (2002)
76. Schiwietz G et al. *Nucl. Instrum. Meth. Phys. Res. B* **266** 1287 (2008)
77. Schiwietz G et al. *Nucl. Instrum. Meth. Phys. Res. B* **317** 48 (2013)
78. Onsager L *Phys. Rev.* **54** 554 (1938)
79. Lifshitz E M, Pitaevskii L P *Physical Kinetics* (Oxford: Pergamon Press, 1981); Translated from Russian: *Fizicheskaya Kinetika* (Moscow: Nauka, 1979)
80. Hänsch W, Miura-Mattausch M *J. Appl. Phys.* **60** 650 (1986)
81. Roldan I B et al. *J. Appl. Phys.* **80** 5121 (1996)
82. Grasser T et al. *Proc. IEEE* **91** 251 (2003)
83. Bordelon T J et al. *Solid-State Electron.* **34** 617 (1991)
84. Mizuno H et al. *J. Appl. Phys.* **74** 1100 (1993)
85. Hughes R C *Phys. Rev. Lett.* **30** 1333 (1973)
86. Hughes R C *Phys. Rev. Lett.* **35** 449 (1975)
87. Ramazashvili R R, Rukhadze A A, Silin V P *Sov. Phys. JETP* **16** 939 (1963); *Sov. Phys. JETP* **43** 1323 (1963)
88. Garin B M, Byakov V M *Khim. Vys. Energ.* **22** 195 (1988)
89. Lankin A V et al. *Phys. Rev. E* **79** 036407 (2009)
90. Komarov F F, Novikov A P, Hoang A T *Izv. Akad. Nauk Belorussk. SSR* (5) 81 (1987)
91. Rethfeld B et al. *Phys. Rev. B* **65** 214303 (2002)
92. Osmani O et al. *Phys. Rev. B* **84** 214105 (2011)
93. Gorbunov S A et al. *Nucl. Instrum. Meth. Phys. Res. B* **315** 173 (2013)
94. Kaiser A et al. *Phys. Rev. B* **61** 11437 (2000)
95. Landau L D, Lifshitz E M *Fluid Mechanics* (Oxford: Pergamon Press, 1987); Translated from Russian: *Gidrodinamika* (Moscow: Nauka, 1986)
96. Epifanov G I *Solid State Physics* (Moscow: Mir, 1979); Translated from Russian: *Fizika Tverdogo Tela* (Moscow: Vysshaya Shkola, 1977)
97. Vedenov A A, Gladush G G *Fizicheskie Protsessy pri Lazernoi Obrabotke Materialov* (Physical Processes at Laser Treatment of Materials) (Moscow: Energoatomizdat, 1985)
98. Medvedev N et al. *Nucl. Instrum. Meth. Phys. Res. B* **268** 3160 (2010)
99. Terekhin P N et al. *Nucl. Instrum. Meth. Phys. Res. B* **354** 200 (2015)
100. Medvedev N A, Volkov A E *AIP Conf. Proc.* **999** 238 (2008)
101. Guizard S et al. *Nucl. Instrum. Meth. Phys. Res. B* **116** 43 (1996)
102. Guizard S et al. *J. Phys. Condens. Matter* **8** 1281 (1996)
103. Seidl M et al. *Nucl. Instrum. Meth. Phys. Res. B* **183** 502 (2001)
104. Novichenok L N, Shul'man Z P *Teplofizicheskie Svoistva Polimerov* (Thermophysical Properties of Polymers) (Minsk: Nauka i Tekhnika, 1971)
105. Baranov I A et al. *Sov. Phys. Usp.* **31** 1015 (1988); *Usp. Fiz. Nauk* **156** 477 (1988)
106. Kitayama T et al. *Nucl. Instrum. Meth. Phys. Res. B* **354** 183 (2015)
107. Komarov F et al. *Nucl. Instrum. Meth. Phys. Res. B* **360** 150 (2015)
108. Kamarou A et al. *Phys. Rev. B* **78** 054111 (2008)
109. Kalinichenko A I et al. *Voprosy Atom. Nauki Tekh. Ser. Fiz. Radiats. Povrezhdenii Radiats. Materialoved.* **92** 131 (2008)
110. Tombrello T A *Nucl. Instrum. Meth. Phys. Res. B* **95** 232 (1995)
111. Stampfli P *Nucl. Instrum. Meth. Phys. Res. B* **107** 138 (1996)
112. Bullough R, Gilman J J *J. Appl. Phys.* **37** 2283 (1966)
113. Klaumünzer S *Nucl. Instrum. Meth. Phys. Res. B* **225** 136 (2004)
114. Surwase S at al. *Nucl. Instrum. Meth. Phys. Res. B* **387** 1 (2016)
115. Young D A *Nucl. Instrum. Meth. Phys. Res. B* **252** 175 (2006)
116. Pakarinen O H, Djurabekova F, Nordlund K *Nucl. Instrum. Meth. Phys. Res. B* **268** 3163 (2010)
117. Leino A A et al. *Nucl. Instrum. Meth. Phys. Res. B* **326** 289 (2014)
118. Gol'danskii V I, Lantsburg E Ya, Yampol'skii P A *JETP Lett.* **21** 166 (1975); *Pis'ma Zh. Eksp. Teor. Fiz.* **21** 365 (1975)
119. Schwartz K et al. *Nucl. Instrum. Meth. Phys. Res. B* **245** 204 (2006)
120. Ronchi C J *J. Appl. Phys.* **44** 3575 (1973)
121. Davydov A A, Kalinichenko A I, in *Problemy Yadernoi Fiziki i Kosmicheskikh Luchei* (Problems of Nuclear Physics and Cosmic Rays) Issue 26 (Exec. Ed. I I Zalyubovskii) (Kharkov: Vishcha Shkola, 1986) p. 60
122. Tombrello T A *Nucl. Instrum. Meth. Phys. Res. B* **94** 424 (1994)
123. Lifshits I M, Kaganov M I, Tanatarov L V *Atom. Energ.* **6** 391 (1959)
124. Gervais B, Bouffard S *Nucl. Instrum. Meth. Phys. Res. B* **88** 355 (1994)
125. Toulemonde M et al. *Matematisk-fysiske Meddeleleser* **52** 263 (2006)
126. Lifshits I M, Kaganov M I, Tanatarov L V *J. Nucl. Energy A* **12** 69 (1960)
127. Allen P B *Phys. Rev. Lett.* **59** 1460 (1987)
128. Toulemonde M et al. *Nucl. Instrum. Meth. Phys. Res. B* **166–167** 903 (2000)
129. Lang M et al. *Nucl. Instrum. Meth. Phys. Res. B* **268** 2951 (2010)
130. Moll S et al. *Phys. Rev. B* **84** 064115 (2011)
131. Dawi E A et al. *Nanotechnology* **22** 215607 (2011)
132. Meftah A et al. *Nucl. Instrum. Meth. Phys. Res. B* **237** 563 (2005)
133. Toulemonde M et al. *Nucl. Instrum. Meth. Phys. Res. B* **115** 37 (1996)
134. Sall M et al. *J. Mater. Sci.* **50** 5214 (2015)
135. Lou S-N et al. *Phys. Rev. B* **68** 134206 (2003)
136. Osmani O et al. *Nucl. Instrum. Meth. Phys. Res. B* **282** 43 (2011)
137. Rothard H *Nucl. Instrum. Meth. Phys. Res. B* **225** 27 (2004)
138. Matsuzaki S et al. *Nucl. Instrum. Meth. Phys. Res. B* (2017), in press
139. Baranov I et al. *Nucl. Instrum. Meth. Phys. Res. B* **266** 1993 (2008)
140. Anders et al. *Nucl. Instrum. Meth. Phys. Res. B* **267** 2503 (2009)
141. Kluth P et al. *Phys. Rev. Lett.* **101** 175503 (2008)
142. Itoh N et al. *J. Phys. Condens. Matter* **21** 474205 (2009)
143. Marks N A et al. *Nucl. Instrum. Meth. Phys. Res. B* **266** 2665 (2008)
144. Kamarou A et al. *Phys. Rev. B* **73** 184107 (2006)
145. Chettah A et al. *Nucl. Instrum. Meth. Phys. Res. B* **267** 2719 (2009)
146. Daraszewicz S L, Duffy O M *Nucl. Instrum. Meth. Phys. Res. B* **269** 1646 (2011)
147. Dunlop A, Jaskierowicz G, Della-Negra S *Nucl. Instrum. Meth. Phys. Res. B* **146** 302 (1998)
148. Canut B et al. *Nucl. Instrum. Meth. Phys. Res. B* **146** 296 (1998)
149. Daraszewicz S L, Duffy O M *Nucl. Instrum. Meth. Phys. Res. B* **303** 112 (2013)
150. Jakas M M, Bringa E M, Johnson R E *Phys. Rev. B* **65** 165425 (2002)
151. Gan Y, Chen J *Comput. Phys. Commun.* **183** 278 (2012)
152. Gan Y, Chen J *Appl. Phys. A* **105** 427 (2011)
153. Caro A, Victoria M *Phys. Rev. A* **40** 2287 (1989)
154. Duffy D M, Rutherford A M *J. Phys. Condens. Matter* **19** 016207 (2007)
155. Rutherford A M, Duffy D M *J. Phys. Condens. Matter* **19** 496201 (2007)
156. Colder A et al. *Nucl. Instrum. Meth. Phys. Res. B* **174** 491 (2001)

157. Medvedev N A et al. *Phys. Rev. B* **82** 125425 (2010)
158. Medvedev N A et al. *Nucl. Instrum. Meth. Phys. Res. B* **268** 2870 (2010)
159. Komarov F F et al. *Vacuum* **70** 75 (2003)
160. Herre O et al. *Phys. Rev. B* **58** 4832 (1998)
161. Gaiduk P I et al. *Phys. Rev. B* **61** 15785 (2000)
162. Komarov F F, Komarov A F, Mironov A M *Nucl. Instrum. Meth. Phys. Res. B* **148** 159 (1999)
163. Komarov F F, Belyi V A *JETP* **95** 316 (2002); *Zh. Eksp. Teor. Fiz.* **122** 366 (2002)
164. Gaiduk P I et al. *Phys. Rev. B* **66** 045316 (2002)
165. Gaiduk P I *Vacuum* **78** 375 (2005)
166. Colder A et al. *J. Appl. Phys.* **91** 5852 (2002)
167. Komarov F F et al. *Vacuum* **78** 353 (2005)
168. Komarov F F, Yuvchenko V N *Tech. Phys.* **48** 717 (2003); *Zh. Tekh. Fiz.* **73** (6) 56 (2003)
169. *Landolt-Börnstein. Series Numerical Data and Functional Relationships in Science and Technology* (New Series, Vol. 17a) (Berlin: Springer, 1982) p. 642
170. Jordan A S *J. Cryst. Growth* **71** 551 (1985)
171. Gantmakher V F, Levinson Y B *Carrier Scattering in Metals and Semiconductors* (Amsterdam: Horth-Holland, 1987) p. 352
172. Volkov A E, Borodin V A *Nucl. Instrum. Meth. Phys. Res. B* **193** 381 (2002)
173. Komarov F F et al. *Dokl. Nats. Akad. Nauk Belarusi* **48** 64 (2004)
174. Szenes G *Nucl. Instrum. Meth. Phys. Res. B* **296** 174 (2011)
175. Szenes G *Nucl. Instrum. Meth. Phys. Res. B* **280** 88 (2012)
176. Itoh N, Stoneham A M *Nucl. Instrum. Meth. Phys. Res. B* **146** 362 (1998)
177. Yavlinskii Yu N *Nucl. Instrum. Meth. Phys. Res. B* **166–167** 35 (2000)
178. Osmani O et al. *Nucl. Instrum. Meth. Phys. Res. B* **317** 72 (2013)
179. Hillyard P B et al. *Phys. Rev. Lett.* **98** 125501 (2007)
180. Wang J et al. *J. Phys. Condens. Matter* **25** 135001 (2013)
181. Lushchik A et al. *Phys. Status Solidi B* **250** 261 (2013)
182. Ovchinnikov V V *Phys. Usp.* **51** 955 (2008); *Usp. Fiz. Nauk* **178** 991 (2008)
183. Zakharov V E, Kuznetsov E A *Phys. Usp.* **55** 535 (2012); *Usp. Fiz. Nauk* **182** 569 (2012)
184. Vaisburd D I (Ed.) *Vysokoenergeticheskaya Elektronika Tverdogo Tela* (Solid State High Energy Electronics) (Novosibirsk: Nauka, 1982)
185. Haas M et al. *Phys. Rev. B* **84** 144303 (2011)
186. Guo H et al. *Physica B* **407** 2262 (2012)
187. Kluth P et al. *Phys. Rev. Lett.* **101** 175503 (2008)
188. Kluth P et al. *Nucl. Instrum. Meth. Phys. Res. B* **266** 2994 (2008)
189. Krauser J et al. *J. Appl. Phys.* **94** 1959 (2003)
190. O'Connell J H et al. *Nucl. Instrum. Meth. Phys. Res. B* **374** 97 (2016)
191. Skuratov V A et al. *Nucl. Instrum. Meth. Phys. Res. B* **326** 223 (2014)
192. Schwartz K et al. *Phys. Rev. B* **78** 024120 (2008)
193. Njoroge E G et al. *Nucl. Instrum. Meth. Phys. Res. B* **371** 263 (2016)
194. Bhattacharya D et al. *Surf. Coat. Technol.* **158–159** 59 (2002)
195. Sisodia V et al. *Appl. Surf. Sci.* **252** 4016 (2006)
196. Sisodia V et al. *Rad. Eff. Def. Solids* **164** 566 (2009)
197. Agarwal G et al. *Surf. Interf. Anal.* **41** 746 (2009)
198. Agarwal G et al. *Appl. Phys. A* **99** 879 (2010)
199. Nagel R, Balogh A G *Nucl. Instrum. Meth. Phys. Res. B* **156** 135 (1999)
200. Senkara J et al. *Elektronika* **40** (11) 11 (1999)
201. Bolse W, Schattat B *Nucl. Instrum. Meth. Phys. Res. B* **209** 34 (2003)
202. Schattat B, Bolse W *Nucl. Instrum. Meth. Phys. Res. B* **225** 105 (2004)
203. Lu F, Lang M, Huang M *Nucl. Instrum. Meth. Phys. Res. B* **286** 266 (2012)
204. Wang Z G et al. *Nucl. Instrum. Meth. Phys. Res. B* **209** 194 (2003)
205. Zhang K et al. *Nucl. Instrum. Meth. Phys. Res. B* **249** 167 (2006)
206. Kumar S et al. *Nucl. Instrum. Meth. Phys. Res. B* **212** 242 (2003)
207. Kumar S et al. *Nucl. Instrum. Meth. Phys. Res. B* **266** 1759 (2008)
208. Szenes G et al. *Nucl. Instrum. Meth. Phys. Res. B* **191** 186 (2002)
209. Wang L et al. *Radiat. Eff. Defects Solids* **126** 403 (1993)
210. Toulemonde M et al. *Nucl. Instrum. Meth. Phys. Res. B* **116** 37 (1996)
211. Douillard L, Duraud J P *Nucl. Instrum. Meth. Phys. Res. B* **107** 212 (1996)
212. Awazu K et al. *Phys. Rev. B* **62** 3689 (2000)
213. Kaniukov E Yu et al. *Nanotechnology* **27** 115305 (2016)
214. Busch M C et al. *J. Appl. Phys.* **71** 2596 (1992)
215. Dallanora A et al. *J. Appl. Phys.* **104** 024307 (2008)
216. Awazu K, Kawazoe H *J. Appl. Phys.* **94** 6243 (2003)
217. Garcia-Navarro A et al. *Nucl. Instrum. Meth. Phys. Res. B* **249** 172 (2006)
218. Komarov F F et al. *Vacuum* **78** 361 (2005)
219. Klaumünzer S *Nucl. Instrum. Meth. Phys. Res. B* **225** 136 (2004)
220. Klaumünzer S et al. *Nucl. Instrum. Meth. Phys. Res. B* **39** 665 (1989)
221. Sigrist A, Balzer R *Helv. Phys. Acta* **50** 49 (1977)
222. Musket R G et al. *J. Appl. Phys.* **91** 5760 (2002)
223. Vlasukova L et al. *Vacuum* **129** 137 (2016)
224. Carvalho A M J F et al. *Thin Solid Films* **517** 289 (2008)
225. Vlasukova L A et al. *Bull. Russ. Acad. Sci. Phys.* **76** 582 (2012); *Izv. Ross. Akad. Nauk Ser. Fiz.* **76** 653 (2012)
226. Al'zhanova A et al. *Nucl. Instrum. Meth. Phys. Res. B* **374** 121 (2016)
227. Vlasukova L A et al. *Vacuum* **105** 107 (2014)
228. Komarov F F et al. *Lith. J. Phys.* **49** 111 (2009)
229. Jensen J et al. *Nucl. Instrum. Meth. Phys. Res. B* **243** 119 (2006)
230. Nomura K et al. *Phys. Rev. B* **68** 064106 (2003)
231. Vlasukova L A et al. *Bull. Russ. Acad. Sci. Phys.* **74** 206 (2010); *Izv. Ross. Akad. Nauk Ser. Fiz.* **74** 226 (2010)
232. Zinkle S J, Skuratov V A, Hoelzer D T *Nucl. Instrum. Meth. Phys. Res. B* **191** 758 (2002)
233. Canut B et al. *Nucl. Instrum. Meth. Phys. Res. B* **266** 2819 (2008)
234. Nakajima K et al. *Nucl. Instrum. Meth. Phys. Res. B* **291** 12 (2012)
235. Morita Y et al. *Nucl. Instrum. Meth. Phys. Res. B* **315** 142 (2013)
236. Kitayama T et al. *Nucl. Instrum. Meth. Phys. Res. B* **354** 183 (2015)
237. Toulemonde M et al. *Phys. Rev. B* **83** 054106 (2011)
238. Sun Y et al. *Nucl. Instrum. Meth. Phys. Res. B* **218** 318 (2004)
239. Takahashi et al. *Nucl. Instrum. Meth. Phys. Res. B* **217** 435 (2004)
240. Adla A, Fuess H, Trautmann C *J. Polym. Sci. B* **41** 2892 (2003)
241. Costantini J M et al. *Nucl. Instrum. Meth. Phys. Res. B* **194** 132 (2004)
242. Virk S H *Nucl. Instrum. Meth. Phys. Res. B* **191** 739 (2002)
243. Severin D, Bender M, Heuser J M *Nucl. Instrum. Meth. Phys. Res. B* **236** 456 (2005)
244. Diwan P K et al. *Nucl. Instrum. Meth. Phys. Res. B* **266** 4738 (2008)
245. Ma M et al. *Nucl. Instrum. Meth. Phys. Res. B* **286** 233 (2012)
246. Delgado A O et al. *Nucl. Instrum. Meth. Phys. Res. B* **273** 55 (2012)
247. Deslandes A et al. *Nucl. Instrum. Meth. Phys. Res. B* **314** 90 (2013)
248. Metz S et al. *Micromech. Microeng.* **14** 324 (2004)
249. Kaith B S et al. *Vacuum* **111** 73 (2015)
250. Fink D et al. *Nucl. Instrum. Meth. Phys. Res. B* **261** 727 (2007)
251. Fink D et al. *Rad. Meas.* **43** 5546 (2008)
252. Fink D et al. *Vacuum* **82** 900 (2008)
253. Yamaki T et al. *Nucl. Instrum. Meth. Phys. Res. B* **314** 77 (2013)
254. Neumann R *Nucl. Instrum. Meth. Phys. Res. B* **314** 4 (2013)
255. Zielinska K et al. *Nucl. Instrum. Meth. Phys. Res. B* **326** 131 (2014)
256. Satoh T et al. *Nucl. Instrum. Meth. Phys. Res. B* **332** 242 (2014)
257. Apel P Yu et al. *Nucl. Instrum. Meth. Phys. Res. B* **326** 158 (2014)
258. Hossain U H et al. *Nucl. Instrum. Meth. Phys. Res. B* **326** 135 (2014)
259. Lee E H et al. *J. Mater. Res.* **8** 377 (1993)
260. Pivin J C *Thin Solid Films* **263** 185 (1995)
261. Swain M V et al. *J. Mater. Res.* **12** 1917 (1997)
262. Dfavenas J et al. *Nucl. Instrum. Meth. Phys. Res. B* **32** 166 (1988)
263. Zhu J Z et al. *Nucl. Instrum. Meth. Phys. Res. B* **91** 469 (1994)
264. Wang Y Q et al. *Nucl. Instrum. Meth. Phys. Res. B* **710** 127 (1997)
265. Hnatowicz V *Nucl. Instrum. Meth. Phys. Res. B* **209** 145 (2003)
266. Davenas J, in *Materials under Irradiation* (Solid State Phenomena, Vols. 30–31, Eds A Dunlop et al.) (Aedermannsdorf: Trans Tech., 1993) p. 317
267. Paretzke H G et al., Report IAEA-TECDOC-799 (Vienna: IAEA, 1995) p. 633
268. Durrani S A, Bull R K *Solid State Nuclear Track Detection: Principles, Methods, and Applications* (Oxford: Pergamon Press, 1987)
269. Spohr R *Ion Tracks and Microtechnology: Principles and Applications* (Braunschweig: Vieweg, 1990)
270. Apel P et al. *Nucl. Instrum. Meth. Phys. Res. B* **185** 216 (2001)

271. Cleland M R, Parks L A, Cheng S *Nucl. Instrum. Meth. Phys. Res. B* **208** 66 (2003)
272. Dawes K, Glover L C, in *Physical Properties of Polymers Handbook* (Ed. J E Mark) (Woodbury, NY: AIP Press, 1996) Ch. 41
273. Hnatowicz V *Phys. Status Solidi B* **216** 931 (1999)
274. Fleisher R L, Price P B, Walker R M *J. Appl. Phys.* **36** 3645 (1965)
275. Szenes G *Phys. Rev. B* **52** 6154 (1995); *Phys. Rev. B* **51** 8026 (1995)
276. Balanzat E, Betz N, Bouffard S *Nucl. Instrum. Meth. Phys. Res. B* **105** 46 (1995)
277. Balanzat E et al. *Nucl. Instrum. Meth. Phys. Res. B* **91** 140 (1994)
278. Betz N et al. *J. Polym. Sci. B* **32** 1493 (1994)
279. Picq V, Balanzat E *Nucl. Instrum. Meth. Phys. Res. B* **151** 76 (1999)
280. Ferain E, Legras R *Nucl. Instrum. Meth. Phys. Res. B* **82** 539 (1993)
281. Steckenreiter T et al. *Nucl. Instrum. Meth. Phys. Res. B* **151** 161 (1999)
282. Chipara M I et al. *Nucl. Instrum. Meth. Phys. Res. B* **88** 418 (1994)
283. Chipara M I, Reyes-Romero J *Nucl. Instrum. Meth. Phys. Res. B* **185** 77 (2001)
284. Dehaye F et al. *Nucl. Instrum. Meth. Phys. Res. B* **209** 103 (2003)
285. Ferain E *Radiat. Mes.* **34** 585 (2001)
286. Piraux L et al. *J. Mater. Res.* **14** 3042 (1999)
287. Jerome C *Chem. Eur. J.* **6** 30089 (2000)
288. Sun Y et al. *Nucl. Instrum. Meth. Phys. Res. B* **209** 188 (2003)
289. Hama Y et al. *Nucl. Instrum. Meth. Phys. Res. B* **208** 123 (2003)
290. Hai Y et al. *Nucl. Instrum. Meth. Phys. Res. B* **356 – 357** 129 (2015)
291. Radwan R M, Abdul-Kader A M, El-Hag Ali A *Nucl. Instrum. Meth. Phys. Res. B* **266** 3588 (2008)
292. Wada T et al. *J. Chem. Soc. Commun.* **1** 1194 (1985)
293. Huynh W U, Dittmer J J, Alivisatos A P *Science* **295** 2425 (2002)
294. Li Z L et al. *Appl. Phys. Lett.* **84** 3558 (2004)
295. Kumar A, Hussain A M P *Nucl. Instrum. Meth. Phys. Res. B* **251** 451 (2006)
296. Costantini J M et al. *J. Appl. Phys.* **87** 1899 (2000)
297. De Bonis A, Bearzotti A, Marletta G *Nucl. Instrum. Meth. Phys. Res. B* **151** 101 (1999)
298. Davenas J, Boiteux G *Adv. Mater.* **2** 521 (1990)
299. Costantini J M et al. *Nucl. Instrum. Meth. Phys. Res. B* **234** 458 (2005)
300. Ramola R C et al. *Current Sci.* **97** 1453 (2009)
301. Hussain A M P et al. *J. Phys. D* **39** 75 (2006)
302. Murugaraj P, Mainwaring D, Siegele R *Appl. Phys. Lett.* **94** 122101 (2009)
303. Gupta S et al. *Nucl. Instrum. Meth. Phys. Res. B* **381** 76 (2016)
304. Balanzat E, Jousset J C, Toulemonde M *Nucl. Instrum. Meth. Phys. Res. B* **32** 368 (1988)
305. Dobrev D et al. *J. Vac. Sci. Technol. B* **19** 1385 (2001)
306. Molares M E T et al. *Appl. Phys. Lett.* **82** 2139 (2003)
307. Sharma T et al. *Vacuum* **135** 73 (2017)
308. Albrecht D J et al. *Appl. Phys. A* **37** 37 (1985)
309. Saleh S A, Eyal Y *Appl. Phys. Lett.* **85** 2529 (2004)
310. Saleh S A *Nucl. Instrum. Meth. Phys. Res. B* **236** 81 (2005)
311. Apel P Yu et al. *Nucl. Instrum. Meth. Phys. Res. B* **209** 329 (2003)
312. Apel P Yu *Radiat. Meas.* **25** 667 (1995)
313. Bryk M T et al. *Nucl. Instrum. Meth. Phys. Res. B* **251** 419 (2006)
314. Mazzei R et al. *Nucl. Instrum. Meth. Phys. Res. B* **236** 407 (2005)
315. Shmidt K et al. *Nucl. Instrum. Meth. Phys. Res. B* **107** 381 (1996)
316. Microfiltration and Laboratory: Poretics Products Catalog, 1996 Edition, Livermore CA, p. l, http://www.osmonics.com/products/page330.htm
317. Kravets L I, Dmitriev S L, Apel P Yu *Khim. Vys. Energ.* **31** 108 (1997)
318. Shirokova V V, Tretyakova S P *Radiat. Meas.* **28** 791 (1997)
319. Skuratov V A, Abu-Alazm S M, Altynov V A *Mater. Sci. Forum* **248** 399 (1997)
320. Baryley H, Martin C R *Chem. Rev.* **100** 2575 (2000)
321. Kohli P et al. *Science* **305** 984 (2004)
322. Menon V P, Martin C R *Anal. Chem.* **67** 1920 (1995)
323. Grasseli M, Betz N *Nucl. Instrum. Meth. Phys. Res. B* **236** 501 (2005)
324. Mazzei R et al. *Nucl. Instrum. Meth. Phys. Res. B* **236** 407 (2005)
325. Xia Y, Yang P *Adv. Mater.* **15** 351 (2003)
326. Ferain E, Legras R *Nucl. Instrum. Meth. Phys. Res. B* **208** 115 (2003)
327. Spohr R et al. *Nucl. Instrum. Meth. Phys. Res. B* **268** 676 (2010)
328. Trautmann C, in *Ion Beams in Nanoscience and Technology* (Eds R Hellborg, H J Whitlow, Y Zhang) (Heidelberg: Springer-Verlag, 2009) p. 369
329. Martin C R *Science* **266** 1961 (1994)
330. Apel P *Nucl. Instrum. Meth. Phys. Res. B* **208** 11 (2003)
331. Toimil Molares M E et al. *Nanotechnology* **15** S201 (2004)
332. Chtanko N et al. *Nucl. Instrum. Meth. Phys. Res. B* **236** 103 (2005)
333. Man L C T et al. *Nucl. Instrum. Meth. Phys. Res. B* **265** 621 (2007)
334. Trautmann C et al. *Nucl. Tracks Radiat. Meas.* **19** 967 (1991)
335. Siwy Z et al. *Nucl. Instrum. Meth. Phys. Res. B* **208** 143 (2003)
336. Ohgai T et al. *J. Appl. Electrochem.* **38** 713 (2008)
337. Mara A et al. *Nano Lett.* **4** 497 (2004)
338. Sergent-Engelen T et al. *Biotechnol. Tech.* **4** 89 (1990)
339. Bignold L P *J. Immun. Meth.* **118** 217 (1989)
340. Fink D et al. *Nucl. Instrum. Meth. Phys. Res. B* **236** 11 (2005)
341. Duan J et al. *Nucl. Instrum. Meth. Phys. Res. B* **267** 2567 (2009)
342. Chen J et al. *Appl. Phys. Lett.* **85** 1401 (2004)
343. Berggren M, Inganas O *Science* **267** 1479 (1995)
344. Schon J H et al. *Science* **290** 963 (2000)
345. Lindeberg M et al., in *Proc. of the Workshop on European Network on Ion Track Technology, Caen, France, 24 – 26 February 2002*
346. Berdinsky A S et al. *Chem. Sustainable Dev.* **8** 141 (2000)
347. Fink D et al. *Radiat. Meas.* **36** 605 (2003)
348. Bohm S, Oltuis W, Bergveld P *Sensors Actuat. B* **63** 201 (2000)
349. Yoshida M et al. *Nucl. Instrum. Meth. Phys. Res. B* **122** 39 (1997)
350. Yousef H, Lindeberg M, Hjort K *Nucl. Instrum. Meth. Phys. Res. B* **266** 1659 (2008)
351. Fink D "Novel ion track-based electronic structures. An overview", ISL-Information (Berlin: HMI, 2005) p. 2
352. Fink D et al. *Nucl. Instrum. Meth. Phys. Res. B* **218** 355 (2004)
353. Hoppe K et al. *Nucl. Instrum. Meth. Phys. Res. B* **266** 1642 (2008)
354. Zollondz J-H et al. *Nucl. Instrum. Meth. Phys. Res. B* **225** 178 (2004)
355. Thornell G et al. *Sensors Actuators A* **73** 176 (1999)
356. Thornell G, Rapp H, Hjort K *IEEE Trans. Ultrason. Ferroelectrics* **47** 8 (2000)
357. Pezzagna S et al. *Phys. Status Solidi A* **208** 2017 (2011)
358. Sanz R et al. *Nanotechnology* **18** 305303 (2007)
359. Skupinski M et al. *Vacuum* **82** 359 (2007)
360. Mitrofanov A V, Apel P Yu *Nucl. Instrum. Meth. Phys. Res. B* **245** 332 (2006)
361. Fisher B E, Spohr R *Rev. Mod. Phys.* **55** 907 (1983)
362. German Patent Application 201197413 (2002)
363. Akapiev G N et al. *Nucl. Instrum. Meth. Phys. Res. B* **208** 133 (2003)
364. Stolterfoht N et al. *Phys. Rev. Lett.* **88** 133201 (2002)
365. Li D H et al. *Nucl. Instrum. Meth. Phys. Res. B* **267** 469 (2009)
366. Stolterfoht N *Nucl. Instrum. Meth. Phys. Res. B* **317** 96 (2013)
367. Keerthisinghe D et al. *Nucl. Instrum. Meth. Phys. Res. B* **317** 105 (2013)
368. Komarov F F, Kamyshan A S, Karwat Cz *Vacuum* **83** S51 (2009)
369. Gravier L et al. *IEEE Trans. Magn.* **38** 2700 (2002)
370. Enculescu I et al. *Appl. Phys. A* **86** 43 (2007)
371. Ferain E, Legras R *Nucl. Instrum. Meth. Phys. Res. B* **267** 1028 (2009)
372. Zhu X R et al. *Nucl. Instrum. Meth. Phys. Res. B* **356 – 357** 57 (2015)
373. Gudiksen M S, Wang J, Lieber C M *J. Phys. Chem. B* **106** 4036 (2002)
374. US Patent 6,328,342 (2001)
375. Ameniya K et al. *Nucl. Instrum. Meth. Phys. Res. B* **356 – 357** 154 (2015)
376. Fleischer R *MRS Bull.* **20** (12) 35 (1995)
377. Durante M et al. *Nucl. Instrum. Meth. Phys. Res. B* **94** 251 (1994)
378. Snoeks E et al. *Adv. Mater.* **12** 1511 (2000)
379. van Dillen T et al. *Nucl. Instrum. Meth. Phys. Res. B* **175** 350 (2001)
380. Klaumünzer S *Nucl. Instrum. Meth. Phys. Res. B* **215** 345 (2004)
381. D'Orleans C D et al. *Nucl. Instrum. Meth. Phys. Res. B* **225** 154 (2004)
382. Klaumünzer S *Nucl. Instrum. Meth. Phys. Res. B* **244** 1 (2006)
383. Penninkhof J J et al. *Nucl. Instrum. Meth. Phys. Res. B* **242** 523 (2006)
384. Giulian R et al. *Nucl. Instrum. Meth. Phys. Res. B* **266** 3158 (2008)
385. Kerboua C H, Chicoine M, Roorda S *Nucl. Instrum. Meth. Phys. Res. B* **269** 2006 (2011)

386. Rizza G, Ridgway M C, in *Ion Beam Modification of Solids* (Eds W Wesch, E Wendler) (Berlin: Springer, 2016) p. 443
387. Sprouster D J et al. *Appl. Phys.* **109** 113504 (2011)
388. D'Orleans C et al. *Nucl. Instrum. Meth. Phys. Res. B* **209** 316 (2003)
389. Roorda S et al. *Adv. Mater.* **16** 235 (2004)
390. van Dillen T, van Blaaderen A, Polman A *Mater. Today* **7** 40 (2004)
391. Ridgway M C et al. *Phys. Rev. Lett.* **106** 095505 (2011)
392. Awazu K et al. *Phys. Rev. B* **78** 054102 (2008)
393. Kluth P et al. *Appl. Phys. Lett.* **94** 113107 (2009)
394. Zeng H et al. *Appl. Phys.* **87** 4718 (2000)
395. Pannu C et al. *Nucl. Instrum. Meth. Phys. Res. B* **379** 206 (2016)
396. Davi E A et al. *Nucl. Instrum. Meth. Phys. Res. B* **384** 86 (2016)
397. Kerboua C H et al. *Thin Solid Films* **527** 186 (2013)
398. Datta D P et al. *Appl. Surf. Sci.* **310** 164 (2014)
399. Oliver A et al. *Phys. Rev. B* **74** 245425 (2006)
400. Singh F et al. *Nucl. Instrum. Meth. Phys. Res. B* **311** 5 (2013)
401. Yang Y et al. *Nucl. Instrum. Meth. Phys. Res. B* **308** 24 (2013)
402. Ridgway M C et al. *Nucl. Instrum. Meth. Phys. Res. B* **267** 931 (2009)
403. Joseph B et al. *Nucl. Instrum. Meth. Phys. Res. B* **256** 659 (2007)
404. Giulian R et al. *Phys. Rev. B* **78** 125413 (2008)
405. Johanessen B et al. *Nucl. Instrum. Meth. Phys. Res. B* **250** 210 (2006)
406. Krasheninnikov A V, Nordlund K *J. Appl. Phys.* **107** 071301 (2010)
407. Avasthi D K, Mehta G H *Swift Heavy Ions for Materials Engineering and Nanostructuring* (Dordrecht: Springer, 2011)
408. Mishra Y K et al. *Appl. Phys. Lett.* **91** 063103 (2007)
409. Giulian R et al. *Phys. Rev. B* **82** 113410 (2010)
410. Mahanta D et al. *Eur. Phys. J. Appl. Phys.* **35** 29 (2006)
411. Shirai M et al. *Nucl. Instrum. Meth. Phys. Res. B* **269** 1787 (2009)
412. Schmidt B et al. *Nucl. Instrum. Meth. Phys. Res. B* **267** 1345 (2009)
413. Amekura H et al. *Appl. Phys. Lett.* **103** 203106 (2013)
414. Rodichev D et al. *Nucl. Instrum. Meth. Phys. Res. B* **107** 259 (1996)
415. Hirschman K D et al. *Nature* **384** 338 (1996)
416. Arnoldbik W M et al. *Phys. Rev. B* **71** 125329 (2005)
417. Arnoldbik W M et al. *Nucl. Instrum. Meth. Phys. Res. B* **258** 199 (2007)
418. Saxena N et al. *Phys. Status Solidi A* **209** 283 (2012)
419. Ardyanian M, Rinnert H, Vergnat M *Appl. Phys. Lett.* **89** 11902 (2006)
420. Batra Y et al. *J. Phys. D* **40** 4568 (2007)
421. Mohanty T et al. *J. Nanosci. Nanotechnol.* **7** 1 (2007)
422. Tripathi N et al. *Nucl. Instrum. Meth. Phys. Res. B* **268** 3335 (2010)
423. Iwase A et al. *Nucl. Instrum. Meth. Phys. Res. B* **195** 309 (2002)
424. Valentin E et al. *Phys. Rev. Lett.* **86** 99 (2001)
425. Volkov A E, Korolev D N *Nucl. Instrum. Meth. Phys. Res. B* **209** 98 (2003)
426. Antonova I V et al. *Nanotechnology* **20** 095205 (2009)
427. Rao S et al. *Nucl. Instrum. Meth. Phys. Res. B* **268** 1741 (2010)
428. Saikiran V et al. *Nucl. Instrum. Meth. Phys. Res. B* **323** 14 (2014)
429. Komarov F F et al. *Bull. Russ. Acad. Sci. Phys.* **80** 141 (2016); *Izv. Ross. Akad. Nauk Ser. Fiz.* **80** 160 (2016)
430. Saikiran V et al. *Nucl. Instrum. Meth. Phys. Res. B* **333** 99 (2014)
431. Rizza G, Dunlop A, Dezellus A *Nucl. Instrum. Meth. Phys. Res. B* **256** 219 (2007)
432. Sprouster D J et al. *Phys. Rev. B* **80** 115438 (2009)
433. Leino A A, Djurabekova F, Nordlund K *Eur. Phys. J. B* **87** 242 (2014)
434. Studer F et al. *Nucl. Instrum. Meth. Phys. Res. B* **82** 91 (1993)
435. Gokholl Sh et al. *Nucl. Instrum. Meth. Phys. Res. B* **333** 64 (2014)
436. Ghidini M et al. *J. Magn. Magn. Mater.* **140 – 144** 483 (1995)
437. Srivastava P C, Tripathi J K *J. Phys. D* **39** 1465 (2006)
438. Provost J et al. *MRS Bull.* **20** (12) 22 (1995)
439. Wiesner J et al. *Physica C* **268** 161 (1996)
440. Rani S et al. *Nanosensor Technol.* **2008** 395490 (2008)
441. Messenger G C, Ash M S *Single Event Phenomena* (New York: Chapman and Hall, 1997)
442. Cellere G et al. *J. Appl. Phys.* **38** 160 (2016)
443. Ma Y et al. *Nucl. Instrum. Meth. Phys. Res. B* **273** 40 (2012)
444. Kumar A et al. *Nanotechnology* **21** 175102 (2010)
445. Merk B et al. *Nucl. Instrum. Meth. Phys. Res. B* **306** 81 (2013)
446. Durante M *Life Sci. Space Res.* **1** 2 (2014)
447. Guan J, Wang L, Qin X *Nucl. Instrum. Meth. Phys. Res. B* **315** 318 (2013)
448. Liu G et al. *Nucl. Instrum. Meth. Phys. Res. B* **325** 43 (2014)
449. Yang J et al. *Appl. Opt.* **50** 6678 (2011)
450. Yao Y C et al. *Opt. Express* **19** 2452 (2011)
451. Zhou Y F et al. *Nucl. Instrum. Meth. Phys. Res. B* **315** 328 (2013)
452. Kip D *Appl. Phys. B* **67** 131 (1998)
453. Prabakaran K et al. *Nucl. Instrum. Meth. Phys. Res. B* **394** 81 (2017)
454. Biswas A et al. *Nano Lett.* **3** 69 (2003)
455. Bhavsar K H, Joshi U *Nucl. Instrum. Meth. Phys. Res. B* **379** 95 (2016)
456. Seki S *Adv. Mater.* **13** 1663 (2001)
457. Biswas A et al. *Nucl. Instrum. Meth. Phys. Res. B* **217** 39 (2004)
458. Norman G E et al. *Contrib. Plasma Phys.* **53** 129 (2013)
459. Saumon D et al., in *Frontiers and Challenges in Warm Dense Matter* (Ed. F Graziani) (Heidelberg: Springer, 2014) p. 151
460. Sadi S et al. *Nucl. Instrum. Meth. Phys. Res. B* **328** 78 (2014)